THESIS FOR THE DEGREE OF DOCTOR OF PHILOSOPHY

Predictions of Hydrodynamics of a Conceptual FLNG-LNG Offloading System

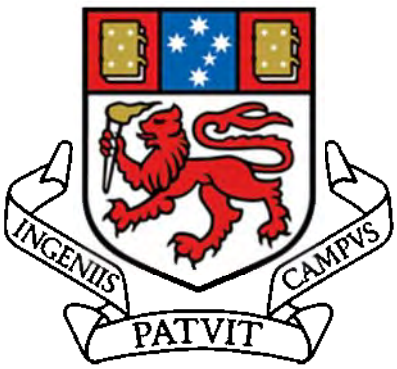

National Centre of Maritime Engineering and Hydrodynamics
AUSTRALIAN MARITIME COLLEGE, UNIVERSITY OF TASMANIA
Launceston, Australia
2018

Declarations

This thesis contains no material which has been accepted for a degree or diploma by the University or any other institution, except by way of background information and duly acknowledged in the thesis, and to the best of my knowledge and belief, no material previously published or written by another person, except where due acknowledgement is made in the text of the thesis, nor does the thesis contain any material that infringes copyrights.

This thesis may be made available for loan and limited copying in accordance with the *Copyright Act 1968*

Signed:

Yuting Jin (金玉庭)

Date 04/04/2018

Declaration for thesis containing published work

This thesis contains published work and/or work prepared for publication, some of which have been co-authored. These publications have been modified to fit into the structure of the thesis. The bibliographical details of the work are outlined below and the full publications of the peer-reviewed journal papers can be seen in the Appendix:

Paper I

Jin, Y., Chai, S., Duffy, J., Chin, C., Bose, N., & Templeton, C. (2016). RANS prediction of FLNG-LNG hydrodynamic interactions in steady current. Applied Ocean Research, 60, 141-154. **(Chapter 4)**

Paper II

Jin, Y., Chai, S., Duffy, J., Chin, C., & Bose, N. (2016). Experimental Study of Wave Induced Loads and Motions on FLNG in Head and Oblique Sea Waves. Paper presented at the ASME 2016 35th International Conference on Ocean, Offshore and Arctic Engineering. **(Chapter 5)**

Paper III

Jin, Y., Chai, S., Duffy, J., Chin, C., Bose, N., & Sun, L. (2016). URANS Prediction of Ship Hydrodynamics in Head Sea Waves at Zero Forward Speed with Model Testing Validation. Paper presented at the ASME 2016 35th International Conference on Ocean, Offshore and Arctic Engineering. **(Chapter 5)**

Paper IV

Jin, Y., Chai, S., Duffy, J., Chin, C., & Bose, N (2017). URANS predictions of wave induced loads and motions on ships in regular head and oblique waves at zero forward speed. Journal of Fluids and Structures 74, 178-204. **(Chapter 5)**

Paper V

Jin, Y., Chai, S., Duffy, J., Chin, C., & Bose, N (2017). URANS predictions on the hydrodynamic interaction of a conceptual FLNG-LNG offloading system in regular waves. Ocean Engineering 153, 362-386. **(Chapter 6)**

Paper VI

Jin, Y., Chai, S., Duffy, J., Chin, C., & Bose, N (2017). Hydrodynamics of a conceptual FLNG system in side-by-side offloading operation. Ships and Offshore Structures **(Chapter 7) - Under Review**

Paper VII

Jin, Y., Chai, S., Duffy, J., Chin, C., & Bose, N. (2015). Scale Effects on Hydrodynamic Manoeuvring Force Prediction. Paper presented at the Twenty-fifth International Offshore and Polar Engineering Conference. **(Appendix)**

Paper VIII

Jin, Y., Duffy, J., Chai, S., Chin, C., & Bose, N. (2016). URANS study of scale effects on hydrodynamic manoeuvring coefficients of KVLCC2. Ocean Engineering, 118, 93-106. **(Appendix)**

Statement of Co-Authorship

The following people and institutions contributed to the publication of work undertaken as part of this thesis:

School/Institution	Name	Role
Yuting Jin	University of Tasmania	Candidate
A Prof. Shuhong Chai	University of Tasmania	Author 1
Dr. Jonathan Duffy	University of Tasmania	Author 2
Dr. Christopher Chin	University of Tasmania	Author 3
Prof. Neil Bose	University of Tasmania	Author 4

Author details and their roles:

Paper 1: RANS prediction of FLNG-LNG hydrodynamic interactions in steady current
Located in chapter 4
The estimated percentage contribution of the candidate is 80%. The co-authors contributed to the concept and design of the research project.

Paper 2: Experimental Study of Wave Induced Loads and Motions on FLNG in Head and Oblique Sea Waves
Located in chapter 5
The estimated percentage contribution of the candidate is 80%. The co-authors contributed to the concept and design of the research project, and provided financial support for attending the conference.

Paper 3: URANS Prediction of Ship Hydrodynamics in Head Sea Waves at Zero Forward Speed with Model Testing Validation
Located in chapter 5
The estimated percentage contribution of the candidate is 80%. The co-authors contributed to the concept and design of the research project, and provided financial support for attending the conference.

Paper 4: URANS predictions of wave induced loads and motions on ships in regular head and oblique waves at zero forward speed

Located in chapter 5

The estimated percentage contribution of the candidate is 80%. The co-authors contributed to the concept and design of the research project.

Paper 5: URANS predictions on the hydrodynamic interaction of a conceptual FLNG-LNG offloading system in regular waves

Located in chapter 6

The estimated percentage contribution of the candidate is 80%. The co-authors contributed to the concept and design of the research project.

Paper 6: Hydrodynamics of a conceptual FLNG system in side-by-side offloading operation

Located in chapter 7

The estimated percentage contribution of the candidate is 80%. The co-authors contributed to the concept and design of the research project.

Paper 7: Scale Effects on Hydrodynamic Manoeuvring Force Prediction

Located in Appendix

The estimated percentage contribution of the candidate is 80%. The co-authors contributed to the concept and design of the research project. and provided financial support for attending the conference.

Paper 8: URANS study of scale effects on hydrodynamic manoeuvring coefficients of KVLCC2

Located in Appendix

The estimated percentage contribution of the candidate is 80%. The co-authors contributed to the concept and design of the research project.

We the undersigned agree with the above stated proportion of work undertaken for each of the above published (or submitted) peer-reviewed manuscripts contributing to this thesis.

Signed:

A Prof. Shuhong Chai	**Prof. Natalia Nikolova**
Primary Supervisor	Principal
College of Engineering and Science	Australian Maritime College
University of Tasmania	University of Tasmania

Date: 04/04/18

Acknowledgement

I never expected the time to slip away so fast when I started my PhD research at the National Centre for Maritime Engineering and Hydrodynamics in 2014. The entire trip of the study and research has been full of challenges, difficulties and hope all along the way. After a three and half-year time, now it comes to an end. This thesis would not have been possible without the support and help from several individuals and institutions.

First and foremost, I would like to express my sincere gratitude to my primary supervisor, Associate Professor Shuhong Chai, for her professional knowledge and valuable instructions benefiting my study much, for her constant inspiration and encouragement while I was struggling with the research. It has been greatly enjoyable to work together with her during the past years. I would also like to extend my thankfulness to Dr. Jonathan Duffy for his excellent and distinctive data analysing and research ideas. At last, I want to thank my other co-supervisors Dr. Christopher Chin and Professor Neil Bose for their constant support for my PhD work.

During the course of this work I conducted model scale experiments using the model test basin facility at the Australian Maritime College. Many thanks to towing tank staff who provided valuable assistance during the conduct of the experiments. Thanks particularly to Tim Lilienthal and Adam Rolls. In addition, many thanks to the Flanders Hydraulics Research (Belgium) and SIMMAN for their valuable experimental data for validating my work.

Last but not least, my great appreciation goes to my dear parents for their unconditional love and warmest confidence in my all through these years; to my girlfriend Xi Liu for her love all along through the past three and half years. I am grateful to all the other family members for their warm-hearted concern. This thesis is dedicated to my beloved whole family.

Abstract

The offloading operation between a floating liquefied natural gas (FLNG) facility and an LNG carrier are often of limited duration depending on the sea environment. In extreme seas or even in moderate sea states, strong hydrodynamic interactions between the FLNG and LNG may occur with resonant motions of the fluid in the gap between the two ships, leading to excessive ship motions and limiting the operability of on-board facilities. Taking an alternative approach of a conventional potential flow (PF) method, this study focuses on the application of solving viscous Reynolds-Averaged Navier-Stokes (RANS) equations for investigating the hydrodynamic interactions of a conceptual side-by-side FLNG-LNG offloading system. To tackle this complex engineering problem, the research has been built up systematically.

Initially, predictions of the interaction forces and moments in steady current are carried out with a quasi-static approach. The feasibility of RANS computation is demonstrated through validations against existing benchmark experimental results. The effects of varying longitudinal and lateral offsets on the hydrodynamic interactions are analysed. When comparing model and full scale computations, scale effects are evident in the surge force but found to be less influential in the predictions of sway force, roll moment and yaw moment for the cases tested.

For analysing the hydrodynamic behaviour of the FLNG-LNG system in waves, a two-phase volume of fluid (VOF) method is adopted together with the fifth-order Stokes wave theory in the unsteady RANS (URANS) computation. This investigation is firstly performed for predicting wave induced loads and motions on single FLNG and single LNG in regular waves for assessing the credibility of the numerical approach. The computed wave loads correlated well with experimental measurements performed at the AMC model test basin.

Applying an analogous approach, URANS computations of FLNG-LNG interactions are carried out for different wave frequencies and lateral separations with the vessels constrained in 6 degrees of freedom (DOF) being fixed. Physical model tests on the FLNG-LNG interactions in regular waves are performed for validation. URANS computations show better accuracy over the PF calculations, especially at relatively high wave frequency conditions where the gap wave resonance occurs. It is seen that the gap wave resonance appears when the incident wave frequency approaches the natural frequency of the gap fluid, resulting in significant variation of wave loads in the directions of sway, heave, pitch and yaw. Meanwhile, the lateral separation is found to have an inverse relationship with the natural frequency of the gap fluid. Reduction in the lateral separation shifts the occurrence of gap wave resonance to a higher wave frequency and brings more significant exaggerations on the gap waves and wave loads. When comparing model and full scale wave loads and gap wave responses, the two series of data correlate well implying insignificant influence of scale effects.

To investigate the global performance of the side-by-side FLNG-LNG system in a real world scenario, a case study based on time domain analysis is carried out when the system is coupled with mooring lines, fenders and hawsers in an irregular sea environment. The system is moored by an inner turret mooring system allowing weathervaning under external disturbances. A thorough overview of the relative motions between the two ships is presented as well as the mooring line and fender loads. The effects of varying hawser pretension and stiffness on the hydrodynamic performance of the system and the loads of the connection system are presented.

As above, the presented work provides insights into the hydrodynamics of the FLNG-LNG interactions in steady current and regular waves, especially for quantifying the hydrodynamic loads and gap wave responses in head sea conditions. The results will assist safe manoeuvring and mooring of the LNG alongside the FLNG in respect of achieving minimal hydrodynamic loads and relative motions between the vessels. The information gathered can also be incorporated into the mathematical model of ship-handling simulators for crew training purposes in the near future.

Table of Contents

List of Figures

List of Tables

Nomenclature

A	Wave amplitude
B	Beam
B_{ij}	Fifth order Stokes wave coefficients
C_B	Block coefficient
d	Model test basin water depth
D	Moulded depth
f	Wave frequency
F_i	Wave induced force
Fr	Length Froude number based on flow speed
h	Water depth
H	Wave height
H_G	Gap wave height
H_G'	Non-dimensional gap wave height
H_0	Incident wave height
I	Moment of inertia about centre of gravity
k_w	Wave number
k_{xx} k_{yy} k_{zz}	Radius of gyration
K	Roll moment
K′	Non-dimensional roll moment
L_w	Wave length
L_{OA}	Ship overall length
L_{pp}	Length between perpendiculars
M_i	Wave induced moment
n	Propeller rate
N	Yaw moment
N′	Non-dimensional yaw moment
Re	Reynolds number
ΔS	FLNG and LNG lateral separation
S_W	Rudder wetted surface area
S_L	Rudder lateral area
T	Draft
T_P	Wave period
TF_{Fi}	Force transfer function
TF_{Mi}	Moment transfer function
TF_{Xi}	Ship motion transfer function
U	Velocity/Flow speed

Δx	Relative longitudinal position between CoGs
X	Surge force
X'	Non-dimensional surge force
X_{ii}	Ship motion response
Δy	Relative transverse position between CoGs
Y	Sway force
Y'	Non-dimensional sway force
β	Drift angle
ω	Wave frequency
μ	Wave heading, angle between the vessel heading and wave direction
λ	Scale factor
ρ	Water density
η	Free surface elevation
η'	Non-dimensional gap wave elevation

Abbreviation

AMC	Australian Maritime College
Aframax	Aframax class container ship
CoG	Centre of gravity
CFD	Computational fluid dynamics
DoF	Degree of freedom
DNV	Det Norske Veritas guidelines/regulations
EFD	Experimental fluid dynamics
FLNG	Floating liquefied natural gas facility
FLNG/LNG	FLNG or LNG single vessel alone
FLNG-LNG	FLNG and LNG in side-by-side
FS	Full scale
FFT	Fast fourier transformation
FHR	Flanders Hydraulics Research
ITTC	International Towing Tank Conference
IOWA	University of IOWA
JONSWAP	Joint North Sea Wave Project
KVLCC2	KRISO very large crude carrier 2
KCS	KRISO container ship
LCG	Longitudinal centre of gravity from the bow
LNG	Liquefied natural gas carrier

LVDT	Linear variable differential transducer
MS	Model scale
PF	Potential flow
P-P	Peak to peak
QTF	Quadratic transfer function
RANS	Reynolds-Averaged Navier Stokes
SST	Shear stress transport
STD	Standard deviation
SWL	Safe working load
URANS	Unsteady Reynolds-Averaged Navier Stokes
VCG	Vertical centre of gravity from the keel
WP	Wave probe

Chapter 1 - Introduction

1.1 Background

The demand for natural gas, the cleanest burning fossil fuel, is expected to increase sharply in the future, making the exploitation of offshore gas fields more attractive. FLNG, an innovative type of floating LNG production and storage platform which consists of a FPSO-type hull equipped with LNG storage tanks and liquefaction plants, has been proposed and developed in the past decade (Zhao et al., 2011). Previous research investigating this type of production system and its associated technology has supported FLNG as a promising solution of exploiting stranded gas fields (Zhao et al., 2014). In Australia, Shell's Prelude FLNG Project (Figure 1.1), which is likely to be the world's first FLNG facility, has been scheduled to operate in 2017. As the development of the FLNG technology has already moved forward from the design phase, optimisation of the operational performance of such LNG production facilities has drawn much attention. One of the most concerned difficulties for the FLNG technology is the hydrodynamic interaction induced large relative motions between the FLNG and the LNG carrier in a side-by-side configuration, which is considered as a potential threat to the flexible cryogenic LNG offloading hose (Kim et al., 2012). In extreme seas or even in moderate sea states, strong hydrodynamic interactions between the FLNG and LNG may occur with resonant motions of the fluid in the gap between the two ships. This could consequently result in excessive ship motions limiting the duration of the LNG offloading operations. Therefore, accurate predictions of the hydrodynamics around the FLNG-LNG system are essential for improving the operability of on-board facilities.

The complexity of the FLNG-LNG hydrodynamic interactions poses a great challenge to the most advanced computational methods to estimate their performance in different environmental conditions. In this thesis, the feasibility of applying modern Computational Fluid Dynamics (CFD) methods to investigate the hydrodynamic interactions between the FLNG and LNG vessels has been studied. The numerical simulations were performed using different environmental conditions to predict the current and wave induced loads on the FLNG-LNG system. The accuracy of the two numerical approaches, the inviscid potential flow (PF) method and the viscous Reynolds-Averaged Navier Stokes (RANS) method has been assessed by comparing to experimental results.

Figure 1.1 Shell's Prelude FLNG to operate in Australia (Courtesy of Shell))

1.2 Previous and Related Studies

Existing methods for predicting the hydrodynamic interactions between two vessels in close proximity include Experimental Fluid Dynamics (EFD) and CFD. In most cases, these two methods are employed together, offering more credible estimations on the ship-ship interaction problem. The experimental studies are also often carried out for the purpose of validating the numerical work. In this section, an overview of literature on the subject ship-ship interaction is presented, covering the relevant studies concerning the efficiency and accuracy of existing approaches when investigating the problem.

1.2.1 Experimental fluid dynamics methods

Extensive EFD studies have been carried out by previous researchers to investigate the hydrodynamic interaction between ships in close proximity. The very first and original experimental work on this subject was carried out by Taylor (1909). It was the first time that the complexity of the hydrodynamic interaction was recognised and suggested for further evaluation. One of the most comprehensive and well-known publications was by Newton (1960). This paper discussed experimental work and full-scale trials that were carried out to determine the feasibility of side-by-side offloading in deep water. The impact of longitudinal and lateral separation on the interaction forces and moments was analysed and interpreted to establish the sequence of corrective rudder movements to maintain parallel courses. Brix (1987) presented a semi-empirical formulation for predicting interaction forces and moments during an overtaking manoeuvre based on his experimental work. Vantorre et al. (2001), Yasukawa and Yoshida (2011), Lataire et al. (2012) and Jin et al. (2016a) all carried out comprehensive studies on estimating ship-ship interaction forces and moments in calm waters considering a

wider range of parameters including Froude number, drift angle and relative positions. By performing regression analysis, a series of empirical formulae were derived for predicting peak values of the longitudinal and lateral forces and yaw moments. A further step forward from measuring interaction forces and moments, Kim et al. (2012) conducted model tests to investigate relative motions of the FLNG and LNG carrier in a side-by-side mooring configuration in waves. The study was conducted for a variety of environmental conditions including different current, wind and wave conditions. It was concluded that for safe operations of the cryogenic offloading arm, the relative motions between the two vessels must be reduced. Taking a similar experimental approach, Zhao et al. (2013) and Zhao et al. (2014) studied the hydrodynamics of a single point turret-moored FLNG system in tandem and side-by-side offloading conditions respectively. The two papers presented model tests investigating the influence of different positional configurations on the hydrodynamic performance of the offloading system. The results demonstrated that the mechanical properties of the connection between the FLNG and LNG play an important role on minimising the relative motions of the two vessels.

1.2.2 Inviscid potential flow based method

Experimental model tests conducted to date seldom measure the flow field and can be expensive and time-consuming although they provide direct and reliable predictions of the hydrodynamic forces and moments. This became the greatest motivation of developing numerical methods for further evaluation of the ship-ship interaction problem. The fundamental potential flow theory of ship-ship interaction was initiated by Tuck and Newman (1974) and Abkowitz et al. (1976). However, the applicability of these two potential flow methods was limited to cases with a flat free surface and their accuracy remains questionable when compared with experimental data. Kodan (1984) applied strip theory to describe the hydrodynamic interaction between two parallel slender structures in oblique waves. The paper provided calculations of the sectional interaction effects on the added mass, damping coefficient and wave exciting force by analysing the incoming radiation waves generated from oscillation of corresponding sections, and then integrated them to recover the overall interaction effects. This method was extended to the application of ship interaction problems in irregular waves. Kodan's theory was implemented by Fang and Kim (1986) by incorporating speed effect in their numerical method of analysing wave-induced motions on two hydrodynamically interacting slender bodies. In this work, the sectional procedure, including the hydrodynamic interaction and an integral equation, is utilized. The numerical results of the coupled motions of two ships were compared with the behaviour of a monohull to emphasise the significance of interaction effects. The study also revealed the validity of strip theory in predicting the interaction effects of closely spaced ships advancing in oblique waves.

In the above publications, the low frequency wave loads in particular, the wave drift forces and sloshing effects in confined water region between the two ships, were not properly addressed. Many researchers have been trying to develop methodologies to calculate second-order forces in the ship-ship interaction condition within the frame of potential flow theory. So far, it is well known that three different methods are available for computing the second-order steady wave forces: the near-field method based on the direction pressure integration, the far-field method based on the momentum-conservation principle and the hybrid middle-field method.

Fang and Chen (2002) proposed a far-field approach for the investigation of ship-ship interactions in regular waves adopting a three-dimensional source distribution method. The numerical solutions were compared with a two-dimensional approach based on the near field approach and experimental data. It was found that the three-dimensional method provided better predictions of interaction effects in the gap wave resonance region. The same methodology was employed in the research by Chen and Fang (2001) with more detailed explanation of the mathematical derivation. Kashiwagi (2004) applied the near-field method as well as a new far-field method for evaluating the wave drift forces and moments on two ships operating side-by-side. In addition, the paper employed a higher-order boundary element method for evaluating the first-order velocity potentials on the whole wetted surface of the ships. Good numerical accuracy between the newly developed far-field method and the near-field method was obtained. Adopting a similar numerical approach, Hong et al. (2005) analysed the motions and drift force of side-by-side moored vessels (LNG FPSO, LNGC and shuttle tankers) in regular and irregular waves. Their numerical approach was able to provide both frequency domain and time domain simulations. Chen (2005) developed the middle-field approach which can also be applied in the ship-ship interaction problems for predicting the hydrodynamic wave loads. The proposed method gave a more simplified formulation than the near-field method but with better numerical convergence than the far-field approach. The paper further emphasised the trapped water resonance phenomena and states that the resonance of the wave field in the confined zone between two floating bodies is due to the hydrodynamic interaction, wave kinematics annulled or amplified by complex scattering between bodies. The unrealistic free surface resonance motion magnifies the wave loads on the bodies and therefore can induce significant discrepancies in the numerical solution.

In order to maintain the realistic level of the wave motion in the confined zone, attempts have been made by previous researchers within the frame of potential flow theory. Buchner et al. (2001) first proposed an artificial rigid damping lid method to suppress the unrealistic wave kinematics in the confined water zone. However, the rigid lid erased all the wavy elevation beneath it and induced perturbation around its edges. To recover the realistic wave motions, Newman (2004) recommended a flexible lid based on a set of basis functions of Chebychev polynomials. By introducing a damping coefficient, the deformation of the free surface of the

confined water zone can be adjusted. Chen (2005) directly applied the equation of the fairly perfect fluid theory involving energy dissipation and taking into account the damping force in the boundary condition on the free surface. This methodology was named the 'epsilon' damping lid method and was integrated in the middle-field approach in the case study of a Wigley hull placed side-by-side with a barge to predict the wave drift force. The numerical solutions agree well with the experimental findings from Kashiwagi (2004). In spite of the successful application, the method remains to be an approximation to the dissipation mechanism which is the exact value of the damping parameter. It was suggested that this dissipation mechanism can be determined by tuning the algorithm and comparing to experimental measurements.

1.2.3 Viscous RANS based method

The potential flow methods discussed above all have common limitations as they barely solve for the viscous effects associated flow separation and nonlinear free-surface boundaries, which are regarded as the main sources of the discrepancies between the potential theory and experiments (Zhao et al., 2017). As computational power has grown rapidly in the past decade, RANS based CFD analysis has drawn much attention. The method accounts for viscous effects and is expected to perform more accurate predictions on the interaction forces and moments as well as the amplitudes of the gap waves without calibration of viscous damping using experimental data.

The RANS computation method has been extensively applied for studying single ship hydrodynamics. Orihara and Miyata (2003) conducted studies on the pitch and heave motions and added resistance for a S175 container ship by solving time dependent unsteady RANS (URANS) equations. The work demonstrated the capabilities of using the CFD RANS method to simulate ship motion responses in regular oblique waves. Similarly, Irvine Jr et al. (2008) investigated the pitch and heave motions of a surface combatant model in regular head sea waves using URANS technique. From the obtained results, an empirical formula was derived to predict the Froude number for maximum motion response as functions of ship geometry coefficients. Sadat-Hosseini et al. (2013) applied the method to predict the motion responses and added resistance of a KVLCC2 container ship in head sea waves for two conditions: fixed in surge and free to surge. By conducting local flow analyses, it was found that the added resistance was highly dependent on the pressure variation on the upper bow of the ship and correlated with bow relative motion. Simonsen et al. (2013) studied heave and pitch motions of a model scale KCS container ship in regular head waves by means of EFD and RANS computations. Model tests with uncertainty assessment were designed and conducted to validate numerical predictions on ship motion responses and added resistance. Extending the

work further. Simonsen et al. (2015) carried out URANS simulations on estimating added resistance of the KCS container ship in oblique waves.

In recent years, extensive studies have been carried out using RANS based method (steady and unsteady) on predicting ship-ship interaction forces and moments considering variables such as Froude number, drift angle and relative positions (Sadat-Hosseini et al., 2011a, Zou and Larsson, 2013, Jin et al., 2016a). This also includes computations performed by Mousaviraad et al. (2016a) and Mousaviraad et al. (2016b) on predicting ship-ship interactions during replenishment operations. Although the results exhibit good agreement with experimental data, the application of the CFD RANS based method has only been proven for limited interaction problems. The feasibility and accuracy of CFD modelling of ship-to-ship interactions in waves are needed to be further studied.

To date, the majority of RANS based analysis on ship-ship interactions are carried out in model scale in order to match up with experimental test conditions. However, model scale flows can show significant differences against full scale conditions due to scale effects. Hochkirch and Mallol (2013) highlights that the discrepancies between model scale and full scale CFD simulations can be found in boundary layers, flow separations and wave breaking behind transom sterns. Thus, performing full scale analyses on the ship-ship interactions is of crucial importance for obtaining more realistic force and moment estimations.

1.3 Research Objectives

Based on the literature review above, the hydrodynamics around multiple floating bodies are yet to be fully understood. A better understanding of the FLNG-LNG hydrodynamic interactions is of great advantage for the oil and gas industry for improving the efficiency, operability and survivability of such systems. In the light of this, the present study focuses on estimating the hydrodynamic loads acting on the FLNG-LNG system. The objectives of this research are summarised as:

- Develop a reliable numerical approach for simulating the hydrodynamics around the FLNG-LNG system in calm water steady current and in regular waves
- Perform experimental validation for the numerical computations on the prediction of wave loads and gap wave elevations
- Investigate the influences of longitudinal and lateral separations on the FLNG-LNG hydrodynamic interactions in calm water steady current and in regular waves
- Evaluate scale effects on the prediction of FLNG-LNG interaction forces and moments

- Assess the global performance of an integrated FLNG-LNG system exposed to real environmental conditions

1.4 Novel Aspects

This study provides contributions through the application of experimental and CFD methods to investigate the hydrodynamic performance of a conceptual FLNG-LNG offloading system. The novel aspects of this work include the following:

- The application of viscous RANS/URANS method on investigating the hydrodynamics around a conceptual FLNG-LNG system in calm water steady current and in regular waves is presented: This work is considered novel since viscous effects can be significant for ship-ship hydrodynamic interactions. Previous numerical studies were mostly based on PF theory with simple hull shapes.

- Physical measurements of wave loads on the FLNG-LNG system as well as gap wave responses provide sources of validation for the present and future computations. To date, there are limited experimental data available in the public domain.

- The feasibility of URANS computations on predicting the gap wave elevations between the FLNG and LNG vessels has been investigated. Existing method to address such problems is by tuning a numerical damping lid in a potential flow solver, which sometimes can be difficult and inconvenient.

- The details of the hydrodynamic interactions between the FLNG-LNG system for varying longitudinal and lateral offsets have been studied in calm water steady current and in regular waves. Such investigations have only been performed for ship lightering operations previously. In addition, it may help ship operators to determine the most favourable relative positions between the two vessels.

- The difference between model and full scale FLNG-LNG interactions in calm water steady current and in regular waves are quantified using viscous RANS/URANS computations. Existing experimental based methods can barely identify the influence of scale effects.

1.5 Thesis Outline

The thesis comprises eight chapters and one appendix, based on the key contents of a series of technical papers for publication. Chapters 4, 5, 6 and 7 are based on peer-reviewed publications and have been modified to fit within the thesis. The full publications are provided in the Appendix.

Chapter 2 and 3 provides the theory background of the numerical simulations and an overview of the experimental study. Chapter 4, 5, 6 and 7 discuss the details of the numerical work and corresponding computational results for predicting the hydrodynamic performance of either single FLNG/LNG or a side-by-side FLNG-LNG system in calm waters and waves.

Chapter 2 describes the fundamentals of the computational approaches in this study. For the PF method, the superposition of wave potentials for modelling ship-ship interactions is briefly explained. For the URANS method, the governing equations of continuum mechanics are summarised, together with the techniques for simulating multiphase incompressible flow. A short overview of the applied turbulence model is also presented.

Chapter 3 contains the physical model scale experimental work carried out in the AMC model test basin for investigating the hydrodynamics of single FLNG/LNG and a side-by-side FLNG-LNG system in waves.

Chapter 4 presents the hydrodynamic interaction forces and moment results of a side-by-side FLNG-LNG system in calm water steady current with a quasi-static RANS approach. The influences of varying relative longitudinal and lateral separations on the interaction forces and moments are quantified. The work also presents full scale computations on the FLNG-LNG hydrodynamic interactions for investigating the existence of scale effects.

Chapter 5 investigates the individual hydrodynamic performance of the FLNG and LNG vessel in regular head and oblique sea waves with URANS computations. The numerical methods for regular wave generation and the modelling of ship motions are discussed in detail. Scale effects on the wave induced loads and motions are addressed by comparing model and full scale computations. The URANS computational results are compared with PF and experimental data. The study outlines the feasibility and accuracy of URANS computations for predicting single ship motion responses in waves.

Chapter 6 adopts a similar URANS approach studying the hydrodynamic interactions between the FLNG and LNG in regular waves. The computed wave loads as well as gap wave elevations are compared with that from PF simulations and physical model scale experiments. Full scale computations are also performed for the investigation of possible scale effects. This chapter emphasises the advantages of URANS method over potential flow when predicting ship-ship interactions in waves.

Chapter 7 presents time domain analysis on the hydrodynamic performance of a side-by-side FLNG-LNG offloading system coupled with mooring lines, fenders and hawser connections based on PF method. The numerical simulation is carried out in full scale condition under a combined environment of wind, current and waves. The relative motions between the FLNG and LNG in the horizontal plane as well as the force responses of the hawsers, fenders and

moorings are estimated. Furthermore, the effects of varying hawser pretension and stiffness on the hydrodynamic performance of the vessels and the loads of the connection system are investigated.

Chapter 8 summarises the thesis and offers some conclusions and suggestions for future research.

Chapter 2 - Computational Methods

This chapter briefly presents the numerical approaches applied in this thesis. The hydrodynamics of the FLNG-LNG system has been analysed using inviscid PF theory and viscous URANS method. For the investigation of FLNG-LNG interactions in calm water steady currents, the RANS computations are primarily applied due to pronounced viscous effects. For the predictions of frequency domain wave loads on the FLNG-LNG system, both of the two numerical approaches are employed and compared. For rapid computation, the motion responses of the FLNG-LNG system coupled with mooring lines, fenders and hawsers are analysed using the potential flow based time domain solver.

2.1 Inviscid Potential Flow Method

The PF solver AQWA is employed to predict the wave-induced loads on the FLNG and LNG hulls. The code utilises 3D Green's function to analyse interactions between surface waves and offshore structures and has gained widespread recognition for its accuracy and efficiency. It is also capable of solving hydrodynamic interaction problems between multiple floating bodies in real seaways.

2.1.1 Frequency domain analysis

First-order wave frequency loads

The frequency dependent hydrodynamic coefficients of the FLNG-LNG offloading system, such as added mass, damping and the first-order wave frequency loads are calculated based on the source distribution method. The hydrodynamic interaction problem is considered as a superposition of the radiation potentials from each individual structure. By adding the incident, diffracted and radiated waves together, the fluid flow field surrounding a floating multi-body system is given as:

$$\varphi(\bar{x})e^{-i\omega t} = \left[(\varphi_I + \varphi_D) + \sum_{m=1}^{M}\sum_{j=1}^{6} \varphi_{Rjm}\, x_{jm} \right] e^{-i\omega t} \tag{2.1}$$

Where $\bar{x} = (x, y, z)$ is an arbitrary point, ω is the wave frequency, φ_I is the space dependent incident wave potential, φ_D is the diffraction wave potential, x_{jm} is the amplitude of motion

of the j-th degree of freedom of the m-th structure. φ_{Rjm} is the radiation potential due to the unit j-th motion of the m-th structure. Here, both of the diffraction and radiation wave potentials are solved by a boundary integration approach utilising the frequency domain pulsating Green's function. Upon the fluid flow potential $\varphi(\bar{x})$, the first order hydrodynamic pressure distribution was calculated based on the linearized Bernoulli's equation.

$$p^{(1)} = i\,\omega\,\rho\,\varphi\,(\bar{x})\,e^{-i\omega t} \tag{2.2}$$

From the pressure distribution, the first order hydrodynamic force and moment components is expressed in a generalised form,

$$F_j^{(1)}\,e^{-i\omega t} = -\int_{S_0} p^{(1)}\,n_j\,dS = [\,-i\,\omega\,\rho \int_{S_0} \varphi(\bar{x})\,n_j\,dS\,]\,e^{-i\omega t} \tag{2.3}$$

where S_0 is the mean wetted surface area of the body, n_j is the unit normal vector on the j-th motion. From Equation (2.3), the Froude-Krylov force F_I and diffraction force F_D are derived.

$$F_{Ij} = -i\,\omega\,\rho \int_{S_0} \varphi_I\,(\bar{x})\,n_j\,dS \tag{2.4}$$

$$F_{Dj} = -i\,\omega\,\rho \int_{S_0} \varphi_D\,(\bar{x})\,n_j\,dS \tag{2.5}$$

The radiation force F_R due to radiation wave induced by the k-th unit amplitude body rigid motion is,

$$F_{Rjk} = -i\,\omega\,\rho \int_{S_0} \varphi_{Rk}\,(\bar{x})\,n_j\,dS \tag{2.6}$$

The radiation potential φ_{Rjm} from Equation (2.1) can also be expressed in real and imaginary parts to produce the added mass $A_{jm,k}$ and damping $C_{jm,k}$ coefficients,

$$A_{jm,k} = \frac{\rho}{\omega} \int_{S_0} Im[\,\sum_{m=1}^{M}\sum_{j=1}^{6} \varphi_{Rjm}\,x_{jm}\,]\,n_j\,dS \tag{2.7}$$

$$C_{jm,k} = -\rho \int_{S_0} Re\,[\sum_{m=1}^{M}\sum_{j=1}^{6} \varphi_{Rjm}\,x_{jm}]\,n_j\,dS \tag{2.8}$$

Mean and slow wave drift forces

The second order wave drift force is solved by the near field approach based on the mean wetted body surface integration method (Pinkster, 1979). Under the assumption of potential flow, the fluid motions may be described by a velocity potential.

$$\varphi = \varepsilon \varphi^{(1)} + \varepsilon^2 \varphi^{(2)} + \ldots \tag{2.9}$$

where ε represents the perturbation parameter close to zero. Assuming that the body is carrying out small amplitude motion about the mean position, the first and second order components of the pressure at a point on the hull may be expressed as,

$$p^{(1)} = -\rho g X_3^{(1)} - \rho \varphi^{(1)} \tag{2.10}$$

$$p^{(2)} = -\rho g X_3^{(2)} - \rho \varphi^{(2)} - \frac{1}{2} \rho \left|\nabla \varphi^{(1)}\right|^2 - \rho (\overline{X}^{(1)} \cdot \nabla \varphi^{(1)}) \tag{2.11}$$

where $\overline{X}$ and X_3 represent the linear motion vector and the vertical co-ordinate of the point respectively. Integrating $p^{(2)}$ over the wetted surface S_0, the second order wave drift force is derived as,

$$F_j^{(2)} = -\frac{1}{2} \rho g \int_{WL} \zeta_r^{(1)2} n_j \, dl + \alpha^{(1)} ? F_j^{(1)} - \iint_{S_0} [(-\frac{1}{2} \rho \left|\nabla \varphi^{(1)}\right|^2) - \rho (\overline{X} \cdot \nabla \varphi^{(1)}) - \rho (\varphi^{(2)})] n_j \, dS \tag{2.12}$$

where $\zeta^{(1)}$ is the first order relative wave height and $\alpha^{(1)}$ is the first order rotation motion. The second order wave drift force in Equation (2.12) contains three components: 1) the line integral around the static waterline of the vessel of the square of the relative wave height, 2) a momentum term from the first order wave force due to the different axes to which the second order force is referenced, and 3) integration of all second order hydrodynamic pressures over the mean submerged part of the hull from Bernoulli equation. In irregular waves, the second order wave drift force may also be expressed in the form of quadratic transfer function (QTF) as,

$$F^{(2)}(t) = \sum_{a=1}^{N} \sum_{b=1}^{N} \zeta_a \zeta_b P_{ab} \cos\{(\omega_a - \omega_b) t + (\varepsilon_a - \varepsilon_b)\} + \sum_{a=1}^{N} \sum_{b=1}^{N} \zeta_a \zeta_b Q_{ab} \sin\{(\omega_a - \omega_b) t + (\varepsilon_a - \varepsilon_b)\} \tag{2.13}$$

where P_{ab} and Q_{ab} are the in-phase and out-phase component of the QTF. With the spectral density $S\zeta(\omega)$ of the irregular waves being specified, the mean second order wave drift force is determined when $\omega_a = \omega_b = \omega$,

$$F_{mean}^{(2)} = 2\int_0^{\infty} S_\zeta(\omega)\left[\frac{F^{(2)}}{\zeta_a\ \zeta_b}(\omega,\omega)\right]d\omega \tag{2.14}$$

while the spectral density of the low frequency wave drift force follows,

$$S_F(\omega_a - \omega_b) = 8\int_0^{\infty} S_\zeta(\omega_a)\, S_\zeta(\omega_a)\left[\frac{F^{(2)}}{\zeta_a\ \zeta_b}(\omega_a,\omega_b)\right]^2 d\omega \tag{2.15}$$

where $\left[\frac{F^{(2)}}{\zeta_a\ \zeta_b}(\omega,\omega)\right]$ is the mean wave drift force QTF in regular waves of frequency ω and is equivalent of $\sqrt{P_{ab}^2 + Q_{ab}^2}$ with $\omega_a = \omega_b$: $\left[\frac{F^{(2)}}{\zeta_a\ \zeta_b}(\omega_a,\omega_b)\right]$ is the low frequency wave drift force QTF and is equivalent of $\sqrt{P_{ab}^2 + Q_{ab}^2}$ with $\omega_a \neq \omega_b$.

2.1.2 Time domain analysis

The coupling effects of vessels and mooring systems have been modelled through numerical time domain simulations. The motion equations in the time-domain coupled analysis for the FLNG vessel and LNG carrier are formulated as:

$$(M + a_\infty)\,\ddot{\mathbf{X}}(t) + C\,\dot{\mathbf{X}}(t) + K\,\mathbf{X}(t) + \int_0^t \mathbf{R}(t-\tau)\,\dot{\mathbf{X}}(\tau)\,d\tau = \mathbf{F}^{wave} + F^{current} + F^{wind} \tag{2.16}$$

where M is the structural mass matrix, a_∞ is the fluid added mass matrix at the infinite frequency, C is the damping matrix including the linear radiation damping effects, K is the total stiffness matrix, F^{wind} and $F^{current}$ are the wind and current forces estimated from the standardized OCIMF (1994) data, and $R(\tau)$ is the retardation function computed by the frequency depended added mass $a(\omega)$ and damping $C(\omega)$.

$$R(\tau) = \frac{1}{2\pi}\int_{-\infty}^{\infty}[C(\omega) + i\,\omega\,a(\omega)]\,e^{i\omega t}\,d\omega \tag{2.17}$$

The coupled analysis is carried out with a time step of 0.2 s based on the convergence test and recommendations in the research performed by Zhao et al. (2014). The mooring lines are modelled by non-linear catenary equations. Simultaneously, to maintain the side-by-side offloading configuration, simple linear force-elongation relationships are given to the hawsers and fenders.

2.2 Viscous URANS Method

2.2.1 Governing equations

The governing equations for the two phase incompressible flow combining air and water are given by the URANS equations coupled with the conservation of continuity (Rusche, 2003):

$$\frac{\partial \rho \mathbf{u}}{\partial t} + \nabla \cdot [\rho \mathbf{u}\mathbf{u}] = -\nabla p^* - \mathbf{g} \cdot \mathbf{x} \nabla \rho + \nabla \cdot [\mu \nabla \mathbf{u} + \rho \boldsymbol{\tau}] + \sigma_T \kappa_\gamma \nabla_\gamma \tag{2.18}$$

$$\nabla \cdot \mathbf{u} = 0 \tag{2.19}$$

Here, $\mathbf{u} = (u,v,w)$ is the velocity field in Cartesian coordinates, p^* represents the pressure including hydrostatic, $\rho = \rho(\mathbf{x})$ is the fluid density which varies with the content of air/water in the computational cells, $\mathbf{x} = (x, y, z)$ are the Cartesian coordinates, $\mathbf{g}$ is the gravitational acceleration, μ is the dynamic molecular viscosity and $\boldsymbol{\tau}$ is the Reynolds stress tensor:

$$\boldsymbol{\tau} = \frac{2}{\rho} \mu_t \mathbf{C} - \frac{2}{3} k \mathbf{I} \tag{2.20}$$

where μ_t is the dynamic eddy viscosity, $\mathbf{C} = (1/2\ (\nabla \mathbf{u} + (\nabla \mathbf{u})^T))$ is the fluid strain rate tensor and k is the turbulent kinetic energy per unit mass, ∇ is the gradient operator $(\partial/\partial x, \partial/\partial y, \partial/\partial z)$, $\mathbf{I}$ is the identity matrix. The last term in Equation (2.18) represents surface tension, where σ_T is the surface tension coefficient which is 0.074 kg/s^2 between air and water at 20°C and κ_γ is the surface curvature. The presence of surface tension will only have minor effects in large scale engineering applications (Jacobsen et al., 2012).

2.2.2 Two-phase VOF method

The above equations are solved for air and water simultaneously, where the fluids are tracked using the volume of fraction γ. γ is 0 for air and 1 for water, and any intermediate value is a mixture of the two fluids. The distribution of γ is modelled by an advection equation:

$$\frac{\partial \gamma}{\partial t} + \nabla \cdot [\mathbf{u}\gamma] + \nabla \cdot [\mathbf{u}_r \gamma (1-\gamma)] = 0 \tag{2.21}$$

The last term on the left-hand side is a compression term, which limits the smearing of the interface, and $\mathbf{u}_r$ is the relative velocity vector. Using γ, the spatial variation in fluid properties, such as ρ and μ, can be derived through weighting:

$$\rho = \gamma\, \rho_{water} + (1+\gamma)\, \rho_{air} \tag{2.22}$$

$$\mu = \gamma\, \mu_{water} + (1+\gamma)\, \mu_{air} \tag{2.23}$$

2.2.3 Turbulence modelling

The closure of the URANS equations is achieved using the Shear-Stress Transport (SST) k-ω turbulence model on the basis of the description by Menter (1994) and Wilcox (2008), where k is the turbulent kinetic energy and ω is the characteristic frequency of the turbulence. The transport equation for k and ω for turbulent flows at high Reynolds is as follows:

$$\frac{\partial(\rho\, k)}{\partial t} + \mathrm{div}(\rho\, k\, \mathbf{u}) = \mathrm{div}\left[\left(\mu + \frac{\mu_t}{\sigma_k}\right) \mathrm{grad}(k)\right] + P_k - \beta^*\, \rho\, k\, \omega \tag{2.24}$$

$$\frac{\partial(\rho\, \omega)}{\partial t} + \mathrm{div}(\rho\, \omega\, \mathbf{u}) = \mathrm{div}\left[\left(\mu + \frac{\mu_t}{\sigma_{\omega,1}}\right) \mathrm{grad}(\omega)\right] + \gamma_2 \left(2\, \rho\, \mathbf{S_{ij}} \cdot \mathbf{S_{ij}} - \frac{2}{3}\, \rho\, \omega\, \frac{\partial U_i}{\partial x_j}\, \delta_{ij}\right) - \beta_2\, \rho\, \omega^2 + 2\, \frac{\rho}{\sigma_{\omega,2}\, \omega} \frac{\partial k}{\partial x_k} \frac{\partial \omega}{\partial x_k} \tag{2.25}$$

where,

$$P_k = \left(2\, \mu_t\, \mathbf{S_{ij}} \cdot \mathbf{S_{ij}} - \frac{2}{3}\, \rho\, k\, \frac{\partial U_i}{\partial x_j}\, \delta_{ij}\right) \tag{2.26}$$

2.2.4 Numerical uncertainty assessment

The numerical uncertainties in the present RANS/URANS computations are assessed following the procedures provided in Wilson et al. (2001) and Stern et al. (2001). It is assumed that the numerical uncertainty U_{SN} comprises of iterative convergence uncertainty U_I, grid uncertainty U_G and time-step uncertainty U_T, giving the following expression:

$$U_{SN}^2 = U_I^2 + U_G^2 + U_T^2 \tag{2.27}$$

Tezdogan et al. (2015) estimated the iterative convergence uncertainty for container ship motion response simulations in Star-CCM+ URANS solver. Their analysis indicates U_I of less than 0.5% in simulation results, which is considered to be negligible. As similar computational settings are applied, the grid and time-step uncertainties are of primary interest. The grid and time-step convergence study are both conducted with triple solutions systematically. The grid uncertainty analysis is performed with the smallest time-step, whilst the time-step independence study is carried out with the finest mesh. Variations of simulation results (S)

between the fine (1), medium (2) and coarse (3) grids with refinement ratio of r_G are identified as:

$$\varepsilon_{G_{21}} = S_2 - S_1 \tag{2.28}$$

$$\varepsilon_{G_{32}} = S_3 - S_2 \tag{2.29}$$

The numerical convergence ratio can be calculated from Equation (2.30).

$$R_G = \varepsilon_{G_{21}} / \varepsilon_{G_{32}} \tag{2.30}$$

Depending on the value of the convergence ratio, four conditions can be predicted.

(i) $0 < R_G < 1$, monotonic convergence

(ii) $R_G < 0$; $|R_G| < 1$ oscillatory convergence

(iii) $1 < R_G$, monotonic divergence

(iv) $R_G < 0$; $|R_G| > 1$ oscillatory divergence

It is noted that for divergence conditions (iii) and (iv), the numerical uncertainty cannot be estimated. For the oscillatory convergence (ii), the numerical uncertainty can be estimated by bounding the error based on oscillation with upper limit S_U and lower limit S_L using Equation (2.31),

$$U_G = \left| \frac{1}{2} (S_U - S_L) \right| \tag{2.31}$$

For convergence condition (i), the generalized Richardson's extrapolation can be employed to estimate the numerical error $\delta^*_{RE_{G1}}$ and order of accuracy p_G as,

$$\delta^*_{RE_{G1}} = \frac{\varepsilon_{G_{21}}}{r_G^{p_G} - 1} \tag{2.32}$$

$$p_G = \frac{\ln(\varepsilon_{G_{32}} / \varepsilon_{G_{21}})}{\ln(r_G)} \tag{2.33}$$

There are two ways to estimate the numerical uncertainty depending on whether the solutions are close to the asymptotic range. This is determined by the correction factor C_G defined as,

$$C_G = \frac{r_G^{p_G} - 1}{r_G^{p_{Gest}} - 1} \tag{2.34}$$

where p_{Gest} is an estimate for the limiting order of accuracy. If C_G approaches unity, the solutions are close to the asymptotic range. In this case, the numerical error δ^*_{SN}, benchmark result S_C and uncertainty U_{GC} can be estimated from.

$$\delta^*_{SN} = C_G \; ? \; \delta^*_{RE_{G1}} \tag{2.35}$$

$$S_C = S - \delta^*_{SN} \tag{2.36}$$

$$U_{GC} = \begin{cases} (2.4(1-C_G)^2+0.1)\left|\delta^*_{RE_{G1}}\right| & \left|1-C_G\right| < 0.125 \\ \left|1-C_G\right|\left|\delta^*_{RE_{G1}}\right| & \left|1-C_G\right| \geq 0.125 \end{cases} \tag{2.37}$$

when C_G is sufficiently greater than 1, which means the solutions are far away from the asymptotic range, the numerical uncertainty U_G can be calculated from Equation (2.38).

$$U_G = \begin{cases} (9.6(1-C_G)^2+1.1)\left|\delta^*_{RE_{G1}}\right| & \left|1-C_G\right| < 0.125 \\ (2\left|1-C_G\right|+1)\left|\delta^*_{RE_{G1}}\right| & \left|1-C_G\right| \geq 0.125 \end{cases} \tag{2.38}$$

Based on similar procedures as above, the time step uncertainty U_T can be estimated. To validate the URANS/RANS computations, it is necessary to check if the absolute comparison error E between numerical and experimental results is smaller than the validation uncertainty U_V calculated as a combination of numerical uncertainty U_{SN} and experimental uncertainty U_D.

$$U_V = \sqrt{U^2_{SN} + U^2_D} \tag{2.39}$$

Chapter 3 - Experimental Study

3.1 FLNG and LNG models

In this study, the MarAd systematic series full-form ship models from Roseman (1987) are used to represent a generic FLNG hull design and a LNG shuttle tanker which operates alongside the FLNG. The hull forms are shown in Figure 3.1. The modelled full scale FLNG has an overall length of 422 m and a displacement of approximately 600,000 tonnes at its fully loaded condition. At the same time, the LNG carrier is studied for an empty hull condition ready for the liquid cargo to be loaded. The geometry particulars of the LNG and FLNG are illustrated in Table 3.1. The stretched MarAd F series here represents a MarAd F series hull where the parallel middle body has been lengthened by 24.0% in the x direction, but the maximum beam and depth remain the same ratio as the original.

Table 3.1 Geometry particulars of FLNG and LNG

	FLNG		*LNG*	
Hull form	**MarAd F series**		**Stretched MarAd F series**	
Scale	FS	MS	FS	MS
L_{OA} (m)	422.0	4.22	323.9	3.24
L_{pp} (m)	400.0	4.00	300.0	3.00
B (m)	72.8	0.728	45.1	0.451
D (m)	36.4	0.364	28.2	0.282
T (m)	24	0.240	10	0.100
C_B	0.85	0.85	0.875	0.875
LCG (m)	232.4	2.324	181.4	1.814
VCG (m)	18.5	0.185	7.0	0.07
K_{xx}/B	0.32	0.32	0.39	0.39
K_{yy}/L_{pp}	0.25	0.25	0.23	0.23
K_{zz}/L_{pp}	0.25	0.25	0.23	0.23

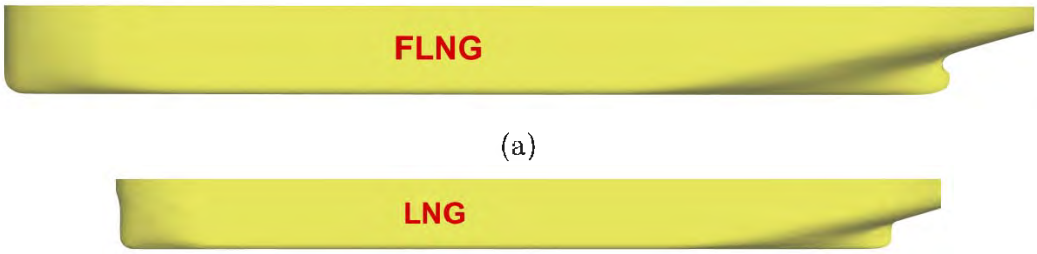

Figure 3.1 Hull geometry of studied generic (a) FLNG and (b) LNG

3.2 Experiment set up

The model tests were performed at the Model Test Basin at the Australian Maritime College, University of Tasmania (Figure 3.2). The basin is 35 m long, 12 m wide, and has a flat bottom with maximum water depth of 1.0 m. The water depth set for the tests in this study was 0.8 m, which corresponds to the water depth draft ratio of d/T_{FLNG}=3.3 or d/T_{LNG}=8.0. Regular waves were generated by a multi-element wavemaker with 16 paddles. The model tests were carried out at the scale of 1:100 for both FLNG and LNG models. The objective of these tests is to validate the setup for the CFD computations.

The experiments were conducted according to ITTC recommended procedures (ITTC, 2005). Figure 3.3 and Figure 3.4 give an overview of the model test setup in the model test basin. Wave energy dissipation devices were located at the end side of the basin to reduce the influence of wave reflection.

For testing the individual FLNG/LNG in regular waves, the model was mounted to a carriage by a starboard forward post, a port forward post and an aft post. Force transducers were placed at the base of the posts for the measurement of wave loads. Ball joints were used to connect the base of the load cells to the ship model. The aft ball joint incorporated a slide oriented parallel to the longitudinal centreline of the model. The forward starboard ball joint incorporated a slide oriented perpendicular to the aft slide. The port ball joint did not incorporate a slide. The forward and aft post connections were located at the ship model's VCG. For the free heave and pitch tests, the posts were free to move vertically so the ship was able to heave and pitch in waves. Linear variable differential transducers (LVDTs) were attached to the posts in order to measure the vertical displacement of the vessel. For the motion restricted cases, the posts were fixed in the vertical plane, constraining the model in 6 DoF motions.

For testing the FLNG-LNG interactions in waves, the two models were mounted to the carriage in the same way as for testing a single ship model. The motions of the FLNG and

LNG were constrained in 6 DoF. Wave probes were placed between the two vessels for measuring the gap wave elevations at different incoming wave conditions. The positions of probes relative to the LCG of the FLNG are given in Table 3.2. In order to obtain accurate wave elevation measurements, wave probes were calibrated on a daily basis before testing. For the load cells, calibrations were performed at the beginning and at the end of the testing program.

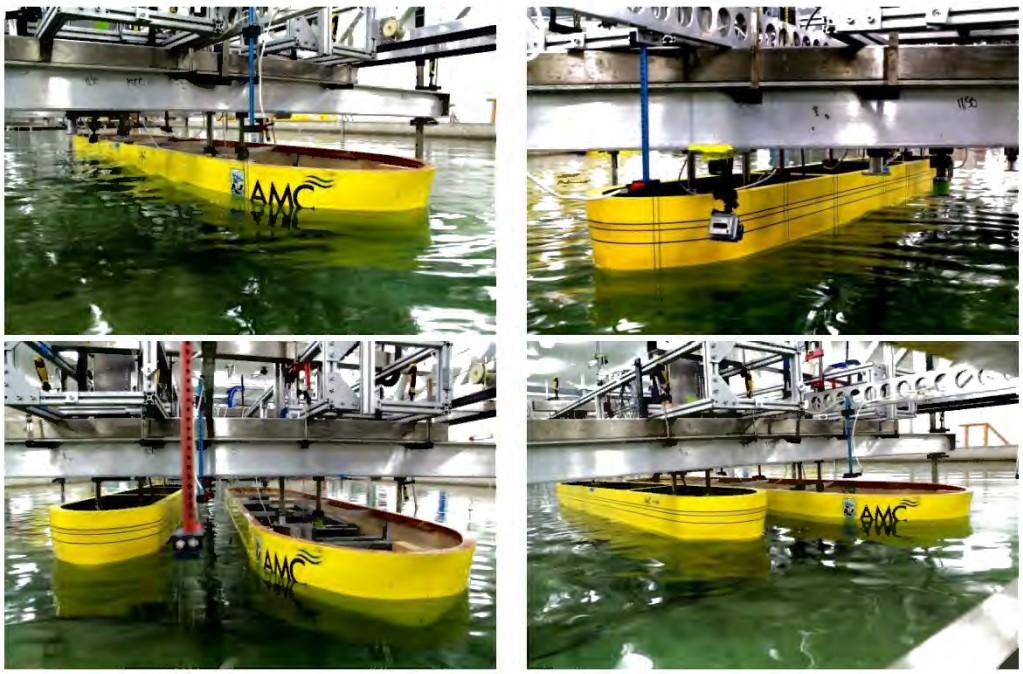

Figure 3.2 Physical model tests in the AMC Model Test Basin

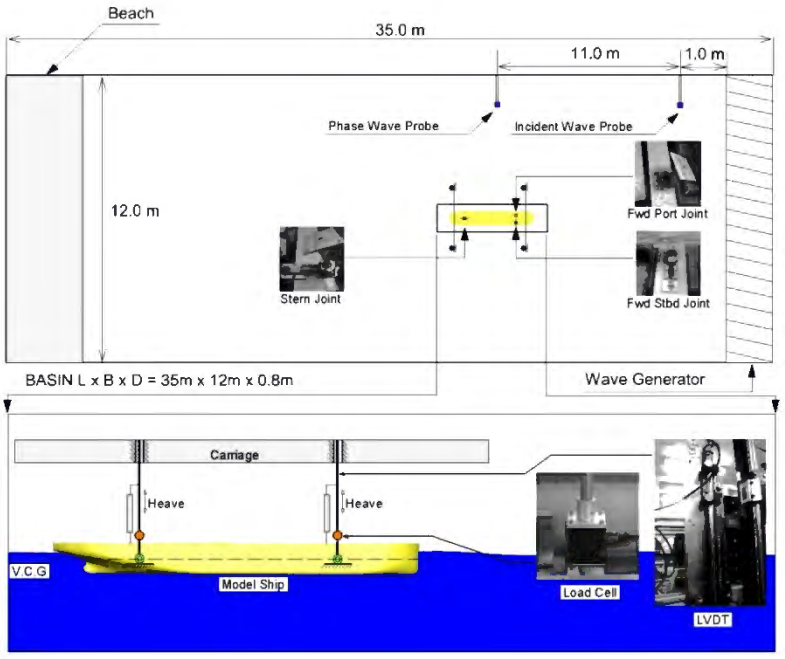

Figure 3.3 Schematic illustration of experimental setup for studying single FLNG/LNG

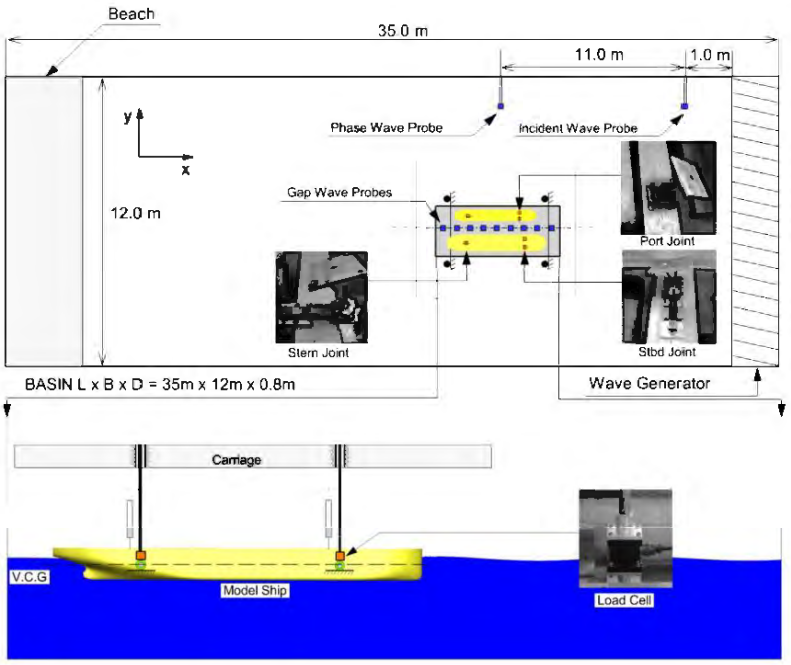

Figure 3.4 Schematic illustration of experimental setup for studying FLNG-LNG interaction

Table 3.2 Positons of the wave probes relative to the LCG of the FLNG parallel to the x-axis

Wave probe	1	2	3	4	5	6	7	8	9	10
Position (m)	2.39	1.59	0.99	0.59	-0.02	-0.41	-1.01	-1.41	-2.01	-2.83

3.3 Test procedure and data acquisition

Initial readings of all instruments were taken prior to each run and were checked between runs to ensure that no notable drift had existed. Sufficient time was allowed between consecutive runs to achieve calm water conditions. Data acquisition commenced after the regular waves had propagated to about 5 m forward of the ship model. The sample rate for the LVDTs and load cells was set at 200 Hz throughout the model test program. The wave loads for each test run were derived afterwards from the time series, selecting a time window where the phase wave probe exhibited consistent sinusoidal readings.

3.4 Testing matrix

The testing matrices for measuring wave loads on single FLNG/LNG vessel and the FLNG-LNG side-by-side offloading system are presented in Section 5.3 and Section 6.3 respectively.

Chapter 4 - FLNG-LNG Interaction in Calm Water Steady Current

In this chapter, computations are presented for a scenario to represent a conceptual FLNG-LNG offloading system anchored in open calm water and exposed to a steady current. To simplify the computations each ship is fixed in all degrees of freedom. Initially, a preliminary study is carried out for five benchmark test cases conducted by Lataire et al. (2009) at the Flanders Hydraulics Research (FHR). Comparisons are made with model test measurements and existing CFD predictions by Sadat-Hosseini et al. (2011b) at the University of IOWA and Zou and Larsson (2013) from Chalmers University of Technology for validation. Based on the model, a series of systematic computations on the FLNG-LNG interactions are performed, focusing on investigating the influence of the relative longitudinal and transverse positions of the interacting hulls. Furthermore, full scale CFD simulations are presented and compared with model scale results, illustrating the existence of scale effects when predicting FLNG-LNG interaction forces and moments in steady current.

4.1 Computational domain, boundary conditions and grid

The computational domain is designed with respect to the dimensions of the towing tank at FHR and Zou and Larsson (2013) numerical study on ship-ship interactions in shallow water. It incorporates two ship hulls and is proven to be feasible in modelling the asymmetric flow field induced by the hydrodynamic interactions. A schematic of the fluid domain is shown in Figure 4.1.

A double body approximation method is adopted for investigating the ship-ship interactions considering the Froude numbers of the studied cases are all relatively small. The top of the domain is set as a symmetry plane representing a flat free surface at $z = 0$. Sinkage and trim are neglected since the current speeds considered in this study are very low. Velocity inlet condition is applied at the upstream of the fluid domain generating steady current. At the downstream, a pressure outlet boundary is imposed. The bottom and sides of the domain are all selected as slip-wall boundaries, which gives zero velocity gradient and zero normal velocity components.

The computational grid is generated according to CD-Adapco (2014) recommendations of virtual towing tank simulations. An illustration of the grid distribution is given in Figure 4.2. Slow cell growth rate is selected to create smooth mesh transition between the refined hull surfaces and the outer boundaries. Hexahedral trimmer and surface remesher are adopted to generate global volume mesh as well as local refinements. To resolve the turbulent boundary layers, prism layer mesher is utilised achieving y+ value of less than 1 along the hull for all computations.

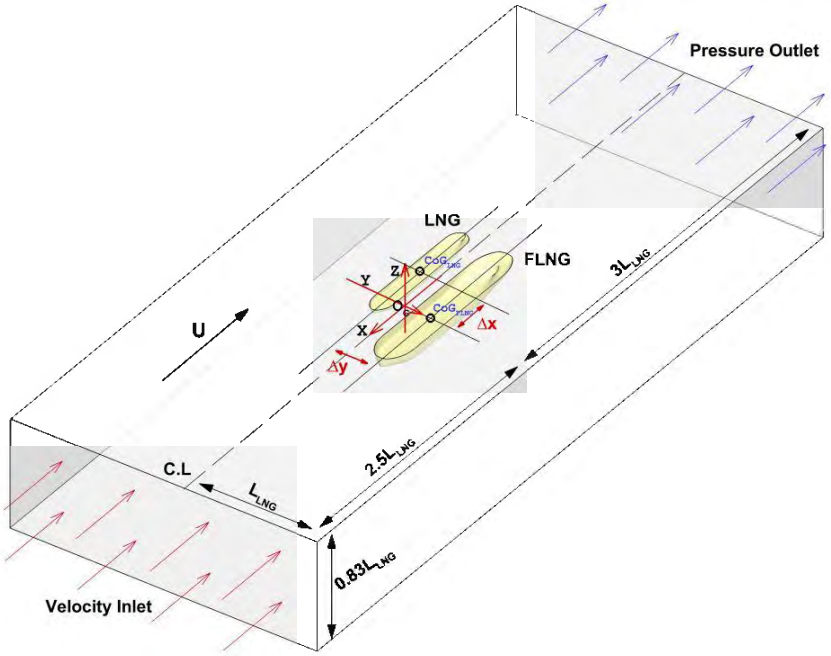

Figure 4.1 Global coordinate system and dimensions of the computational domain

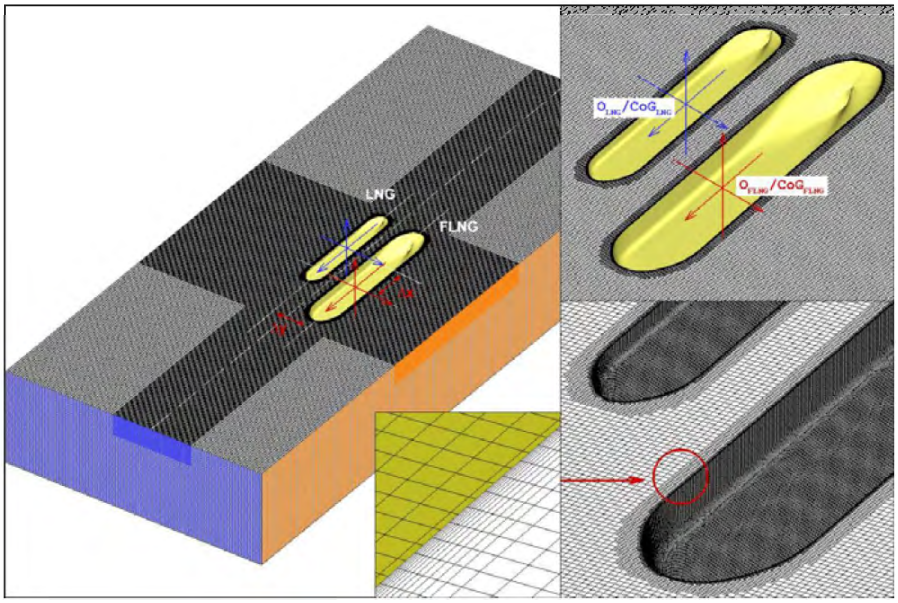

Figure 4.2 Illustration of computational grid for FLNG-LNG interaction simulations

4.2 Benchmark ship-ship interaction cases

CFD computations of five benchmark model tests are firstly carried out for validation of the current numerical approach. The tests are conducted at FHR studying the lightering operation of a KVLCC2 (2nd version of the KRISO Very Large Crude-oil Carrier) vessel and an Aframax tanker appended with rudder and propeller at constant forward speeds. The nature of the tested lightering conditions is regarded to be highly similar to that of ship-ship interaction cases in steady current. The ship hull geometries are provided by FHR with a scale factor of 1/75. For more detailed ship hull data, reference can be made to Lataire et al. (2009).

4.2.1 Benchmark case description

During the physical model scale tests, the KVLCC2 model was treated as the reference hull and placed at 1.007 m from the centre of the towing tank. The position of the Aframax tanker was then adjusted to obtain different longitudinal and lateral staggers for measurement. Table 4.1 lists the five benchmark test conditions that are adopted in our preliminary computations. It should be noted that a wide range of interaction conditions are covered in these benchmark cases including different draft, water depth, propeller rates. The propeller induced flow is modelled using the virtual disk method in Star-CCM+, which introduces a momentum source by defining the thrust torque curve and rotation rate of the propeller (CD-Adapco, 2014). The tested flow speed corresponds to full scale velocities of 4.0, 5.0 and 6.0 knots, which represents typical operational conditions during a lightering situation.

Table 4.1 Benchmark test conditions for preliminary CFD study

Conditions	Test A	Test B	Test C	Test D	Test E
h (m)	0.23	0.27	0.48	0.37	0.48
$T_{Aframax}$ (m)	0.10	0.20	0.20	0.10	0.10
T_{KVLCC2} (m)	0.17	0.17	0.17	0.28	0.28
β_{Aframx} (°)	0	0	0	2	0
β_{KVLCC2} (°)	0	0	0	0	0
U (m/s)	0.36	0.30	0.24	0.24	0.36
Fr	0.065	0.054	0.043	0.043	0.065
Re ($\times 10^6$)	1.09	0.91	0.73	0.73	1.09
$\Delta x/L_{Aframax}$	0	0	0	0	0.500
$\Delta y/L_{Aframax}$	0.43	0.43	0.23	0.32	0.32
$n_{Aframax}$ (RPM)	588	384	432	273	410
n_{KVLCC2} (RPM)	344	287	249	249	345

4.2.2 Benchmark computational results

Comparisons are made between the computational results and that obtained from literature for the benchmark lightering cases, focusing on the predictions of hydrodynamic forces and moments including surge force X, sway force Y, roll moment K and yaw moment N. The results are listed in Table 4.2 where S_A stands for the simulation results from current study, S_C and S_I denote the computed values from Chalmers and IOWA and D represents the experimental data from FHR. The sign conventions of S_C, S_I and D are corrected to be consistent with the coordinate system of S_A for comparison. It is also worth mentioning that there was no measurement of K for KVLCC2 from FHR and the IOWA results are available only for Tests A, B and E.

In addition, quasistatic surface elevations are estimated from the hydrodynamic pressure on the double model symmetry plane for the present study. The obtained wave patterns are also referred to Bernoulli waves or symmetric disturbances in Zou and Larsson (2013) work. Comparisons of experimental and computational predictions on wave elevations at the three longitudinal cuts are made for Test B and D as illustrated in Figure 4.3. As can been seen in Test B (Figure 4.3(a)), the adopted RANS approach predicts the wave elevations very well when compared with measured data. In Test D (Figure 4.3(b)), the computed elevation correlates very well with the experimental data for wave cut 1. For wave cut 2, the RANS method under-estimates the wave pattern and for wave cut 3, an over-prediction on the surface elevation is observed. It is also interesting to mention here that the quantitative measurements of the computed wave pattern for test D is extremely close to that published in Zou and Larsson (2013)'s paper using a similar CFD approach.

Benchmark Test cases A and B have the same relative positional configuration but different water depth conditions. The under-keel-clearance (UKC) of KVLCC2 for Test A is smaller than that in Test B, while the opposite is true for the Aframax hull. According to a previous study by Zou et al. (2011), surge force X is the greatest for small UKC. This trend is seen in the three sets of computational results: the resistance X is reduced for KVLCC2 and increased for the Aframax from Test A to Test B. However, the experimental data shows an unexpected decrease in X for the Aframax and relatively large deviations from the numerical results. The obtained sway forces on the KVLCC2 and Aframax are in opposite directions for both Test A and Test B, which indicates strong suctions between the two ships. This is also evident from the pressure contours as shown in Figure 4.4(a) and (b) where a low pressure zone was captured between the KVLCC2 and Aframax hull. The average difference of Y between S_A and S_C is 14.0%, while the discrepancy between S_A and D is estimated to be 23.0%. Similarly, in Tests A and B, the computed yaw moments N for the Aframax and KVLCC2 are showing opposite directions. For the Aframax, negative yaw moments are obtained from model testing

and CFD, meaning aft-body of the vessel is approaching the KVLCC2. For the KVLCC2, positive yaw moments are captured for both testing conditions, indicating the stern of the ship is approaching that of the Aframax. It is also seen that the computed yaw moment results show better agreement with experimental values for Test B rather than Test A. For the roll moment K, the measured values in both tests are negligible. However, it is interesting to see that the three computational approaches give similar predictions with an average deviation of 12%.

In Test C, as given in the benchmark test description, the gap between the Aframax and KVLCC2 is the smallest. Again, the present numerical predictions on the hydrodynamic forces and moments show consistency with Chalmers results, Sc, but relatively large discrepancies are observed compared with model testing data D. When comparing against tests A and B, the computational results indicate a decrease in the resistance for the two hulls. According to Zou and Larsson (2013), this is due to the fact that the water escapes the narrow channel between the two vessels and passes below or around the two ships. Also, the considerably small Δy results in high velocity flow field between the Aframax and KVLCC2, consequently introducing pressure gradients between the port and starboard side of the vessels, therefore producing a strong suction force. This is proven by the pressure contour plot in Figure 4.4(c) as well as the sway force in Table 4.2. The captured yaw moments for the Aframax and KVLCC2 acted in the same directions as they are predicted in Tests A and B and again this means the aft-body of the two ships are turning into each other.

As for Test D, the two ships are separated laterally by a relatively larger distance; therefore the hydrodynamic interaction between the Aframax and KVLCC2 is not as pronounced as it is for Test C, which results in less sway force, roll moment and yaw moment. It can be seen from Table 4.2 that the present computation shows better correlation with experimental data than Chalmers for resistance X and yaw moment N, but under-predicts the sway force acting on the KVLCC2 hull. Another important feature for Test D to be addressed is that the Aframax has a 2° drift angle with bow turning towards the KVLCC2. This is the primary reason for the small yaw moment captured on the Aframax hull. The bow-in configuration induces reverse pressure gradient on the starboard side of the Aframax which balances the yaw moment that tends to make the ship's aft-body turn towards the KVLCC2 (Figure 4.4(d)).

For Test E, current computational results agree well with the IOWA and Chalmers CFD data. As the Aframax has been moved forward dramatically for this configuration, the captured suction force between the two ships is not as significant as it was for the previous test cases. However, strong yaw moment that tends to turn the stern of the Aframax towards to the bow of the KVLCC2 is observed. This moment is generated by the low pressure zone between the stern of the Aframax and the bow of the KVLCC2 as shown in Figure 4.4(e). Once again, small roll moment values are captured for both of the two vessels under this test condition.

Table 4.2 Forces and moments on the Aframax and KVLCC2 from benchmark study

		Test A		Test B		Test C		Test D		Test E	
		Aframax	KVLCC2	Aframax	KVLCC2	Aframax	KVLCC2	Aframax	KVLCC2	Aframax	KVLCC2
	D	-0.77	-3.92	-0.37	-1.89	-0.77	-1.86	-0.17	-1.11	-0.60	-2.49
X	S_C	-1.10	-2.54	-1.22	-1.84	-0.65	-1.05	-0.43	-3.27	-1.66	-1.47
(N)	S_I	-1.32	-2.97	-1.39	-2.00	-	-	-	-	-1.66	-2.20
	S_A	*-0.93*	*-2.35*	*-1.08*	*-1.78*	*-0.58*	*-1.04*	*-0.35*	*-1.29*	*-1.49*	*-1.39*
	D	0.30	-0.85	1.55	-1.41	1.09	-0.86	0.81	-0.91	1.15	-0.85
Y	S_C	1.41	-1.12	1.23	-1.29	1.48	-1.20	0.81	-1.01	0.43	-0.32
(N)	S_I	1.51	-1.20	1.13	-1.42	-	-	-	-	0.48	-0.64
	S_A	*1.32*	*-0.84*	*1.46*	*-1.3*	*1.6*	*-1.14*	*0.76*	*-0.28*	*0.35*	*0.13*
	D	0.00	-	0.01	-	0.01	-	0.00	-	0.00	-
K	S_C	-0.29	0.31	-0.08	0.37	-0.04	0.28	0.66	0.07	-0.11	-0.02
(Nm)	S_I	-0.29	0.35	-0.06	0.40	-	-	-	-	-0.11	0.03
	S_A	*-0.28*	*0.29*	*-0.06*	*0.38*	*-0.01*	*0.28*	*-0.14*	*0.07*	*-0.12*	*0.06*
	D	-1.38	-3.44	-0.19	0.68	-0.73	0.00	-0.02	0.28	-0.11	0.74
N	S_C	-0.19	0.88	-0.09	0.80	-0.34	0.48	0.00	0.84	-1.05	-2.69
(Nm)	S_I	-0.57	1.33	-0.21	1.19	-	-	-	-	-1.10	-2.06
	S_A	*-0.24*	*0.80*	*-0.35*	*0.84*	*-0.45*	*0.33*	*-0.02*	*0.25*	*-0.9*	*-2.84*

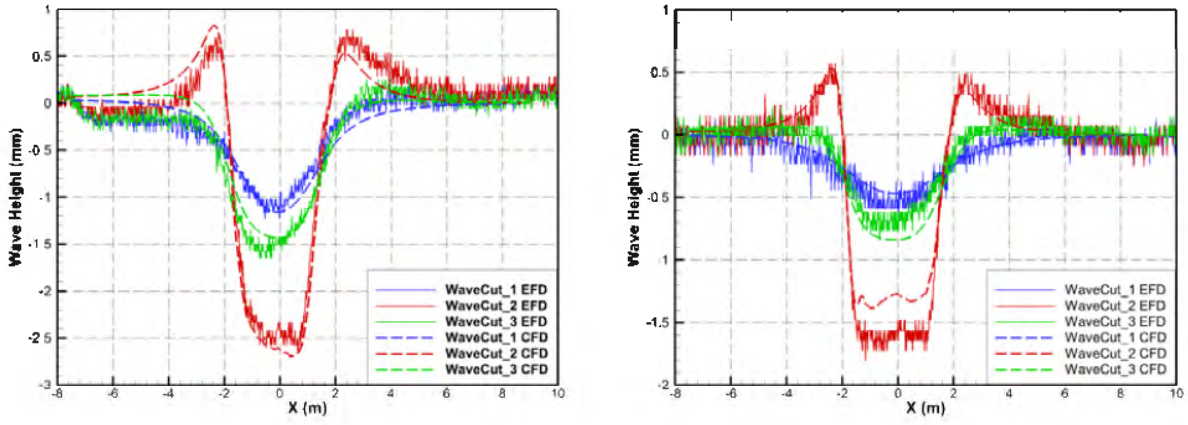

(a) (b)

Figure 4.3 Comparison of wave elevations for benchmark testing cases: (a) Test B; (b) Test D

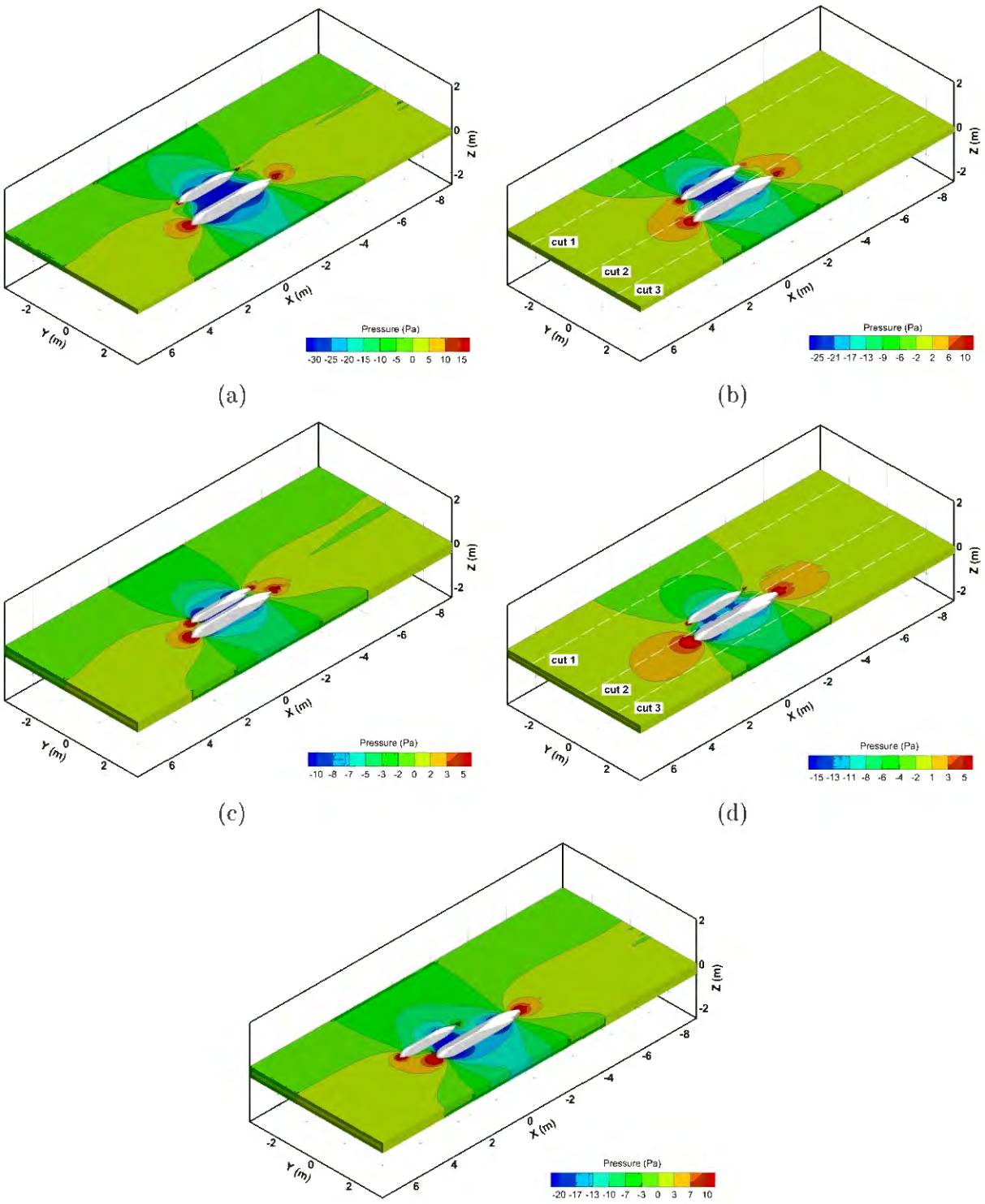

Figure 4.4 CFD pressure contours at the horizontal plane z=0 for benchmark cases: (a) Test A; (b) Test B; (c) Test C; (d) Test D; (e) Test E

4.3 Systematic computations

In the previous section, CFD computations on ship-ship interactions have been conducted for benchmark model test cases. The results demonstrate the feasibility of the present numerical model in predicting the hydrodynamic interaction forces and moments. Applying a similar numerical approach, the hydrodynamic interactions of the FLNG-LNG offloading configuration have been investigated for different relative longitudinal and lateral ship positions. An illustration of the testing matrix is shown in Table 4.3. It is worth mentioning that both of the model and full scale simulations are conducted in a fresh water condition to quantify the influence of Reynolds number due to the variation of ship speed and length. During the systematic computations, the position of the FLNG is always fixed and its gravitational centre is regarded as a reference point. The different relative longitudinal and lateral separations (Δx and Δy) are achieved by translating the position of LNG. The tested conditions contain nine Δx positions and six Δy positions which are non-dimensionalised by Lpp of the LNG tanker. The variations of the relative longitudinal separation Δx are coupled with a fixed lateral separation Δy=0.033×Lpp(LNG). A negative Δx represents a position when the CoG of the LNG is behind that of the FLNG. Similarly, the six relative lateral separations are studied with a fixed longitudinal separation Δx=0×Lpp(LNG) where the CoGs of the FLNG and LNG are aligned with each other in the longitudinal direction.

Table 4.3 Matrix of the CFD computations for FLNG-LNG interaction

Condition	Model scale		Full scale	
	FLNG	LNG	FLNG	LNG
h (m)	2.5	2.5	250	250
T (m)	0.24	0.1	24	10
T/h	0.096	0.04	0.096	0.04
U (m/s)	0.2	0.2	2	2
β (°)	0	0	0	0
Fr	0.032	0.037	0.032	0.037
Re	7.97×10^5	5.97×10^5	7.97×10^6	5.97×10^6
Δx	(-1.0, -0.75, -0.5, -0.25, 0.0, 0.25, 0.5, 0.75, 1.0) × L_{pp}(LNG)			
Δy	(0.033, 0.050, 0.083, 0.13, 0.25, 0.33) × L_{pp}(LNG)			

4.3.1 Numerical uncertainty analysis

Before investigating the differences between model scale and full scale computations, it is essential to quantify the numerical uncertainties in the simulation results. In order to

demonstrate the existence of scale effects, variations between model scale and full scale forces and moments have to be greater than the obtained numerical uncertainties. Following the verification procedures by Wilson et al. (2001) and Stern et al. (2001), it is assumed that the numerical uncertainty U_{SN} comprises of iterative convergence uncertainty U_I, grid-spacing uncertainty U_G and time-step uncertainty U_T, giving the following expression:

$$U_{SN}^2 = U_I^2 + U_G^2 + U_T^2 \tag{3.1}$$

Here, both U_I and U_T are considered to be negligible for steady RANS simulations. The grid-spacing uncertainty U_G is regarded to be the major contribution of U_{SN} and is of particular interest. The grid convergence study is performed for the condition $\Delta x=0.0\times L_{pp}$(LNG), $\Delta y=0.033\times L_{pp}$(LNG) using three different mesh configurations with a refinement ratio, $r_G=\sqrt{2}$. The number of elements for each mesh configuration is given in Table 4.4.

Table 4.4 Number of elements for studied mesh configurations in the grid convergence study

Mesh condition	Number of elements	
	Model scale	Full scale
Fine (1)	27,297,704	36,009473
Medium (2)	10,985,869	13,771,491
Coarse (3)	3,664,353	4,857,725

The simulation results for each mesh condition are listed in Table 4.5 and Table 4.6 along with estimations for grid-spacing uncertainties. It is observed that the uncertainties in surge and sway forces are much less than that in the roll and yaw moment predictions. Overall, the present computational method gives reasonably small numerical uncertainties, demonstrating its feasibility for undertaking further systematic simulations.

Table 4.5 Grid convergence study results for model scale simulations

Parameter	r_G	Solutions			R_G	Convergence	δ^*_G (%S_1)	U_G (%S_1)
		S_1	S_2	S_3				
X_{LNG}	$\sqrt{2}$	-0.160	-0.158	-0.155	0.67	MC	-2.50	3.54
Y_{LNG}	$\sqrt{2}$	0.208	0.207	0.205	0.50	MC	-0.48	0.53
K_{LNG}	$\sqrt{2}$	-0.0344	-0.0345	-0.0392	0.02	MC	~	7.00
N_{LNG}	$\sqrt{2}$	0.0162	0.0163	0.0149	-0.07	OC	~	4.32
X_{FLNG}	$\sqrt{2}$	-0.502	-0.501	-0.504	-0.33	OC	~	0.30
Y_{FLNG}	$\sqrt{2}$	-0.202	-0.199	-0.206	-0.43	OC	~	1.73
K_{FLNG}	$\sqrt{2}$	0.0081	0.0077	0.0099	-0.18	OC	~	13.7
N_{FLNG}	$\sqrt{2}$	0.0562	0.0520	0.0631	-0.38	OC	~	9.88

Table 4.6 Grid convergence study results for full scale simulations

Parameter	r_G	Solutions			R_G	Convergence	δ^*_G (%S_1)	U_G (%S_1)
		S_1	S_2	S_3				
X_{LNG}	$\sqrt{2}$	-30060	-29061	-30707	-0.61	OC	~	2.74
Y_{LNG}	$\sqrt{2}$	233545	224071	235983	-0.80	OC	~	2.55
K_{LNG}	$\sqrt{2}$	-3586507	-3378479	-3866796	-0.43	OC	~	6.81
N_{LNG}	$\sqrt{2}$	1582736	1599956	1643485	0.40	MC	0.71	4.54
X_{FLNG}	$\sqrt{2}$	-196083	-197206	-202186	0.23	MC	0.10	2.66
Y_{FLNG}	$\sqrt{2}$	-206203	-207109	-204392	-0.33	OC	~	0.66
K_{FLNG}	$\sqrt{2}$	778733	733683	959874	-0.20	OC	~	14.5
N_{FLNG}	$\sqrt{2}$	204043	198270	250983	-0.11	OC	~	12.90

4.3.2 Computational results

Numerical predictions on the interaction forces and moments for the FLNG-LNG offloading system are non-dimensionalised using Equations (3.2) to (3.5). The computed model and full scale results are presented in Figure 4.5 and Figure 4.6. Qualitative analysis on the differences between the model and full scale computations are reported in Section 4.3.5.

$$X' = \frac{X}{0.5\,\rho\,U_0^2\,T\,L_{pp}} \tag{3.2}$$

$$Y' = \frac{Y}{0.5\,\rho\,U_0^2\,T\,L_{pp}} \tag{3.3}$$

$$K' = \frac{K}{0.5\,\rho\,U_0^2\,T\,L_{pp}^2} \tag{3.4}$$

$$N' = \frac{N}{0.5\,\rho\,U_0^2\,T\,L_{pp}^2} \tag{3.5}$$

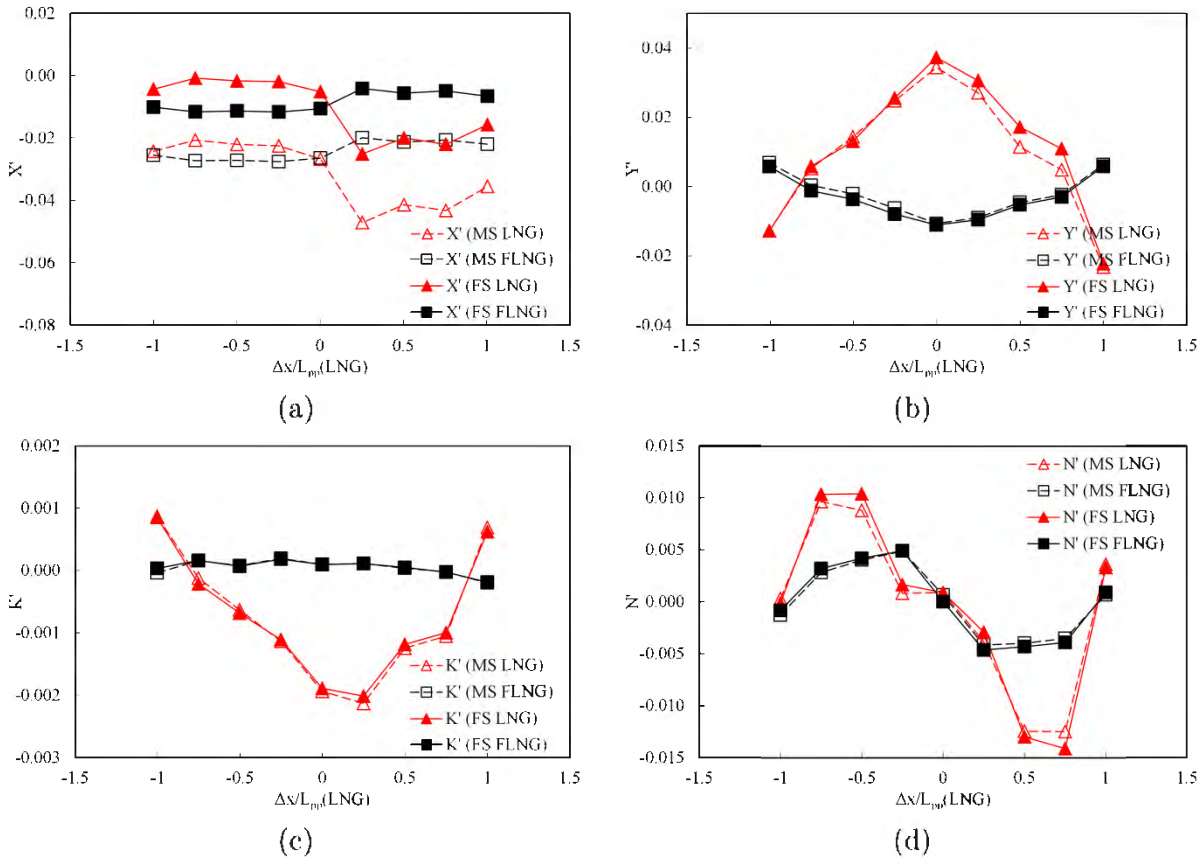

Figure 4.5 Non-dimensional interaction forces and moments from model and full scale computations for varying Δx, $\Delta y=0.033L_{pp}(LNG)$, $Fr=0.037$ based on $L_{pp}(LNG)$, $T(LNG)/h=0.04$ (a) Surge force; (b) Sway force; (c) Roll moment; (d) Yaw moment

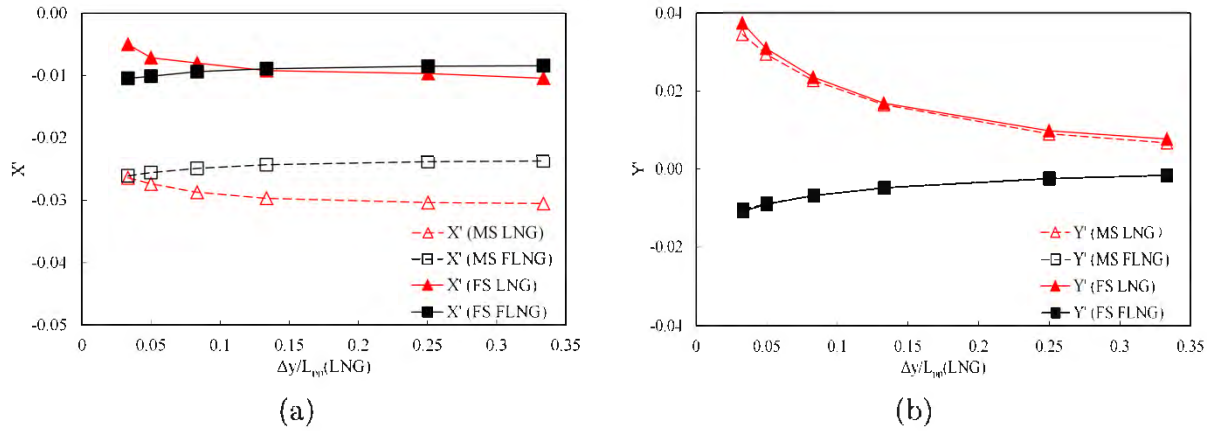

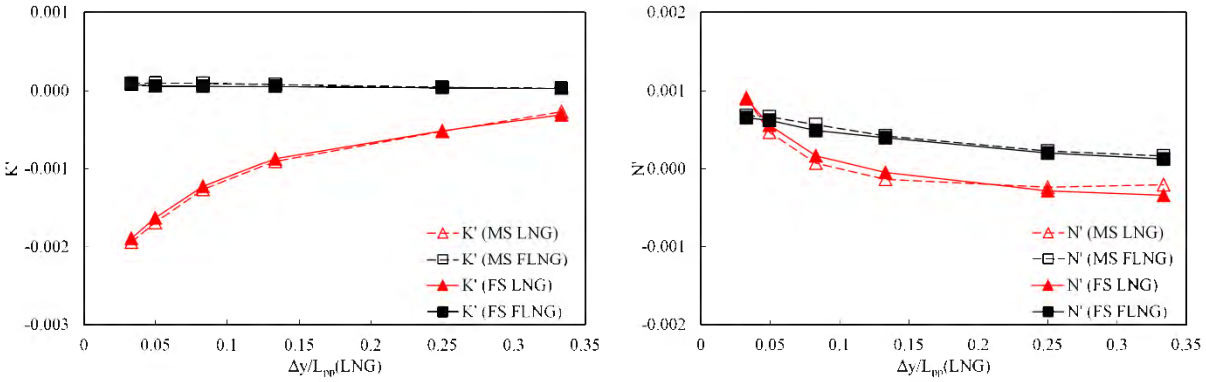

(c) (d)

Figure 4.6 Non-dimensional interaction forces and moments from model and full scale computations for varying Δy, Δx=0.0L_{pp}(LNG), Fr=0.037 based on L_{pp}(LNG), T(LNG)/h=0.04 (a) Surge force; (b) Sway force; (c) Roll moment; (d) Yaw moment

4.3.3 FLNG-LNG interaction in model scale

Influence of the longitudinal distance Δx

The hydrodynamic forces and moments on the FLNG and LNG for different relative longitudinal distances Δx are shown in Figure 4.5. The relative lateral distance is set to be fixed at Δy/L_{pp}(LNG)=0.033 for all the tested cases here. It can be seen in Figure 4.5(a), when the CoG of the LNG is behind that of the FLNG, Δx/L_{pp}(LNG)<0.0, the non-dimensional surge force X′ on the LNG is relatively small and shows minor variation in magnitude against change in Δx positions. As the CoG of the LNG moves towards the front of the FLNG, X′ on the LNG increases and reaches its maximum at Δx/L_{pp}(LNG) =0.25 and then drops gradually. The non-dimensional surge force X′ on the FLNG exhibits an opposite trend. The maximum value on the FLNG occurs when the CoG of the LNG is behind that of the FLNG and it stays relatively consistent before the LNG moves to the front of the FLNG. At the position Δx/L_{pp}(LNG) =0.25, X′ on the FLNG reaches its minimal value in magnitude and then increases slowly afterwards. The distribution of X′ on the LNG and FLNG is close to symmetrical around the value of approximately -0.27.

A similar pattern can be found for the non-dimensional sway force Y′ in Figure 4.5(b) where the predicted Y′ values on the FLNG and LNG are symmetric about 0. The FLNG mostly encountered negative sway forces for the studied cases, indicating the hull has been attracted towards the LNG. On the other hand, the LNG mostly experiences positive sway force during the variation of Δx, showing it tends to move towards the FLNG as well. The exceptions are observed at the condition Δx/L_{pp}(LNG)=-1.0 and 1.0 where the two vessels are repelled from each other. The sway force increases when the CoGs of the two vessels are getting close. It

reaches a peak at $\Delta x/L_{pp}(LNG)=0$ and decreases after that when the two CoGs move away from each other.

The measured non-dimensional roll moment K′ on the FLNG and LNG are not as significant as the sway force Y′ in magnitude as shown in Figure 4.5(c). Again, for most cases where $\Delta x/L_{pp}(LNG)$ is from -0.75 to 0.75, the FLNG experiences positive roll moment and the LNG encountered negative roll moment, indicating that the decks of the two vessels are rolling towards each other. Regarding the non-dimensional yaw moment N′ in Figure 4.5(d), predictions on the two vessels present similar tendency along Δx. When the LNG is at the furthest distance from the FLNG, $\Delta x/L_{pp}(LNG)=-1.0$, the N′ values are very small but found to be positive on the LNG and negative on the FLNG. For the conditions where the CoG of the LNG is located closer to the FLNG, $\Delta x/L_{pp}(LNG)$ from -0.75 to 0.0, the yaw moment is shown to be positive on both hulls and are much larger in magnitude. This means the LNG is bow-in towards the FLNG while the FLNG is bow-away from the LNG. Results are opposite when the CoG of the LNG is located in front of that of the FLNG, the recorded yaw moment is negative on both hulls, indicating that the FLNG is bow-in towards the LNG while the LNG is bow-away from the FLNG. At last, when the LNG is at the furthest distance forward of the FLNG, the yaw moment on both hulls reduces to a negligible level.

To better understand the hydrodynamics of the interactions between the FLNG and LNG, especially for the sway force Y and yaw moment N, the axial velocity contours on the horizontal plane z=-0.05 m for different Δx are presented in Figure 4.7. The directions of Y and N on each hull are labelled as arrows. The development of the flow field and hydrodynamic interactions between the two ships has been demonstrated for varying Δx positions. In general, it is observed that high velocity regions exist around the fore- and aft-shoulder of the two ship hulls due to the nature of their physical shape. When the CoG of the LNG is at a closer position to that of the FLNG CoG, another high velocity region is created in the area between the two vessels, resulting from the blockage by the narrow gap between the two hulls.

To further illustrate the FLNG-LNG interaction, pressure distributions on the port side of the LNG and on the starboard side of the FLNG are given in Figure 4.8. It can be seen that low pressure zones exist around the fore- and aft- shoulder on both hulls, which are induced by high velocity flows in the vicinity of these areas as mentioned previously. When the CoG of the LNG has been moved towards that of the FLNG, another low pressure region is created on both hulls and its size grows as the blockage effect by the narrow gap between the two vessels gets more pronounced. Note that, with the change of Δx from -1.0 to 1.0, this low pressure zone moves backwards from bow to stern on the LNG, while forwards from stern to bow on the FLNG.

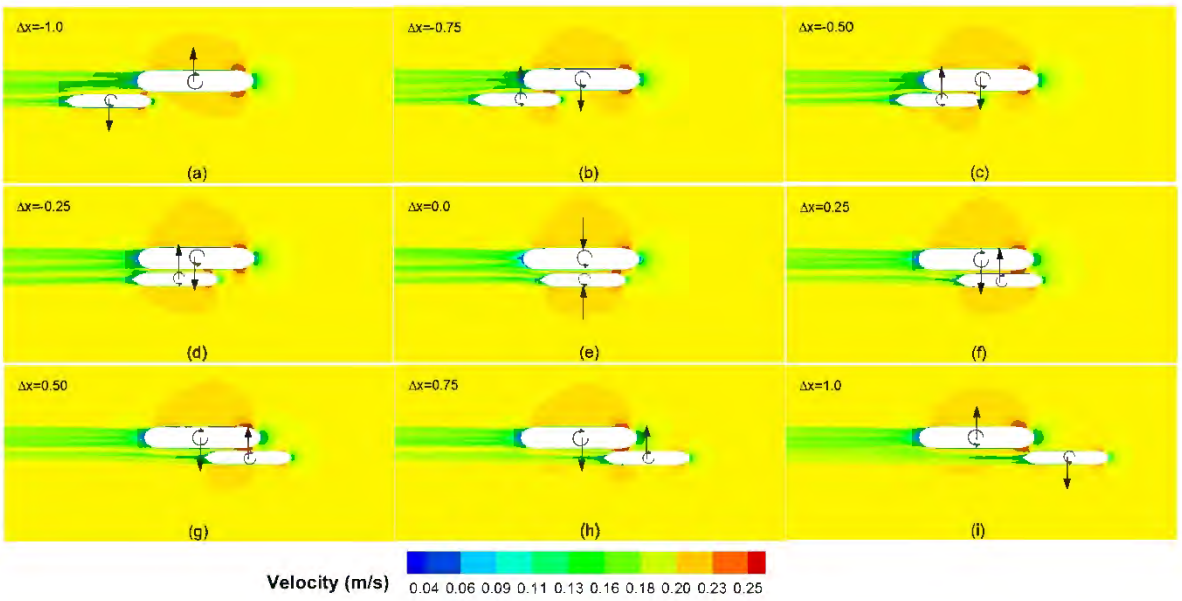

Figure 4.7 Axial velocity contours at the horizontal plane z=-0.05m for different Δx in model scale, Δy=0.033L_{pp}(LNG), Fr=0.037 based on L_{pp}(LNG), T(LNG)/h=0.04

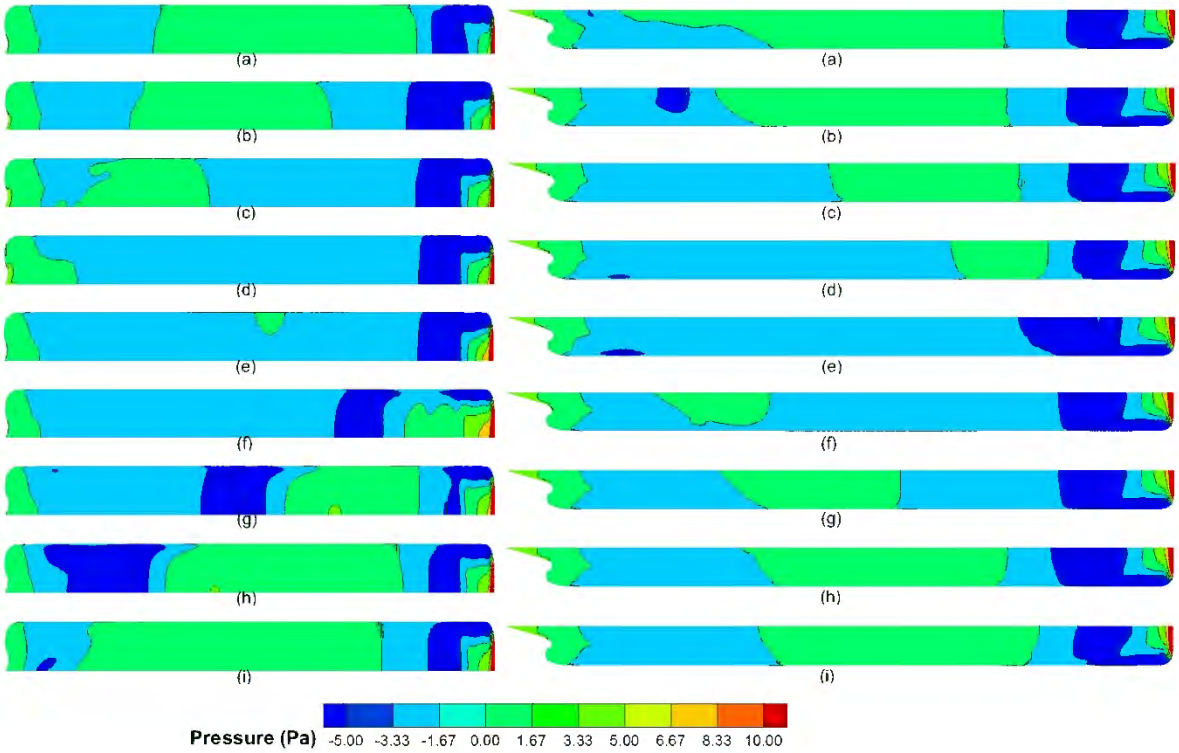

Figure 4.8 Pressure distributions on the port side of the LNG (left, vertical scale magnified three times) and on the starboard side of the FLNG (right) for different Δx in model scale, Δy=0.033L_{pp}(LNG), Fr=0.037 based on L_{pp}(LNG), T(LNG)/h=0.04 (a) Δx=-1.0L_{pp}(LNG), (b) Δx=-0.75L_{pp}(LNG), (c) Δx=-0.50L_{pp}(LNG), (d) Δx=-0.25L_{pp}(LNG), (e) Δx=0.0L_{pp}(LNG), (f) Δx=0.25L_{pp}(LNG), (g) Δx=0.50L_{pp}(LNG), (h) Δx=0.75L_{pp}(LNG) and (i) Δx=1.0L_{pp}(LNG).

Influence of the lateral distance Δy

Variations of the hydrodynamic forces and moments on the model scale FLNG and LNG against different lateral separations Δy at fixed longitudinal position Δx=0 are presented in Figure 4.6. It is seen from Figure 4.6(a) that the non-dimensional surge force X′ has not been influenced by the lateral distance between the two vessels significantly. For the non-dimensional sway force Y′, roll moment K′ and yaw moment N′, strong dependence on Δy has been demonstrated in Figure 4.6(b), (c) and (d). As the lateral distance between the two ships increases, blockage effect in the narrow gap between the two hulls becomes less significant which leads to reductions in the magnitude of predicted Y′, K′ and N′ values.

The axial velocity contours on the horizontal plane z=-0.05m and pressure distributions on the FLNG and LNG hulls for different Δy are presented in Figure 4.9 and Figure 4.10. For the condition Δy=0.033 where the two hulls are at the closest proximity, strong hydrodynamic interaction between the two vessels is evident. It is seen that the wake fields after the ship hulls tend to combine together, which yields a large wake flow behind the two vessels. In addition, large low pressure regions are found distributing along the port side of the LNG and the starboard side of the FLNG. As the relative lateral separation Δy increases, the size of these low pressure regions has been reduced. For the condition Δy=0.33 where the two vessels are at the greatest distance from each other, the low pressure regions around the mid-ship of the LNG and FLNG vanished, which reveals a significant reduction in hydrodynamic interaction between the two ships.

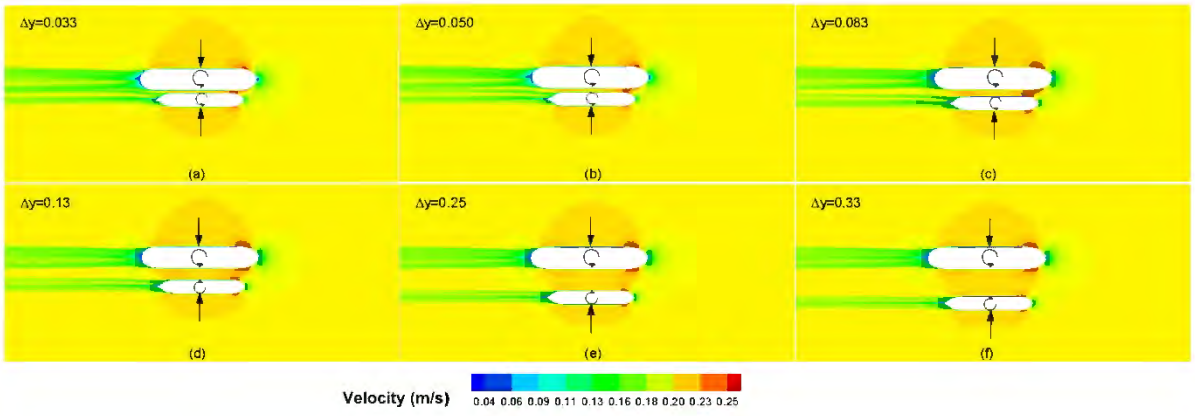

Figure 4.9 Axial velocity contours at the horizontal plane z=-0.05 m for different Δy in model scale, $\Delta x=0.0L_{pp}$(LNG), Fr=0.037 based on L_{pp}(LNG), T(LNG)/h=0.04

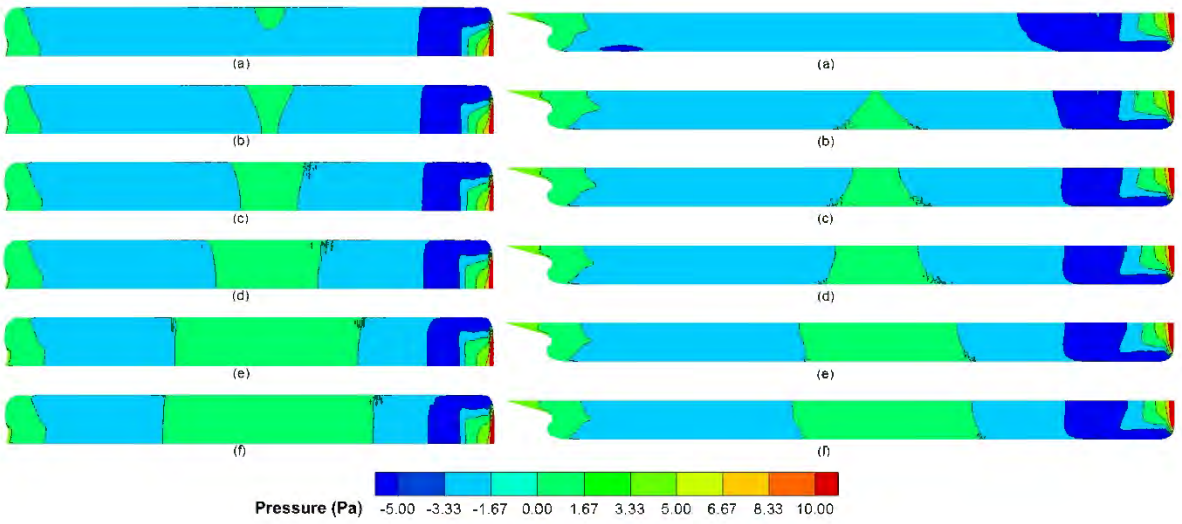

Figure 4.10 Pressure distributions on the port side of the LNG (left, vertical scale magnified three times) and on the starboard side of the FLNG (right) for different Δy in model scale, $\Delta x=0.0L_{pp}(LNG)$, Fr=0.037 based on $L_{pp}(LNG)$, $T(LNG)/h=0.04$ (a) $\Delta y=0.033L_{pp}(LNG)$, (b) $\Delta y=0.050L_{pp}(LNG)$, (c) $\Delta y=0.083L_{pp}(LNG)$, (d) $\Delta y=0.13L_{pp}(LNG)$, (e) $\Delta y=0.25L_{pp}(LNG)$ and (f) $\Delta y=0.33L_{pp}(LNG)$

4.3.4 Full scale predictions on FLNG-LNG interaction

In a real situation, the hydrodynamics involved in a full scale ship-ship interaction problem can be very different from that in the model testing. Therefore, full scale predictions of hydrodynamic forces and moments on the FLNG and LNG for varying positional configurations are conducted and discussed in this section based on the validated computational setup.

Variations of the full scale non-dimensional surge force X′, sway force Y′, roll moment K′ and yaw moment N′ on the two ships against different longitudinal seperations Δx are presented in Figure 4.5. It is found that, when the CoG of the LNG is behind that of the FLNG, $\Delta x/L_{pp}(LNG)<0.0$, the non-dimensional surge force X′ on the two ships shows minor variation in magnitude against change in Δx positions. As the CoG of the LNG moves to the front of that of the FLNG, X′ on the LNG grows to become larger than that on the FLNG and reaches its maximum at $\Delta x/L_{pp}(LNG)$ =0.25 and then drops gradually. The surge force X′ on the FLNG exhibits an opposite behaviour. In general, the qualitative trend of the full scale X′ correlates well with model scale predictions. Similarly, it is seen in Figure 4.5(b), (c) and (d) that the tendencies of full scale predictions on Y′, K′ and N′ all correlate well with model scale results. The differences in the magnitude of these values will be presented and elaborated in the next section.

The correlation in the tendency of force and moment results against different Δx can be explained by the similarities observed from the model and full scale flow fields and pressure distributions around the two ships by comparing Figure 4.7 and Figure 4.9 with Figure 4.11 and Figure 4.13. In Figure 4.11, the full scale axial velocity contours at the horizontal plane z=-5.0m for different Δx are presented. It is seen that the velocity fields on the plane share identical patterns as they are captured in model scale. The same is found for the pressure distributions on the FLNG and LNG hulls when comparing Figure 4.12 against Figure 4.8. On the FLNG, the low pressure peak moves forwards from stern to bow, while on the LNG it moves backwards from bow to stern with an increase of Δx.

From a practical point of view, the predictions on the FLNG-LNG interaction forces and moments can provide recommendations and guidelines for real world manoeuvring operations. For instance, if the LNG offloading was chosen to be carried out at the configuration $\Delta x/L_{pp}(LNG)=0.0$ for minimal yaw moment, additional care should be taken on reducing the possible threats of collision resulting from the large sway force that pulls the two vessels towards each other. The solution could be introducing external sway forces from thrusters or having a robust fender system along the starboard side of the FLNG. Adversely, if the offloading was chosen to be taken place at $\Delta x/L_{pp}(LNG)=-0.75$ for minimal sway forces, attention should be paid on the relatively large yaw moment experienced on the two vessels to avoid possible threats of collision between the bow of the LNG and stern of the FLNG.

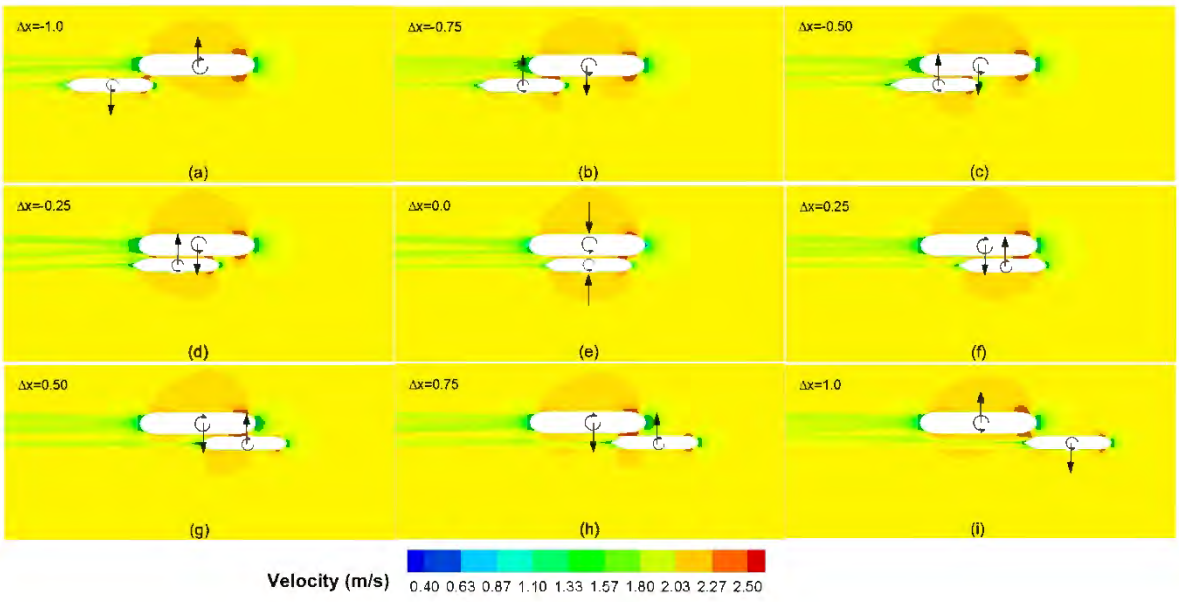

Figure 4.11 Axial velocity contours at the horizontal plane z=-5m for different Δx in full scale, $\Delta y=0.033L_{pp}(LNG)$, Fr=0.037 based on $L_{pp}(LNG)$, T(LNG)/h=0.04

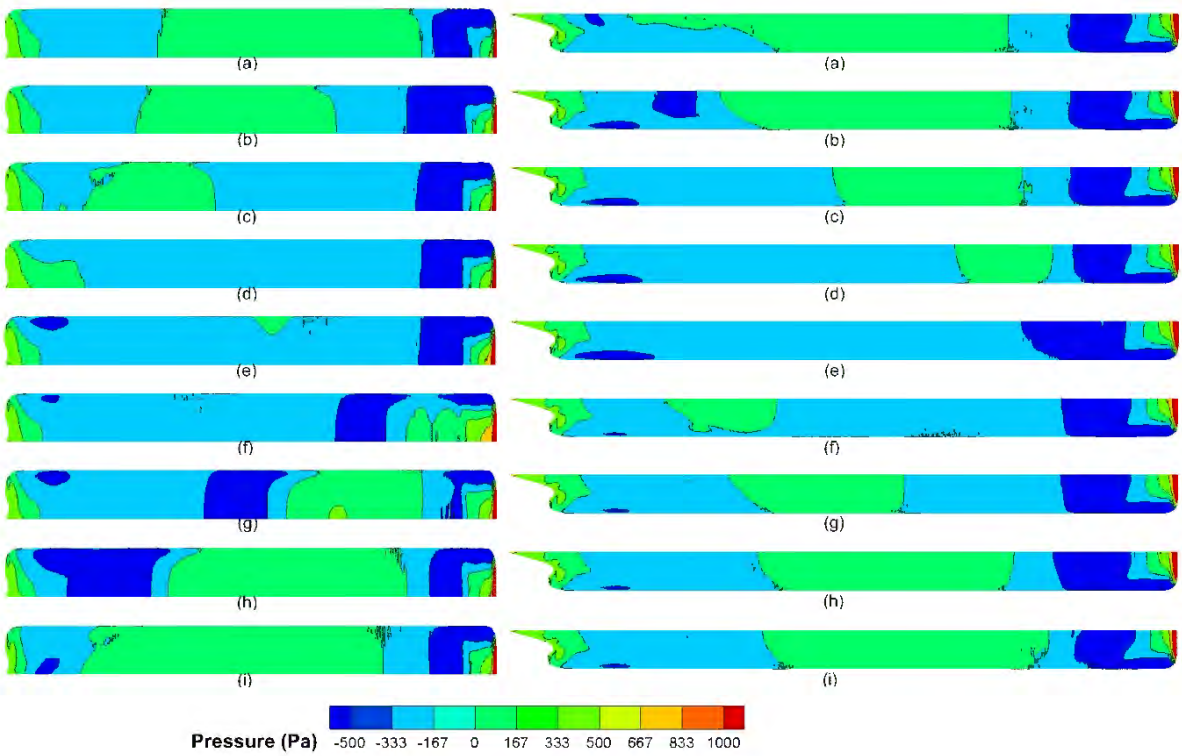

Figure 4.12 Pressure distributions on the port side of the LNG (left, vertical scale magnified three times) and on the starboard side of the FLNG (right) for different Δx in full scale, Δy=0.033L_{pp}(LNG), Fr=0.037 based on L_{pp}(LNG), T(LNG)/h=0.04 (a) Δx=-1.0L_{pp}(LNG), (b) Δx=-0.75L_{pp}(LNG), (c) Δx=-0.50L_{pp}(LNG), (d) Δx=-0.25L_{pp}(LNG), (e) Δx=0.0L_{pp}(LNG), (f) Δx=0.25L_{pp}(LNG), (g) Δx=0.50L_{pp}(LNG), (h) Δx=0.75L_{pp}(LNG) and (i) Δx=1.0L_{pp}(LNG).

For the variation of lateral separation Δy, full scale predictions of X′, Y′, K′ and N′ on the LNG and FLNG are shown in Figure 4.6. When comparing these results against model scale, it is observed the tendencies of full scale predictions on X′, Y′, K′ and N′ all correlate well with model scale data. To elaborate the credibility of this finding, full scale axial velocity contours and pressure distributions around the LNG and FLNG for different Δy are presented in Figure 4.13 and Figure 4.14. Again, it is seen that the increase of lateral distance between the two vessels leads to a reduction in the hydrodynamic interaction. Therefore, in a real world offloading operation, it is suggested that the FLNG and LNG should be separated from each other as far as possible to reduce the influences of hydrodynamic interactions. However, operational factors such as the length of the cryogenic hose and mooring system should also be considered to when determining the desired lateral separation.

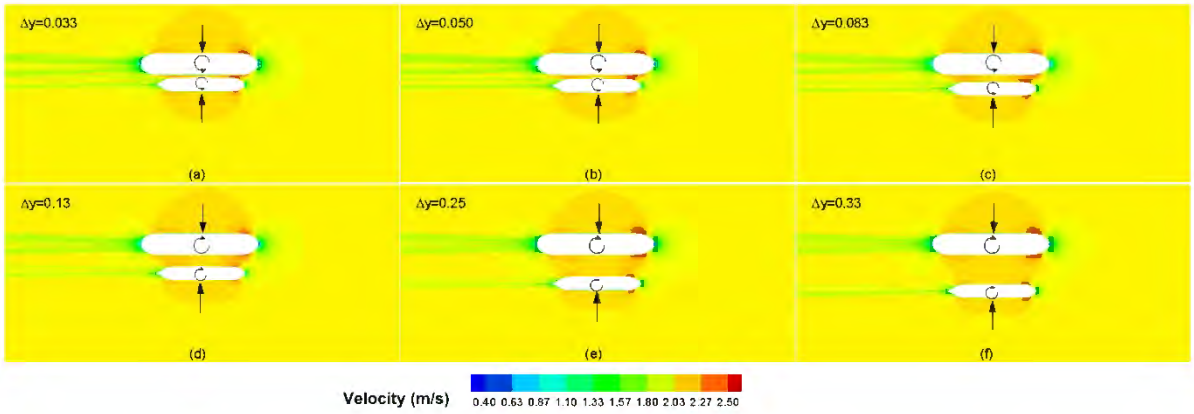

Figure 4.13 Axial velocity contours at the horizontal plane z=-5m for different Δy in full scale, $\Delta x=0L_{pp}(LNG)$, Fr=0.037 based on $L_{pp}(LNG)$, T(LNG)/h=0.04

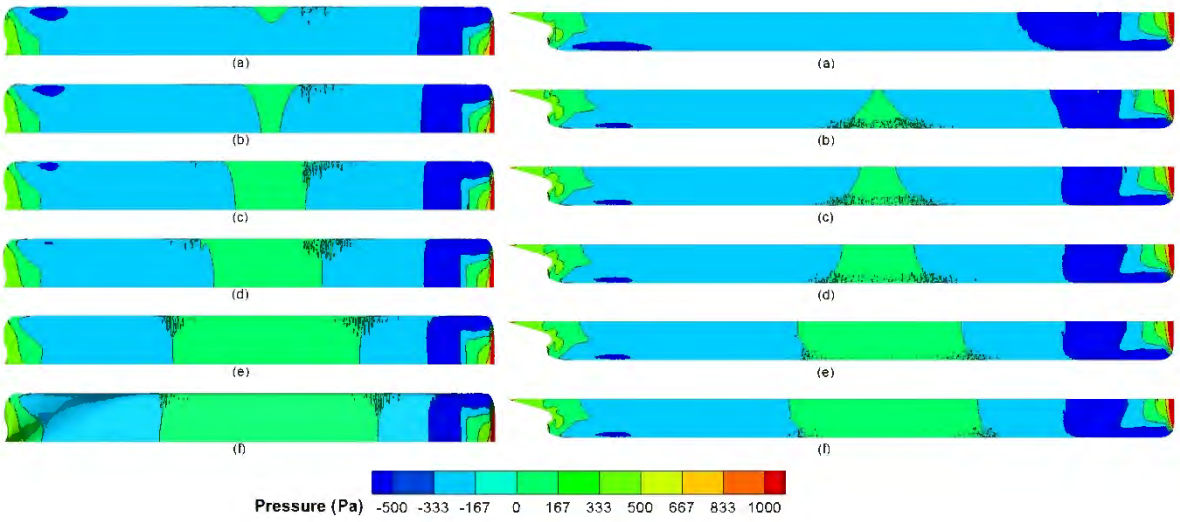

Figure 4.14 Pressure distributions on the port side of the LNG (left, vertical scale magnified three times) and on the starboard side of the FLNG (right) for varies Δy in full scale, $\Delta x=0L_{pp}(LNG)$, Fr=0.037 based on $L_{pp}(LNG)$, T(LNG)/h=0.04 (a) $\Delta y=0.033L_{pp}(LNG)$, (b) $\Delta y=0.050L_{pp}(LNG)$, (c) $\Delta y=0.083L_{pp}(LNG)$, (d) $\Delta y=0.13L_{pp}(LNG)$, (e) $\Delta y=0.25L_{pp}(LNG)$ and (f) $\Delta y=0.33L_{pp}(LNG)$

4.3.5 Scale effects in FLNG-LNG interaction

Analysis on the differences between non-dimensional model and full scale simulation results shown in Figure 4.5 and Figure 4.6 is presented in the section. For the non-dimensional surge force X′, significant differences are found between the model and full scale results, demonstrating strong influences of scale effects. The magnitude of full scale predictions for X′ is shown to be much less than that of the model scale for both of the LNG and FLNG hulls. This can be explained by comparing the model scale and full scale axial velocity fields shown

in Figures 4.7, 4.9, 4.11 and 4.13. It is seen that the model scale simulations have relatively thicker boundary layers and larger turbulent wake regions after the hull and this indicates more significant viscous effects over the full scale conditions due to the lower Reynolds number at model scale. For the other non-dimensional parameters, Y′, K′ and N′, scale effects seem to be much less influential on the predictions since the model scale and full scale numerical results correlate well. This is also reflected from the similarities of model and full scale pressure distributions on the ship hulls as presented in Figures 4.8, 4.10, 4.12 and 4.13.

To further investigate the influence of scale effects, the average percentage variations of predicted force and moment results are compared with numerical uncertainties for the tested cases as given in Table 4.7. It is found that the percentage variations of X′ between model and full scale computations are much greater than the numerical uncertainties, which is a clear evidence of scale effects. For the other parameters, the percentage variations are shown to be either close or less than the uncertainty values, which demonstrates scale effects are much less influential for these parameters.

Table 4.7 Quantitative summary of scale effects on FLNG-LNG interaction force and moment predictions

		Average variation% (S_{MS}-S_{FS})/S_{FS}		**Numerical uncertainty**
		For varying Δx	**For varying Δy**	**U_G(MS+FS)**
LNG	X′	72.2%	71.8%	6.28%
	Y′	7.69%	7.11%	3.08%
	K′	13.1%	4.77%	13.8%
	N′	10.9%	11.7%	8.86%
FLNG	X′	66.3%	62.8%	2.96%
	Y′	14.3%	1.90%	2.39%
	K′	13.0%	24.8%	28.2%
	N′	15.4%	10.8%	22.8%

4.4 Concluding remarks

The hydrodynamic interactions of the FLNG/LNG offloading system in calm water steady current has been investigated and reported in this chapter using CFD. Initially, a study of five benchmark test cases for the Aframax and KVLCC2 interaction is made. Forces and moments are compared with experimental data and computational results from literature. From the benchmark study, it is found that the predicted surface elevations correlate well with the model test measurements, indicating the pressure distributions at the free surface were well captured. Besides that, there is a good correspondence between the three sets of computational

results for the interaction forces and moments, implying that the current computations are validated by other CFD solutions. However, the discrepancy between experimental measurements and results from the three sets of computations is relatively large in many cases. The same finding is reported in Zou and Larsson (2013)'s work. The reason for this can be the existence of relatively large numerical and experimental uncertainties for the presented benchmark cases. Here, the authors are unable to perform a formal verification and validation analysis due to the lack of experimental uncertainties.

On the validated numerical setup, systematic computations on the hydrodynamic interactions of the FLNG/LNG offloading system have been carried out for different longitudinal and lateral separations. The hydrodynamic forces and moments in variations are predicted, and to help understand these changes, the axial velocity contours and pressure distributions around the two hulls are presented. Furthermore, to quantify the scale effects existing in the current study, full scale predictions on the FLNG/LNG interactions are conducted and discussed.

With varying longitudinal separation, the surge force on the LNG increases when it is moved to the front of the FLNG; while for the FLNG, the tendency of surge force experiences the opposite trend. At large longitudinal separations, a repelling sway force exists and pushes the LNG and FLNG away from each other. As the separation reduces, the force direction is reversed and creates strong attraction between the two hulls. At the far longitudinal separations, a yaw moment turns the LNG and the FLNG away from each other. For the rest of the tested conditions, it forces the hulls to turn in the same direction. When the LNG is positioned behind the FLNG, the yaw moment turns the two ships to the port; while with the LNG CoG ahead of the FLNG CoG, it turns the hulls to the starboard. With varying lateral separation, the magnitude of forces and moments on the LNG and FLNG all reduces as the lateral separation increases. The sway force acting on the LNG and FLNG tends to pull them towards each other for the tested cases. At the closest lateral separation, the yaw moment turns the bow of the LNG and FLNG to port side. As the separation increases, this yaw moment diminishes and approaches zero.

When comparing the model scale and full scale simulation results, the following conclusions can be drawn:

- Tendencies of non-dimensional model and full scale interaction force and moment predictions for the LNG and FLNG hulls correlate well.
- Model scale simulations demonstrate relatively thicker boundary layers and larger turbulent wake regions around the LNG and FLNG hulls, indicating a more significant viscous effect over the full scale conditions. As a result, large discrepancies exist

between the predictions of model scale and full scale surge force magnitude, which illustrate that scale effects are evident.

- Scale effects are much less influential in sway force, roll moment and yaw moment predictions due to very good correspondence found between the patterns of model and full scale pressure distributions on the port side of the LNG and starboard side of FLNG hulls.

Chapter 5 has been removed for copyright or proprietary reasons.

The chapter contains material published in:
Jin, Y., Chai, S., Duffy, J ., Chin, C., & Bose, . -. (2016). Experimental Study of Wave Induced Loads and :ti.lotions on FLNG in Head and Oblique Sea Waves. Paper presented at the ASME 2016 35th International Conference on Ocean, Offshore and Arctic Engineering.

Jin, Y., Chai, S., Duffy, J ., Chin, C., Bose, K., & Sun, L. (2016). URANS Prediction of Ship Hydrodynamics in Head Sea Waves at Zero Forward Speed with Model Testing Validation.
Paper presented at the AS:ti.IE 2016 35th International Conference on Ocean, Offshore and Arctic Engineering.

Jin, Y., Chai, S., Duffy, J ., Chin, C., & Bose, N (2017). URANS predictions of wave induced loads and motions on ships in regular head and oblique waves at zero forward speed. Journal of Fluids and Structures 74, 178-204.

Chapter 6 - FLNG-LNG Interaction in Regular Waves

In this chapter, URANS computations are presented for investigating the hydrodynamic interactions between a conceptual FLNG and a LNG vessel in a side-by-side offloading configuration. The study is carried out in regular head sea waves with both vessels' motion being fixed in 6 DOF. Physical model scale experiments are performed for the validation of the numerical approach. Based on the validated numerical model, a series of systematic computations is reported for studying the wave loads and gap wave responses of the FLNG-LNG system for different wave frequencies and lateral separations. Furthermore, the computations are also performed in full scale to quantify possible scale effects in the prediction of wave loads and gap wave responses.

6.1 Computational domain, boundary conditions and grid

The computational domain is designed following the International Towing Tank Conference (ITTC) practical guidelines for ship CFD applications (ITTC, 2011) to avoid blockage effect and wave reflections. A schematic drawing of the computed fluid domain is given in Figure 6.1. A velocity inlet boundary condition is applied at the upstream end of the fluid domain where incident regular waves are generated. At the downstream end of the fluid domain, a damping pressure outlet boundary is imposed to prevent wave reflections. The top, bottom and side walls of the domain are all selected as velocity inlets to avoid velocity gradient occurring from the boundaries as in the use of a slip-wall condition.

The computational grid is generated according to the CD-Adapco (2014) recommendations of wave simulations. Slow cell growth rate is selected to create smooth mesh transition between the refined hull surfaces and the outer boundaries. Hexahedral trimmer and surface remesher are adopted to generate global volume mesh as well as local refinements. To resolve the turbulent boundary layer, all y+ wall treatment is utilised as well as the prism layer mesh, achieving y+ value of 30+ along the hull for all computations. At the free surface, anisotropic trimmer refinements in both X and Z directions are applied, which provides approximately 80 cells per wavelength and 20 cells per wave height for accurate wave capturing.

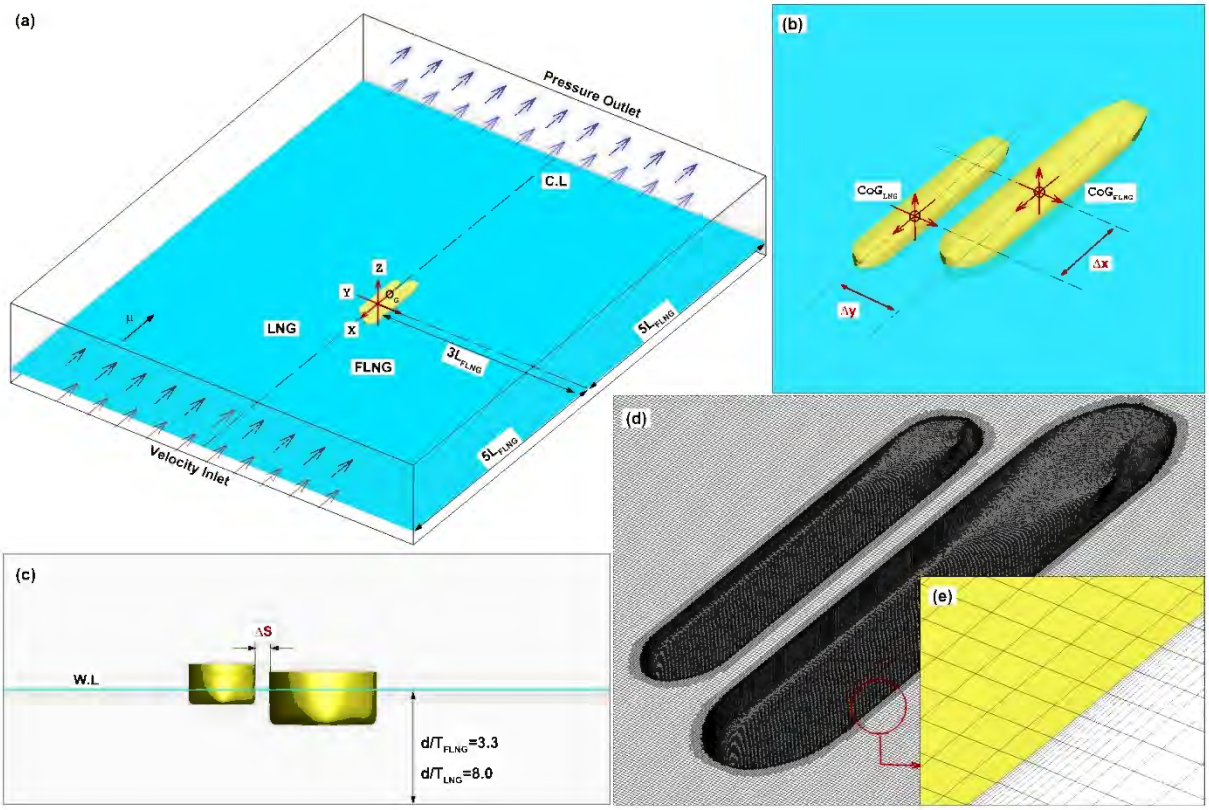

Figure 6.1 Illustration of the coordinate system and dimensions of the computational domain and mesh grid

6.2 Wave generation

The fifth order Stokes waves are employed for the present computations as it resembles real waves more closely than ones generated by the method using the first order wave theory. This higher order wave theory is based on the work by Fenton (1985) and is suggested by DNV (2010) for wave generations in this study. Existing work by Tezdogan et al. (2015) and Jin et al. (2016) both applied this approach to generate regular waves. Their results showed a 2.5% difference when compared against input wave height. A detailed comparison between the computed waves and theoretical values can be found in Section 5.2. Illustrations of the generated waves at different positions along the computational domain are given in Figure 6.2.

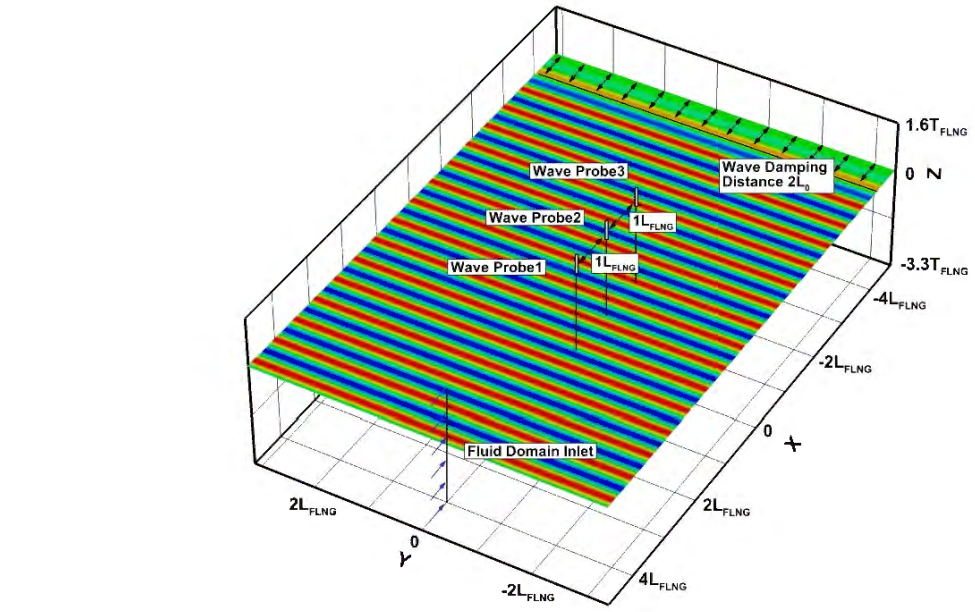

(a)

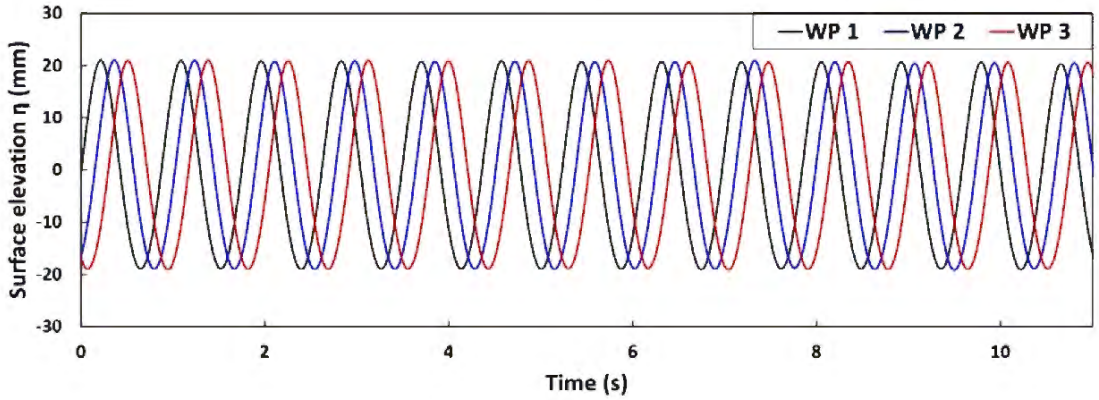

(b)

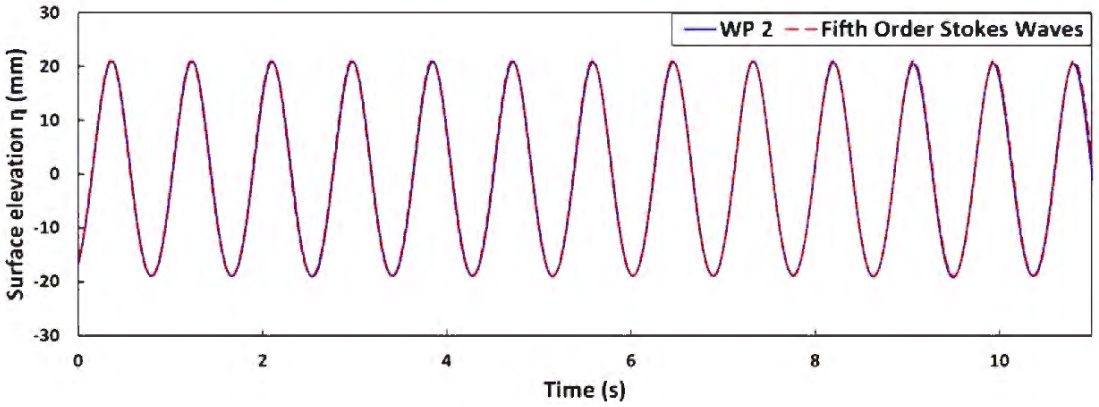

(c)

Figure 6.2 Demonstration of wave generation in the numerical tank f=1.15 Hz (a) locations of wave probes, vertical direction not to scale (b) comparisons between wave probe measurements (c) comparison between URANS prediction and theoretical wave generation

6.3 Experimental results

Model scale measurements of wave loads acting on the FLNG-LNG system are presented in this section. The two ships were constrained in 6 degrees of freedom (DOF). Gap wave elevations η were measured through wave probes. The experimental results are employed for the validation of numerical simulations. The water depth set for the tests in this study was 0.8 m, which corresponds to the water depth draft ratio of d/T_{FLNG}=3.3 or d/T_{LNG}=8.0. The two ships were parallel to each other and the investigated gap width was 100mm. Regular waves were generated by a multi-element wavemaker with 16 paddles. The model tests were carried out at the scale of 1:100 for both the FLNG and LNG model. The tested cases are listed in Table 6.1.

Table 6.1 Matrix of model test cases

	DOF	Wave angle μ	Wave frequency (Hz)	Wave height H (mm)	Lateral separation ΔS (mm)
FLNG LNG	Fixed in 6DoF	180° (head sea)	0.63 0.70 0.75 0.81 0.89 0.99 1.06 1.15	40	100

The wave induced forces and moments and the gap wave elevations were measured when the waves are passing through the FLNG-LNG system. An example of the time history measurements of wave loads are given in Figure 6.3 for the condition of 0.63 Hz head sea waves. It can be observed that the wave loads on the LNG are less comparable to that on the FLNG, which is primarily due to its smaller displacement. The wave load frequencies on both vessels are consistent as can be found from performing Fast Fourier Transformation (FFT) on the time history signals. Figure 6.4 presents some wave load signals on the frequency domain from the FFT analysis.

The gap wave elevations exhibit similar sinusoidal nature as the measured wave loads. Time history measurements from wave probes are presented in Figure 6.5. It is observed that the amplitude of the gap waves varies at different locations. The gap wave frequency remains consistent with the incoming wave frequency as presented in Figure 6.6 based on FFT analysis. More detailed descriptions on the gap wave elevations at different wave frequencies are given in a later section.

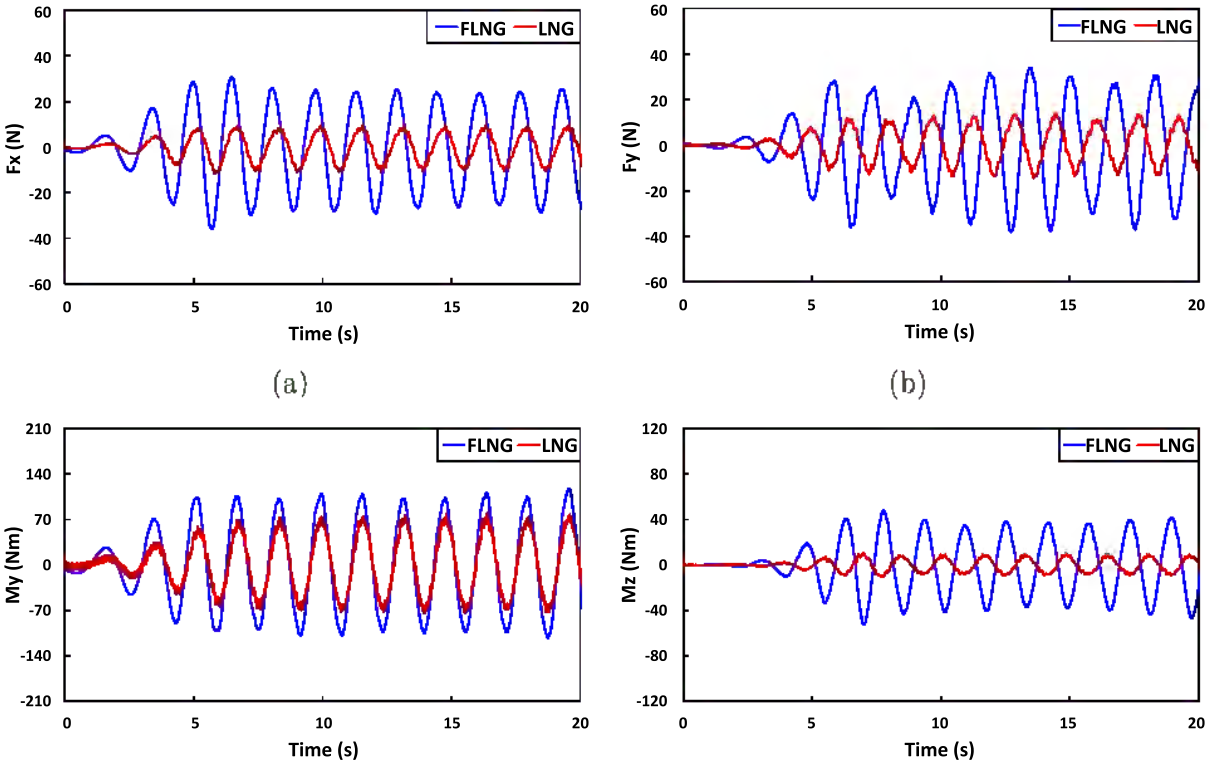

Figure 6.3 Time history measurements of wave induced loads on the FLNG-LNG system at wave frequency of 0.63 Hz

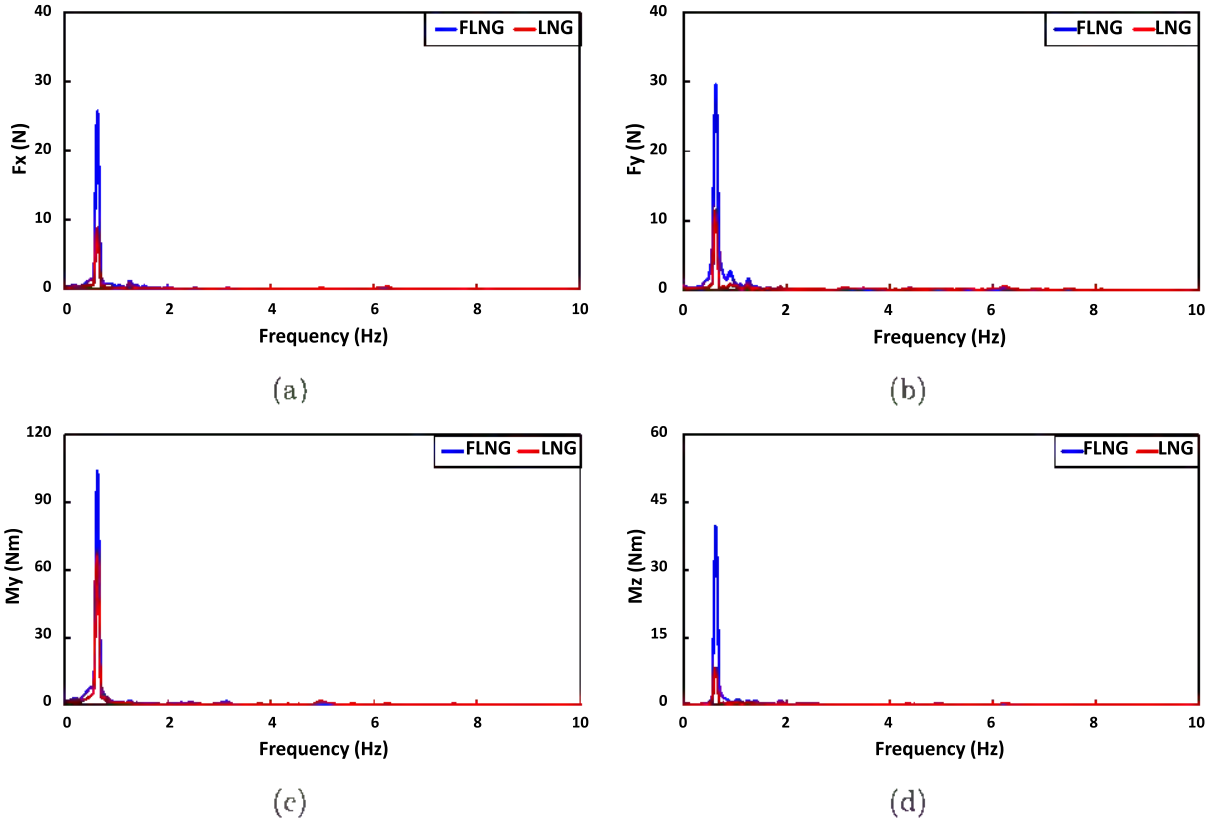

Figure 6.4 FFT analysis on selected wave load signals

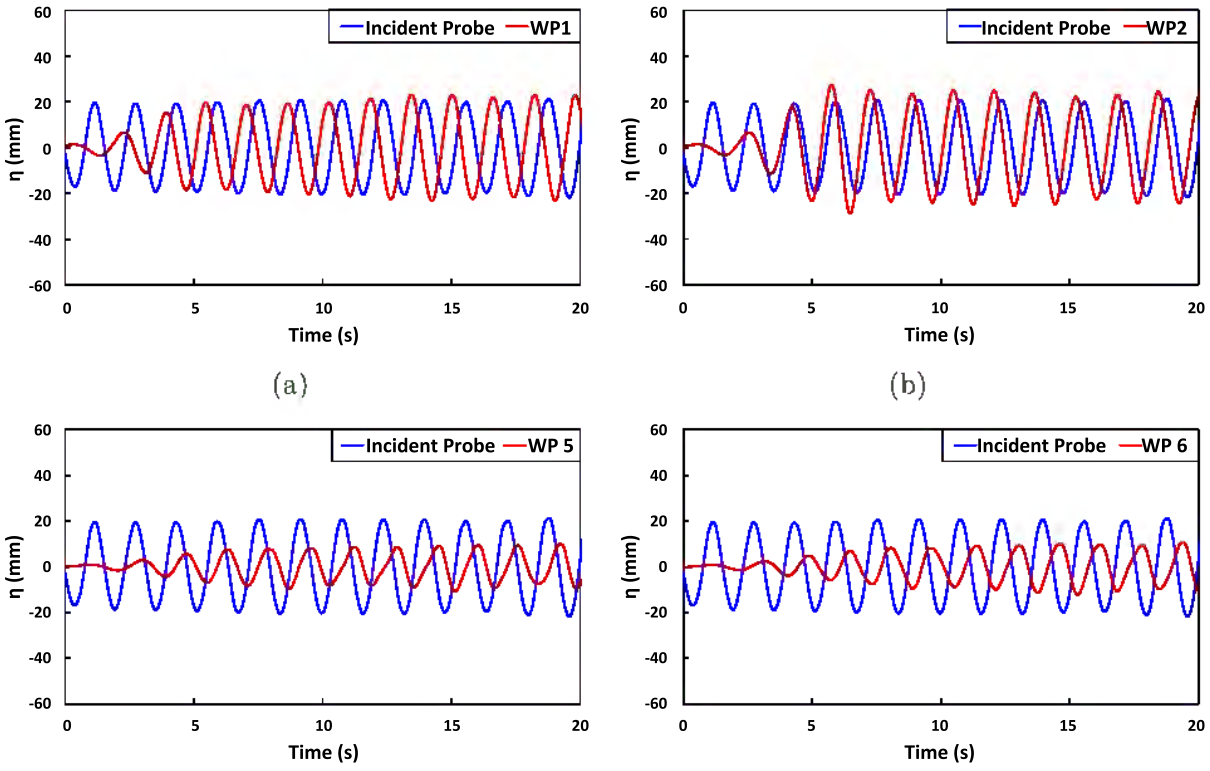

Figure 6.5 Time history measurements of gap wave elevations at wave frequency of 0.63 Hz for selected probe locations

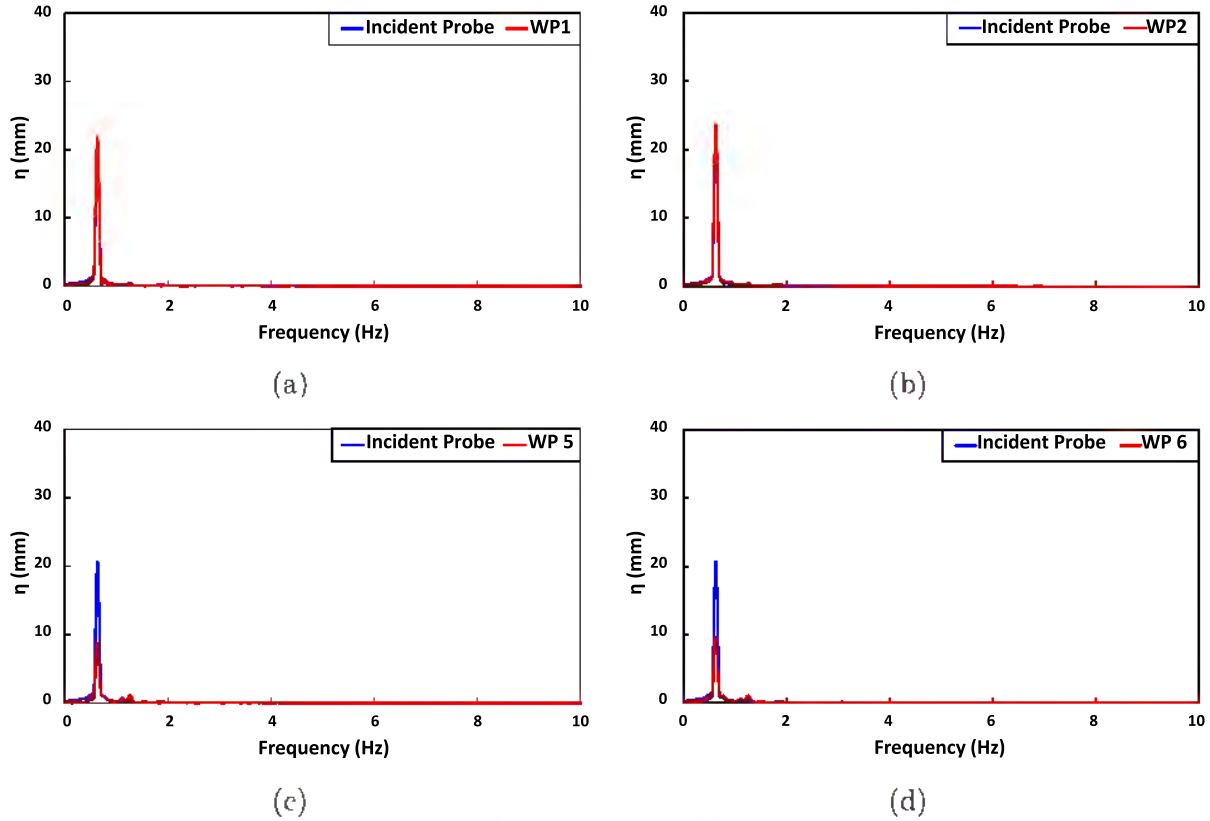

Figure 6.6 FFT analysis on selected gap wave elevation signals

For the comparison with URANS computational results, the measured wave loads are expressed as transfer functions, TF_{Fj} and TF_{Mj}:

$$TF_{Fj} = \frac{F_j}{A} \tag{6.1}$$

$$TF_{Mj} = \frac{M_j}{A} \tag{6.2}$$

where F_j and M_j (j=x, y and z) are the amplitudes for wave induced force and moment on the ship's hull. It also must be noted that the wave induced loads are evaluated referring to the ships' local coordinate systems.

6.4 CFD verification and validation

Before investigating the FLNG-LNG interaction systematically, it is essential to verify and validate the present computational approach. The verification and validation study is carried out for one of the wave conditions f=0.81 Hz. According to Weymouth et al. (2005), large forces and motions tend to result in high numerical errors. This therefore can be regarded as one of the ideal cases to investigate the greatest numerical errors that exist in our computations due to large wave loads predicted.

The grid uncertainty analysis is performed with the smallest time-step, whilst the time-step independence study was carried out with the finest mesh. The details of the grid and time-step adopted in the verification study are presented in Table 6.2.

Table 6.2 Computational grids and time-steps employed in the verification study

	Number of elements	**Time-step (Δt)**
Fine (1)	41 M	$T_{wave}/1024$
Medium (2)	23 M	$T_{wave}/512$
Coarse (3)	9 M	$T_{wave}/256$

Based on similar procedures as described in Section 2.2.4, a summary of the grid-spacing and time-step uncertainties for the tested computational case are listed in Table 6.3 and Table 6.4. Overall, the present computation gives relatively small numerical uncertainties, demonstrating its feasibility for undertaking further systematic simulations.

Table 6.3 Grid convergence study

	r_G	Solutions			R_G	Convergence	$\delta^*_{RE_{G1}}$ (%S1)	U_G (%S1)	EFD
		S1	S2	S3					
FLNG									
TF_{Fx}	$\sqrt{2}$	1224	1250	1375	0.21	MC	0.56	9.71	1250
TF_{Fy}	$\sqrt{2}$	1903	2063	1813	-0.64	OC	~	6.57	2063
TF_{Fz}	$\sqrt{2}$	789	750	801	-0.76	OC	~	3.23	750
TF_{My}	$\sqrt{2}$	4005	4125	3833	-0.41	OC	~	3.65	4125
TF_{Mz}	$\sqrt{2}$	4568	4500	4364	2.00	MC	-1.49	5.70	4500
LNG									
TF_{Fx}	$\sqrt{2}$	578	525	596	-0.74	OC	~	6.14	525
TF_{Fy}	$\sqrt{2}$	817	825	847	0.36	MC	0.53	4.17	825
TF_{Fz}	$\sqrt{2}$	1585	1563	1486	0.29	MC	-0.56	6.15	1563
TF_{My}	$\sqrt{2}$	3501	3563	3405	-0.39	OC	~	2.26	3563
TF_{Mz}	$\sqrt{2}$	1086	1250	1112	-1.19	OC	~	7.55	1250

Table 6.4 Time-step convergence study

	r_T	Solutions			R_T	Convergence	$\delta^*_{RE_{T1}}$ (%S1)	U_T (%S1)	EFD
		T1	T2	T3					
FLNG									
TF_{Fx}	2	1175	1250	1083	-0.45	OC	~	7.11	1250
TF_{Fy}	2	1956	2063	1801	-0.41	OC	~	6.70	2063
TF_{Fz}	2	794	750	883	-0.33	OC	~	8.38	750
TF_{My}	2	3956	4125	3713	-0.41	OC	~	5.21	4125
TF_{Mz}	2	4548	4500	4403	0.49	MC	-1.03	4.06	4500
LNG									
TF_{Fx}	2	543	525	489	0.50	MC	-3.31	4.69	525
TF_{Fy}	2	795	825	789	-0.83	OC	~	2.26	825
TF_{Fz}	2	1591	1563	1455	0.26	MC	-0.62	7.88	1563
TF_{My}	2	3445	3563	3415	-0.80	OC	~	2.15	3563
TF_{Mz}	2	1104	1250	1098	-0.96	OC	~	6.88	1250

To validate the computations, it is necessary to check if the absolute comparison error E between numerical and experimental results is less than the validation uncertainty U_V calculated as a combination of numerical uncertainty U_{SN} and experimental uncertainty U_D.

$$U_V = \sqrt{U_{SN}^2 + U_D^2} \tag{6.3}$$

Comparisons between E and U_V for the wave load transfer functions from the present computation are given in Table 6.5. It is worth mentioning here that the experimental uncertainties U_D are obtained based on the method adopted by Longo and Stern (2005) and Duffy (2008). It is observed that the URANS predictions correlate well with the experimental results. The average comparison errors are 9.21% and 6.52% for the FLNG and LNG respectively. All the investigated parameters are validated except TF_{My} for the LNG. This is considered to be acceptable due to a relatively small discrepancy when comparing against the experimental value.

Table 6.5 Validation of performed URANS simulations

	U_{SN} (%CFD)	U_D (%EFD)	U_V (%CFD)	E (%CFD)
FLNG				
TF_{Fx}	12.03	1.93	12.2	12.1
TF_{Fy}	9.38	10.5	14.1	13.4
TF_{Fz}	8.98	7.57	11.8	10.0
TF_{My}	6.36	4.21	7.63	6.72
TF_{Mz}	7.00	1.21	7.10	3.84
LNG				
TF_{Fx}	7.73	3.42	8.45	4.76
TF_{Fy}	4.74	3.53	5.91	2.82
TF_{Fz}	10.00	4.5	11.0	5.5
TF_{My}	3.12	1.85	3.63	7.44
TF_{Mz}	10.21	3.23	10.7	12.1

6.5 Systematic computations

In the previous section, URANS computation was verified and validated against physical model scale experiments. The results demonstrate the feasibility of the present numerical model in predicting the FLNG-LNG hydrodynamic interactions in waves. Applying analogous numerical approach, the FLNG-LNG system is investigated for different wave frequencies and lateral separations. Furthermore, the computations have also been performed in full scale to quantify scale effects of the FLNG-LNG hydrodynamic interactions in waves. An illustration of the test matrix is given in Table 6.6.

Table 6.6 Matrix of the CFD computations for FLNG-LNG interaction in head sea waves

Scale	Model	Motion	μ	Δx(mm)	ΔS(mm)	Wave frequency f(Hz)
Model Scale (1:100)	FLNG-LNG	Fixed in 6DoF	180°	0	100	0.63, 0.70, 0.75, 0.81, 0.89, 0.99, 1.03, 1.06, 1.10, 1.15
				0	200	0.63, 0.70, 0.75, 0.81, 0.89, 0.99, 1.06, 1.15
				0	350	0.63, 0.70, 0.75, 0.81, 0.89, 0.99, 1.06, 1.15
Full Scale	FLNG-LNG	Fixed in 6DoF	180°	0	10000	0.106, 0.115

6.5.1 FLNG-LNG interaction at different wave frequencies

URANS computations are firstly performed for the lateral separation of ΔS=100mm for different incident wave frequencies. The results gathered from the numerical simulations are compared with experimental data (EFD) and those obtained from potential flow (PF) solver AQWA, which utilises a three-dimensional panel method solving inviscid, irrotational and incompressible fluid around floating structures. For more theoretical explanation of the PF solver, reference can be made to the manual of the software (ANSYS, 2013). Illustrations of URANS time history predictions of wave loads on the FLNG and LNG for the wave frequency of 0.70 Hz are presented in Figure 6.7. Good correlation in the magnitude and period of the wave loads is observed between the URANS and EFD results.

By carrying out FFT analysis on the time history recordings, the wave load transfer functions are derived for the investigated wave frequencies as shown in Figure 6.8. To assess the performance of URANS and PF methods, the discrepancies between numerical predictions and experimental measurements are quantified in Table 6.7 and Table 6.8. For relatively low wave frequencies (0.63 - 0.89 Hz), PF method shows comparable accuracy as URANS prediction. As the wave frequency increases, the URANS computation starts to show better correlation with EFD data. The PF method tends to over-predict the peak magnitude of the transfer functions, particularly for the sway force, heave force, pitch moment and yaw moment. The absolute comparison error for URANS and PF predictions against EFD results varies between 0.05 - 37.0% and 0.14 - 47.4% respectively.

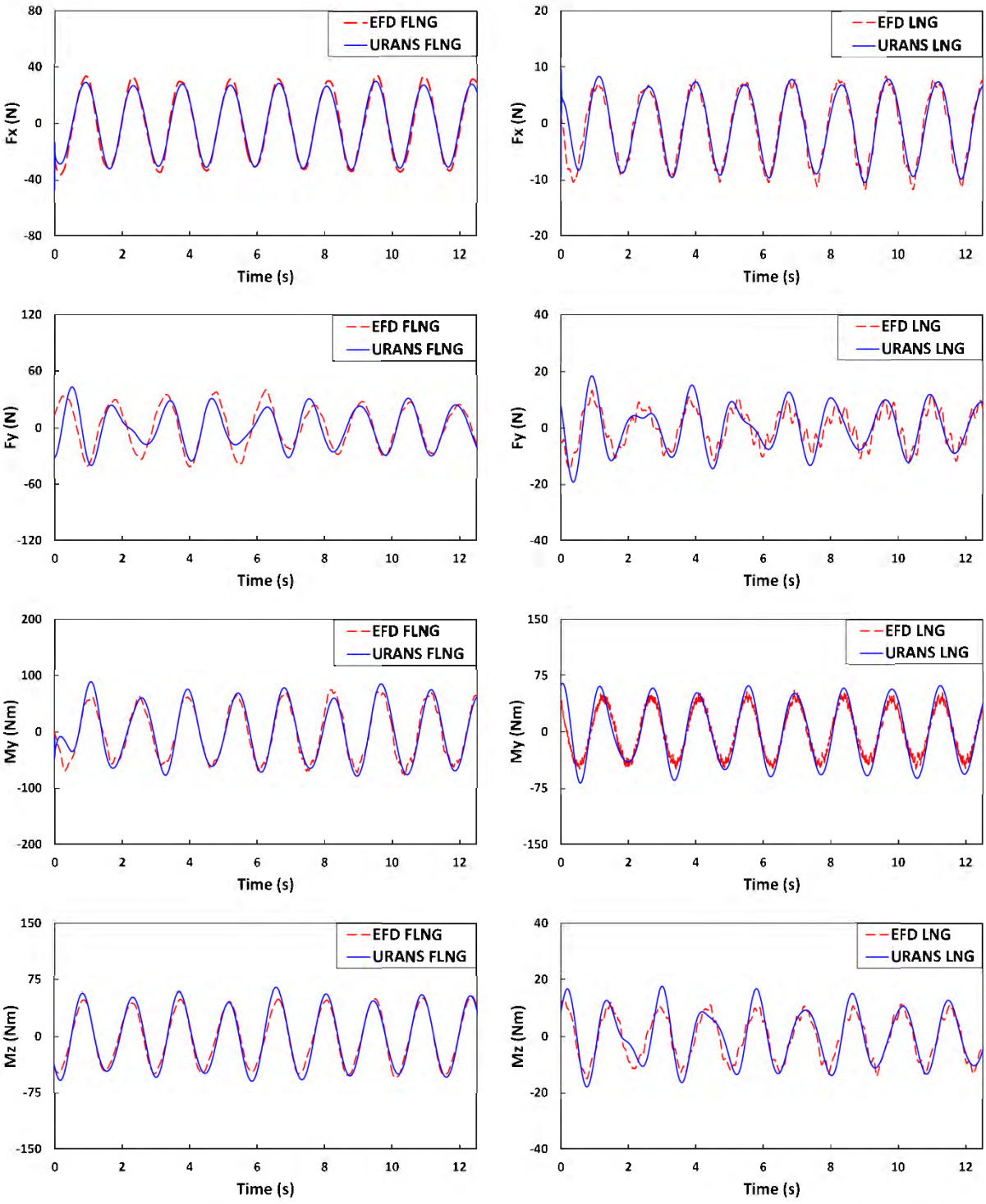

Figure 6.7 Wave loads on the FLNG-LNG system for the lateral separation of ΔS=100 mm at wave frequency of 0.70 Hz

FLNG

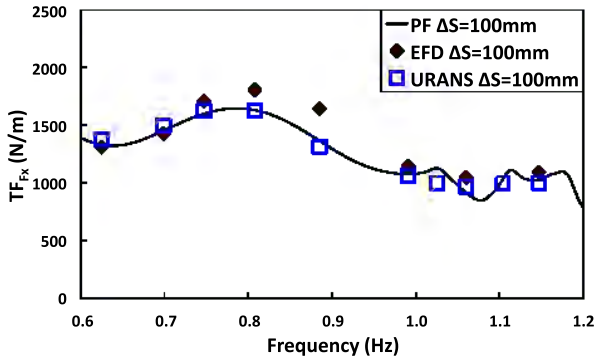

(a)

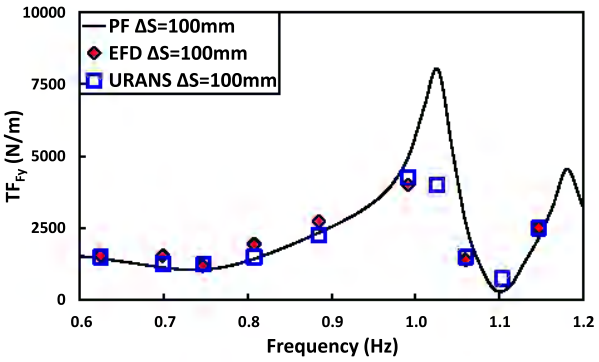

(c)

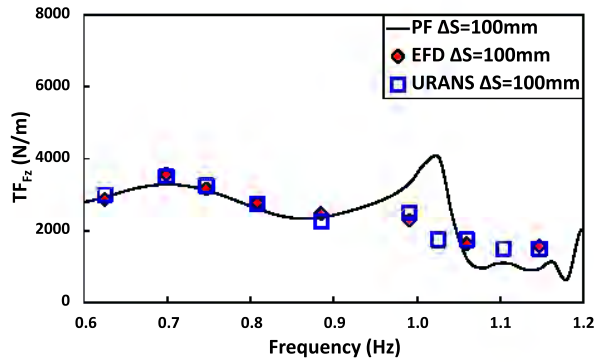

(e)

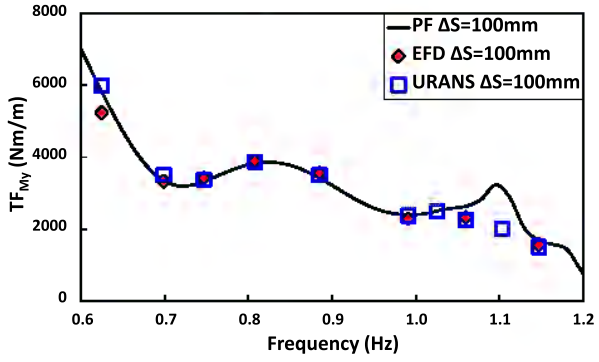

(g)

LNG

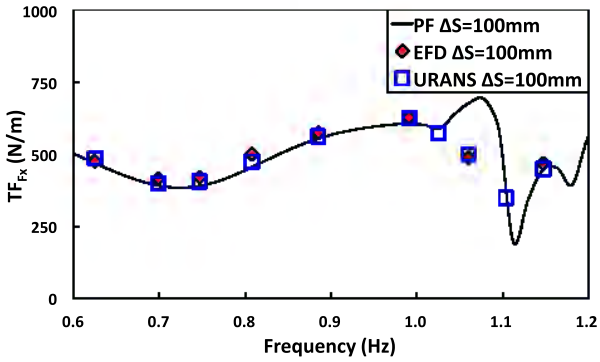

(b)

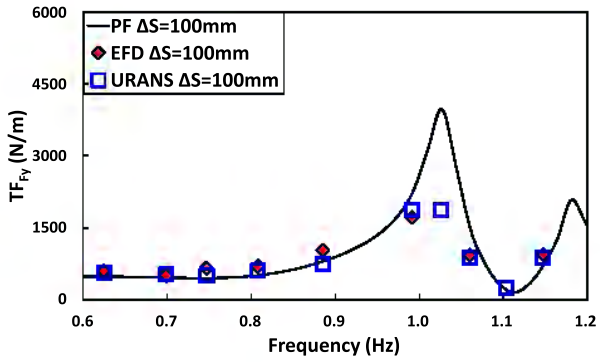

(d)

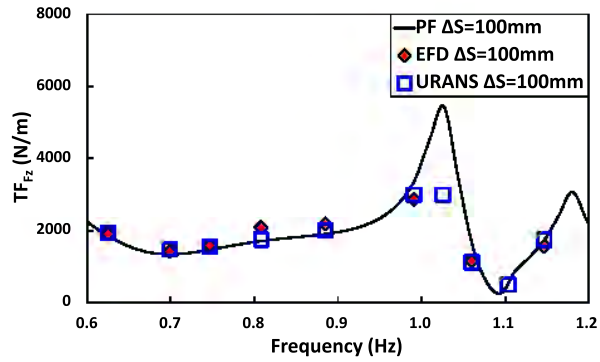

(f)

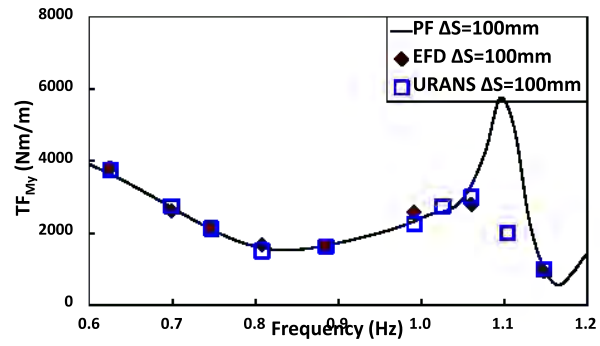

(h)

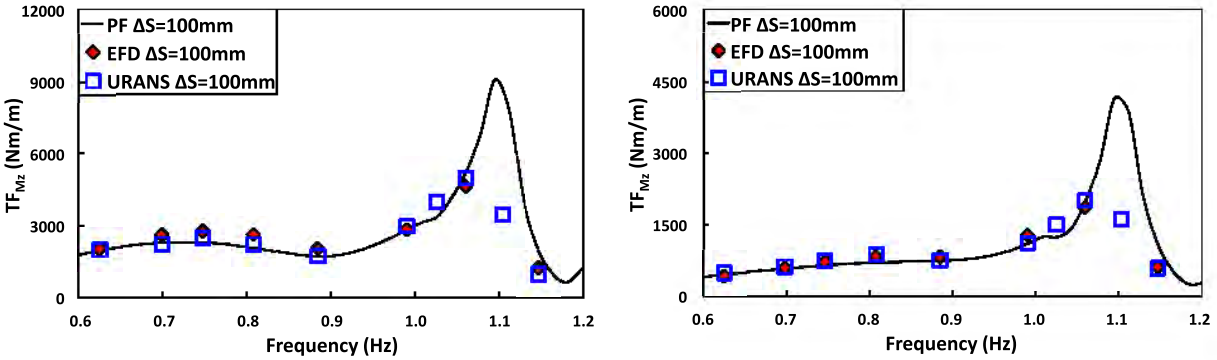

Figure 6.8 Wave load transfer functions of the FLNG-LNG system for the lateral separation of ΔS=100 mm

Table 6.7 Comparison errors of the numerical predictions against experimental results for the wave loads acting on the FLNG

f (Hz)	E(%) TF_{Fx}		E(%) TF_{Fy}		E(%) TF_{Fz}		E(%) TF_{My}		E(%) TF_{Mz}	
	CFD	PF	CFD	PF	CFD	PF	CFD	PF	CFD	PF
0.63	4.76	1.51	-3.17	-7.09	4.76	2.40	12.70	10.06	-1.19	-2.59
0.70	4.76	1.76	-23.81	-36.43	-2.04	-8.91	4.76	0.39	-16.40	-13.83
0.75	-5.26	-6.94	5.26	-11.61	2.83	-1.17	-1.36	-2.97	-10.53	-19.66
0.81	-11.11	-10.67	-29.63	-35.38	-1.01	-6.46	-0.36	-1.52	-17.28	-26.28
0.89	-25.24	-20.42	-21.77	-16.89	-9.59	-4.09	-1.76	-4.09	-17.42	-18.45
0.99	-7.56	-6.27	5.88	19.17	8.57	31.07	3.76	4.75	4.76	-0.14
1.06	-8.17	-14.54	6.98	47.41	6.98	-33.92	-3.36	11.82	6.98	10.66
1.15	-9.38	-6.97	0.05	-14.95	-4.17	-47.40	-4.17	6.96	-25.00	36.46

Table 6.8 Comparison errors of the numerical predictions against experimental results for the wave loads acting on the LNG

f (Hz)	E(%) TF_{Fx}		E(%) TF_{Fy}		E(%) TF_{Fz}		E(%) TF_{My}		E(%) TF_{Mz}	
	CFD	PF	CFD	PF	CFD	PF	CFD	PF	CFD	PF
0.63	2.32	-1.40	-5.82	-23.88	1.69	-2.64	-1.59	-4.64	14.29	6.91
0.70	-4.17	-6.33	5.88	-8.93	4.76	-6.12	4.76	3.35	4.76	-1.52
0.75	-3.64	-7.75	-31.58	-46.86	-1.05	-7.18	0.93	-0.16	3.51	-10.62
0.81	-5.26	-9.62	-15.74	-37.64	-19.05	-21.77	-11.11	-4.88	4.76	-17.28
0.89	-2.28	-3.72	-36.99	-29.13	-9.59	-14.91	-1.16	0.71	-9.59	-11.02
0.99	-0.57	-3.56	8.57	22.34	4.76	15.20	-14.29	-10.63	-14.29	-15.97
1.06	2.33	27.87	-6.31	38.04	-3.36	30.09	6.98	16.52	6.98	5.59
1.15	-4.17	-4.64	-7.14	-33.28	10.71	10.47	6.25	10.63	-4.17	43.65

It is seen from Figure 6.8 that the sway force, heave force and yaw moment transfer functions vary significantly at relatively high wave frequency conditions. This is considered as a consequence of gap wave resonance, where the amplified gap waves induce asymmetric pressure distributions on the FLNG and LNG hulls, and therefore large disturbances on the wave loads. Figure 6.10 presents the significant variation of gap waves under different wave frequencies from URANS predictions and EFD measurements. At the wave frequency of 0.63 Hz, the gap wave elevations recorded at WP 5 and 6 are suppressed to half that of the incident waves. On the other hand, at the wave frequency of 1.15 Hz, resonance occurs and excites the gap waves to three times of the incident wave height.

It is observed that the gap wave response is generally sinusoidal, which enables a constant gap wave height H_G to be estimated from the FFT analysis. For the convenience of comparing gap wave response at different locations and wave frequencies, the non-dimensional gap wave height H_G' is introduced, representing the ratio between H_G and the incident wave height H_O. Figure 6.11 presents comparisons of URANS, EFD and PF predictions on the gap wave responses at different wave frequencies for the lateral separation of ΔS=100 mm. It is found that the pattern of gap waves exhibits great similarities when the incident wave frequency is below 0.90 Hz, though there are discrepancies in the magnitude of H_G' between the numerical and experimental results at certain regions. For positions within the range of -0.5 - 0.0 m, the gap waves are suppressed to less than half of the incident wave amplitude at the low frequency conditions (0.63 - 0.89 Hz). The tendency of H_G' varies differently for high wave frequency conditions (1.06 Hz and 1.15 Hz) close to the natural frequency of the fluid (1.23 Hz) in the gap. This natural frequency, which is outlined in Figure 6.9, is estimated based on an empirical formulae from Saitoh et al. (2006) and Moradi et al. (2015) as given in Equation (6.4). The amplitude of the gap waves within the range of -1.0 - 1.0 m are magnified to 2 - 4 times of the incident wave amplitude due to resonance effect.

$$f_n = \sqrt{\frac{g}{\frac{\Delta S \times B}{d\text{-}T} + T}} \tag{6.4}$$

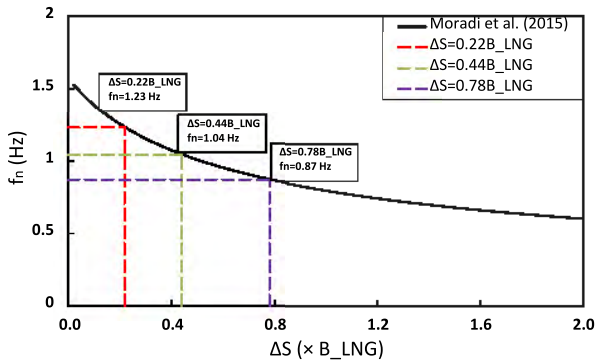

Figure 6.9 Estimation of the natural frequency for gap fluid

Wave frequency f=0.63 Hz

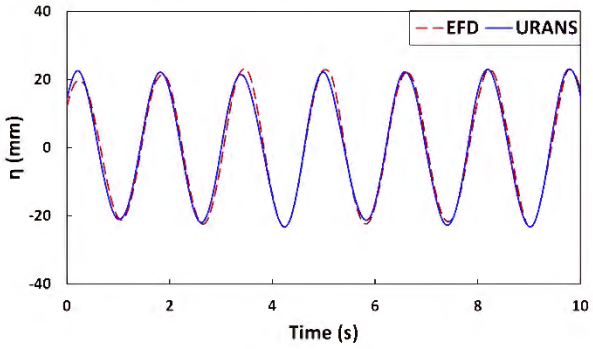

WP 1

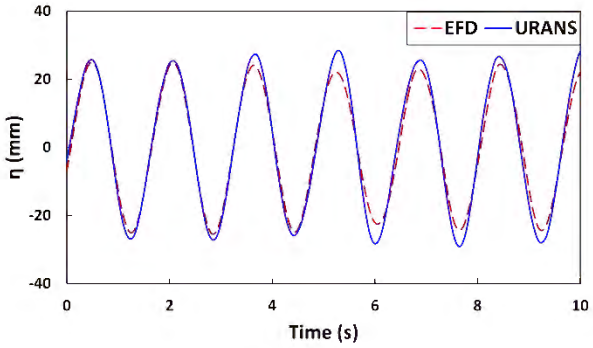

WP 2

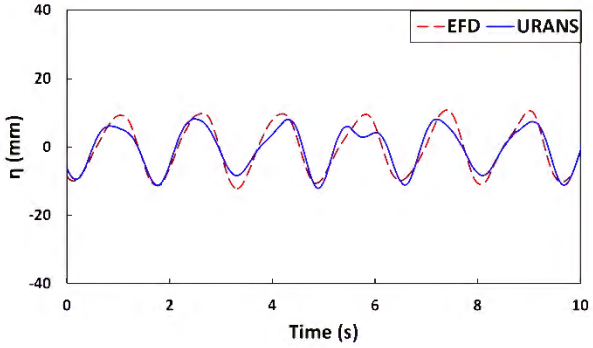

WP 4

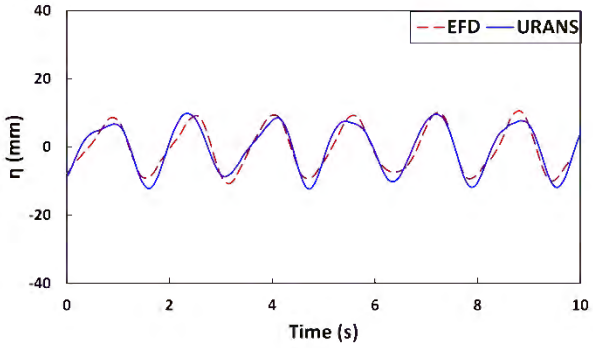

WP 5

Wave frequency f=1.15 Hz

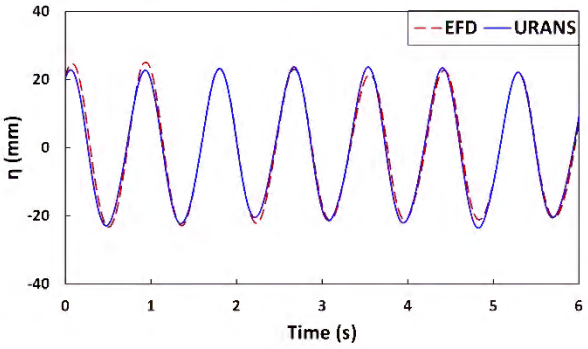

WP 1

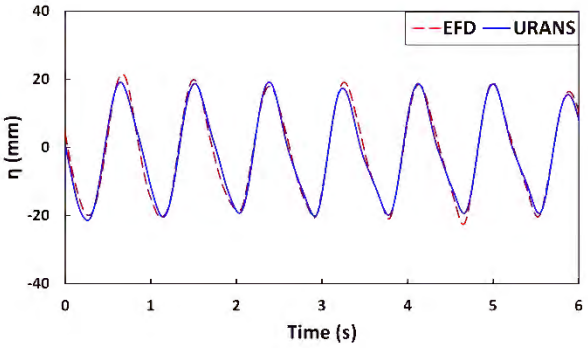

WP 2

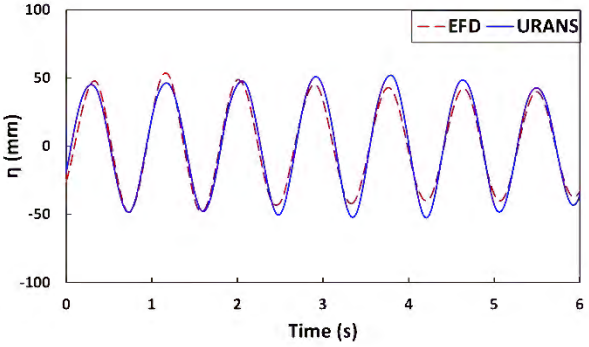

WP 4

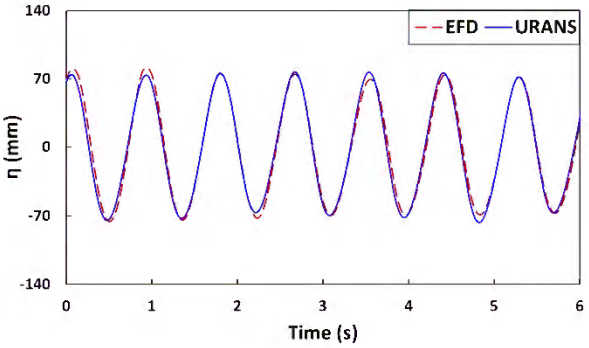

WP 5

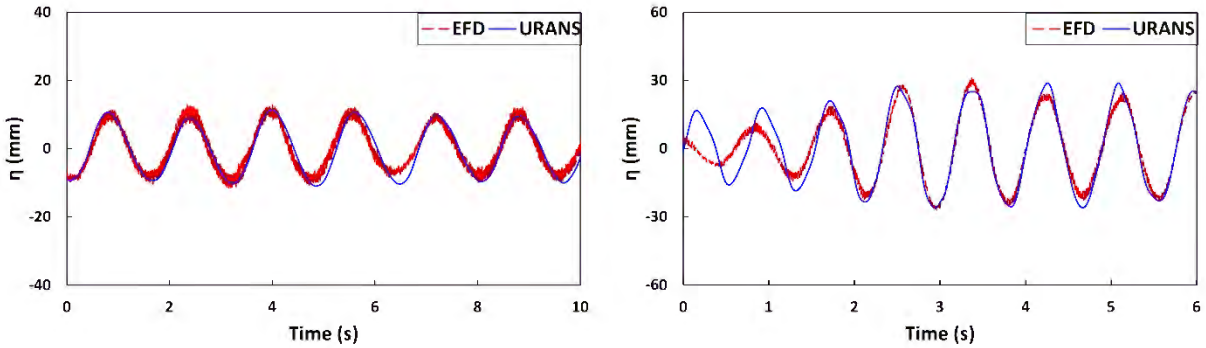

WP 8 WP 8

Figure 6.10 URANS predictions of gap wave elevation of the FLNG-LNG system comparing against experimental measurements for the lateral separation of ΔS=100 mm at wave frequencies of 0.63 Hz and 1.15 Hz

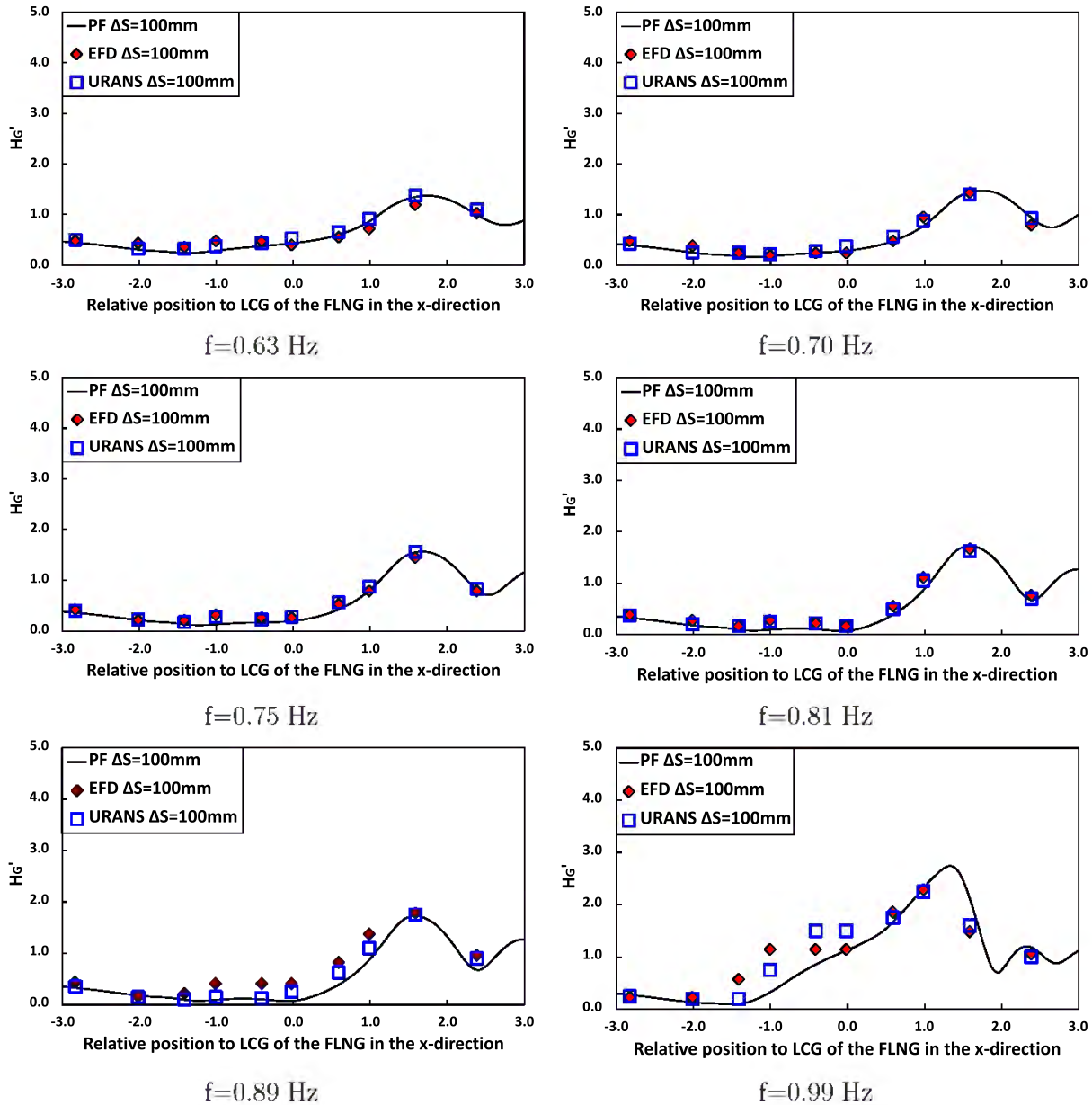

f=0.63 Hz f=0.70 Hz

f=0.75 Hz f=0.81 Hz

f=0.89 Hz f=0.99 Hz

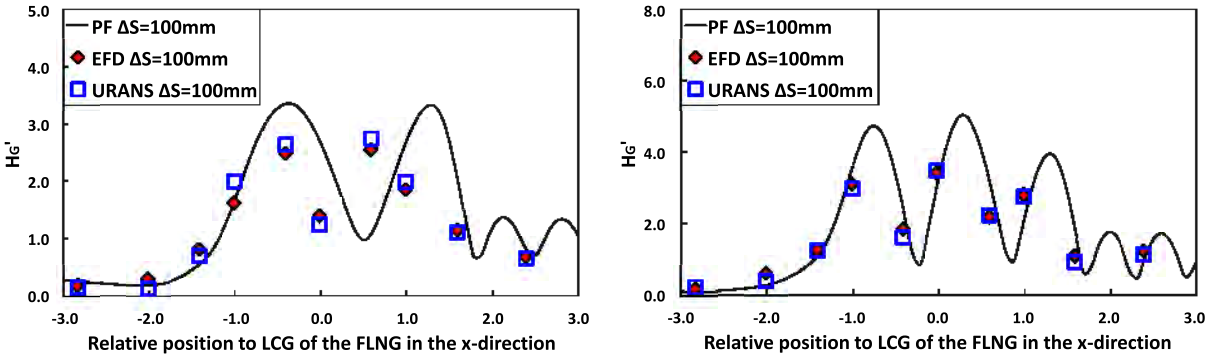

f=1.06 Hz f=1.15 Hz

Figure 6.11 URANS, EFD and PF predictions on the non-dimensional gap wave height for the lateral separation of ΔS=100 mm

It is seen from Figure 6.11 that the URANS method provides more accurate predictions on H_G' especially for the relatively high wave frequency conditions (0.99 Hz, 1.06 Hz and 1.15 Hz). On the other hand, the PF method tends to over-estimate the peak values of gap wave height at these wave frequencies. As discussed in the literature review, this is primarily due to the absence of viscous damping in the linear potential flow solver. This observation also explains the better correlation of URANS predictions on the wave load transfer functions over PF method when comparing with EFD results for relatively high wave frequency conditions. For better PF calculations, additional damping has to be added to the gap waves and it requires tuning based on reliable EFD data. It is also found that the gap wave resonance is not the only dominant factor that influences the wave loads on the FLNG and LNG. For instance, at the wave frequency of 1.06 Hz where the gap waves are significantly exaggerated, the sway force is not comparable to that for the wave frequency f=0.99 Hz. To explain this, the hydrodynamic pressure distribution on the FLNG and LNG hulls are presented in Figure 6.12. This specific time step corresponds to the highest gap wave elevation at the location of x=0 m, where the peak repulsive sway force appears. When comparing the two different wave frequencies, one can observe greater hydrodynamic pressure on the lee wall of the ship hulls for the case of f=0.99 Hz. This leads to a more significant portion of repulsive sway force adding on top of that caused by gap wave resonance and therefore results in a greater net sway force when compared to the wave frequency of f=1.06 Hz

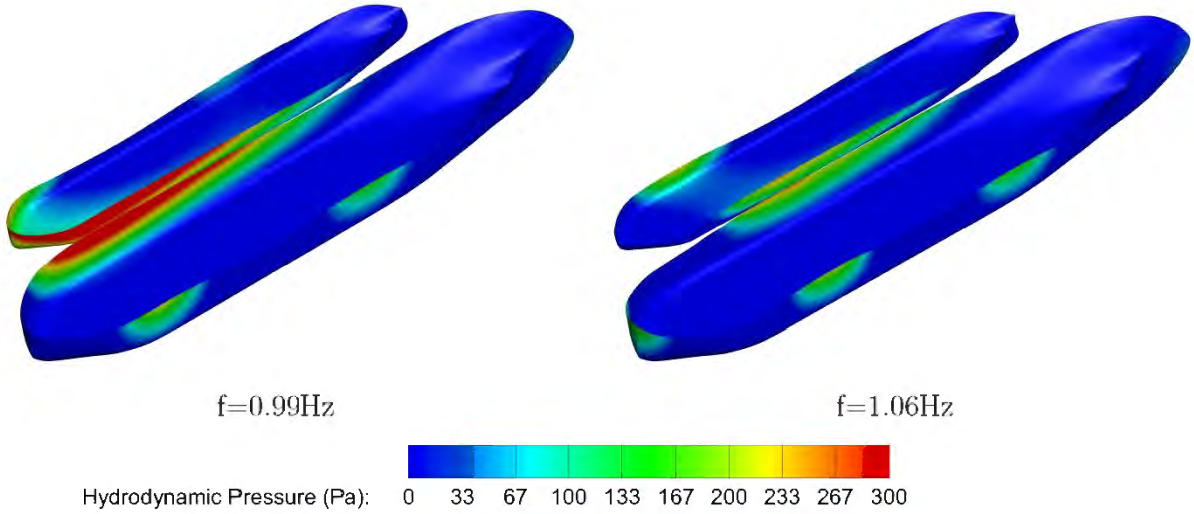

Figure 6.12 Hydrodynamic pressure on the FLNG and LNG hull for the lateral separation of ΔS=100 mm

6.5.2 Flow field around the FLNG-LNG offloading system

To visualise wave diffraction around the FLNG-LNG system in a side-by-side offloading configuration, contours of the free surface elevation are presented in Figure 6.13 for the lateral separation of ΔS=350 mm. For low frequency wave conditions, the FLNG-LNG system acts like an integrated floating structure where the incident waves diffract directly at the forward region of the system. The wave energy hardly passes into the gap between the two ships. As a result, the amplitude of the gap waves becomes less significant than that of the incident waves. As the wave frequency increases, the incident waves start to "penetrate" the FLNG-LNG system, meanwhile the wave frequency shifts closer to the natural frequency of the fluid trapped in the gap and results in great exaggerations of the gap waves.

To understand the fluid dynamics behind the gap wave resonance in head sea, the velocity field around the FLNG-LNG cross section x=0 m is presented in Figure 6.14. It can be seen that the gap wave response induces strong cross flow around the two ships, however with much less noticeable vortical structures when compared to the beam sea conditions shown in Moradi et al. (2015). When t=0Tp, the gap wave is at its crest where the fluid starts to escape from the confined region between the two ships and a small vortex forms near the inner bilge of the FLNG. As time marches forward, the gap wave keeps decreasing and reaches its lowest elevation at t=3Tp/8. After that, the fluid starts to be driven back from the far field to the gap at t=Tp/2. This leads to the uprising of gap wave elevation, which reaches its maximum at t=7Tp/8. One can also find that there is a high velocity region in the gap consistently throughout the presented time intervals. The outcome from this is a reduction of

hydrodynamic pressure on the leewall of the FLNG and LNG hulls, which leads to strong attraction force (t=3Tp/8) that can be hazardous for operation.

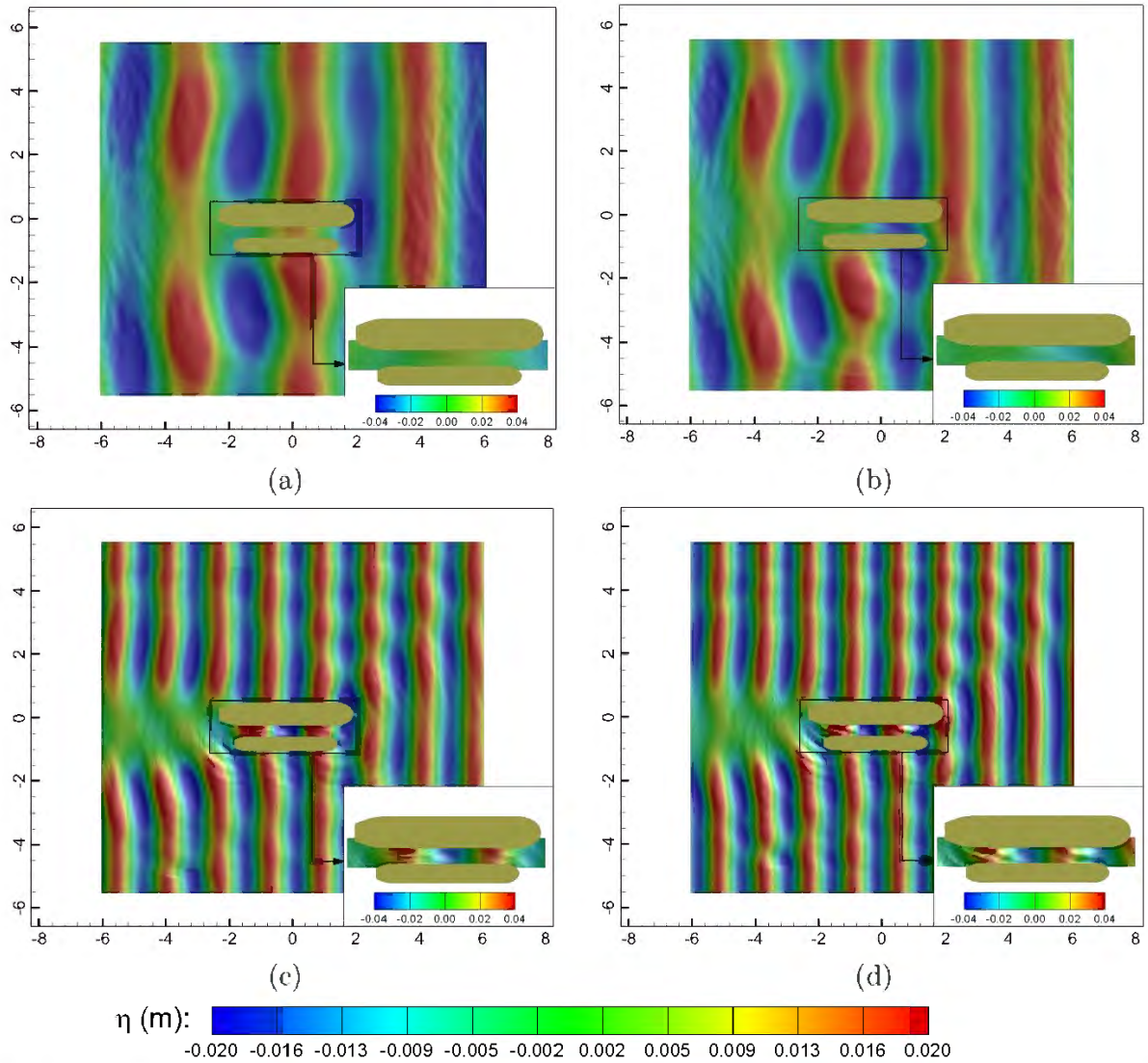

Figure 6.13 Wave diffraction around the FLNG-LNG system for the lateral separation of ΔS=350 mm at different wave frequencies (a) 0.63 Hz; (b) 0.70 Hz; (c) 0.99 Hz and (d) 1.06 Hz

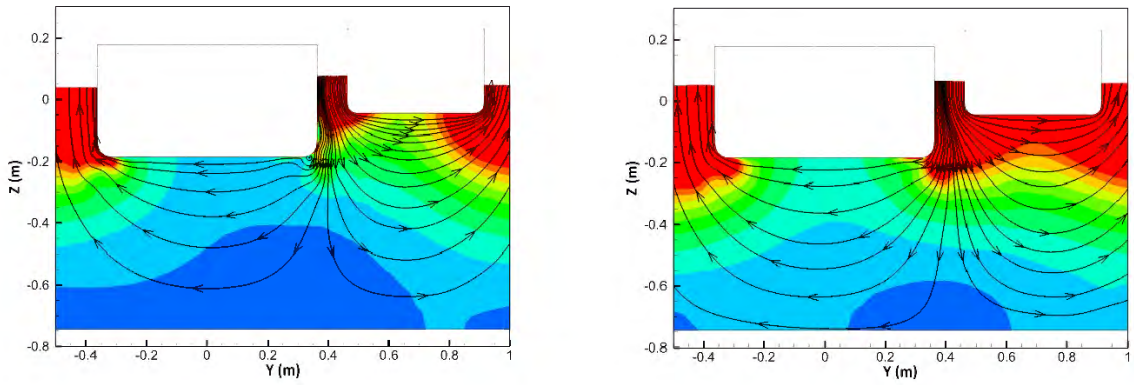

t=0Tp t=T_p/8

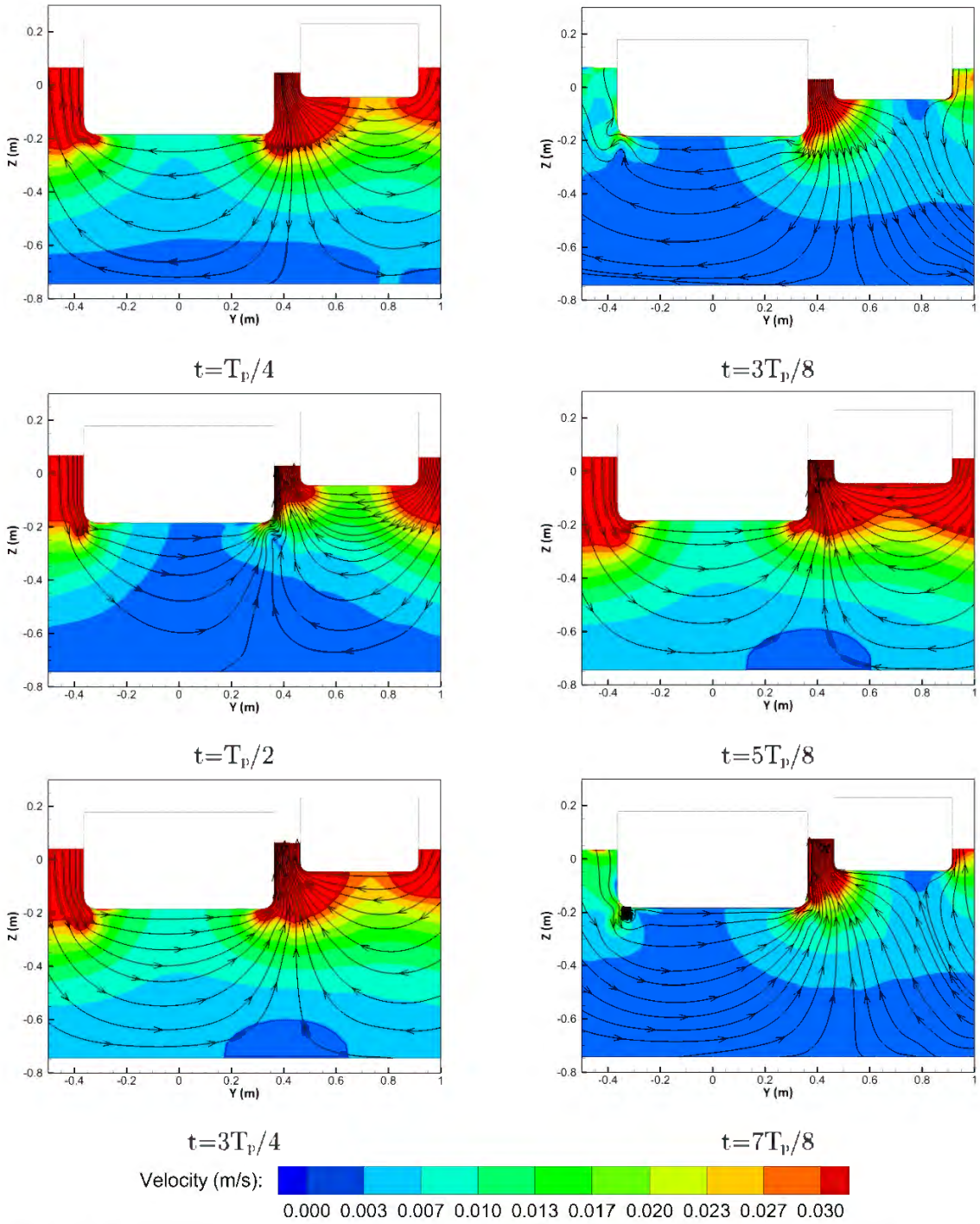

Figure 6.14 Cross-sectional view of the flow field around FLNG-LNG system for the lateral separation of ΔS=100 mm and wave frequency of f=1.06 Hz

6.5.3 Influence of lateral separation between FLNG and LNG

In this section, the influence of lateral separations on the FLNG-LNG hydrodynamic interactions has been investigated. Figure 6.15 presents the variation of non-dimensional gap

wave height H_G' for the FLNG-LNG lateral separations of ΔS=200 mm and ΔS=350 mm respectively. When comparing against Figure 6.11, the pattern of gap waves exhibits similarities for the three lateral separations at low wave frequencies of 0.63 Hz, 0.70 Hz and 0.75 Hz. As the wave frequency increases, the gap waves for the condition with lateral separation of ΔS=350 mm firstly starts to be exaggerated at the wave frequency of 0.81 Hz. Exaggeration of gap waves for condition with less lateral separations starts at higher wave frequencies, 0.99 Hz for ΔS=200 mm and 1.06 Hz for ΔS=100 mm. This indicates the occurrence of gap wave resonance shifts to higher frequencies when reducing the lateral separation between the FLNG and LNG. This is also evident from the inverse relationship between the lateral separation and gap fluid natural frequency in Equation (6.4). In addition, the lateral separation also has an influence on the significance of gap wave resonance. Among the three conditions tested ΔS=100 mm, 200 mm and 350 mm, it was found that a less lateral separation brings severer wave response in the gap between the FLNG and LNG hulls.

In Figure 6.15, for the lateral separation of ΔS=200 mm, URANS computation still provides better predictions on H_G' than PF method when comparing against EFD measurements, especially for the high wave frequency conditions 0.99 - 1.15 Hz. When the lateral distance increases to 350 mm, this advantage becomes less profound. Although URANS simulation still demonstrates slightly better accuracy, the discrepancies between PF and EFD measurements on H_G' has been reduced significantly for the lateral separation of ΔS=350 mm. This implies that PF method is suitable to model the gap wave responses for relatively large lateral separations with an acceptable level of accuracy.

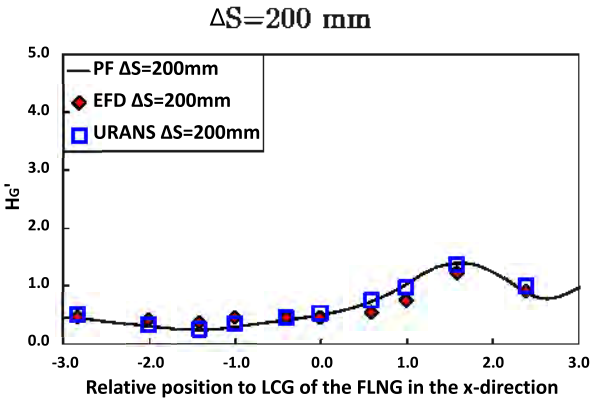

f=0.63 Hz

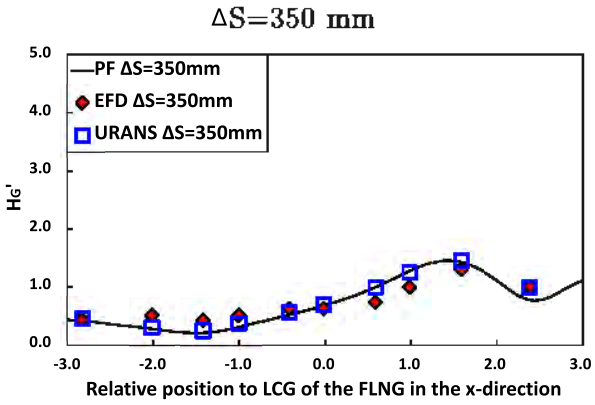

f=0.63 Hz

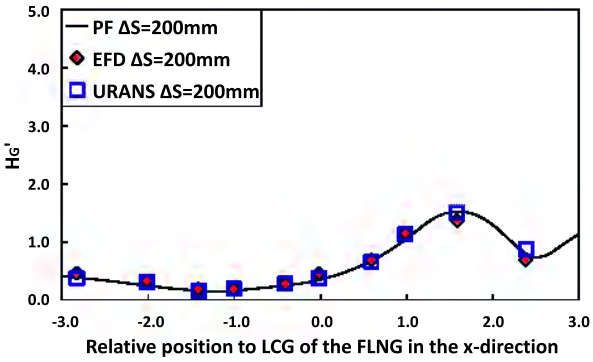

f=0.70 Hz

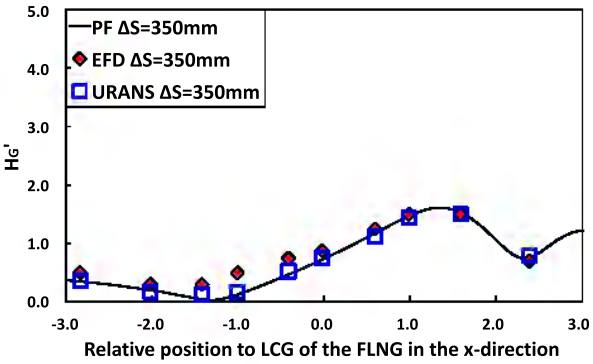

f=0.70 Hz

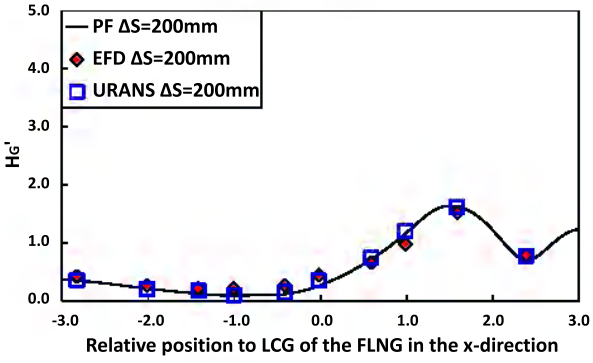

f=0.75 Hz

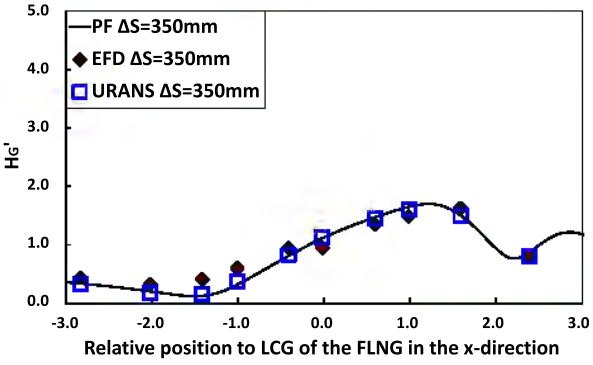

f=0.75 Hz

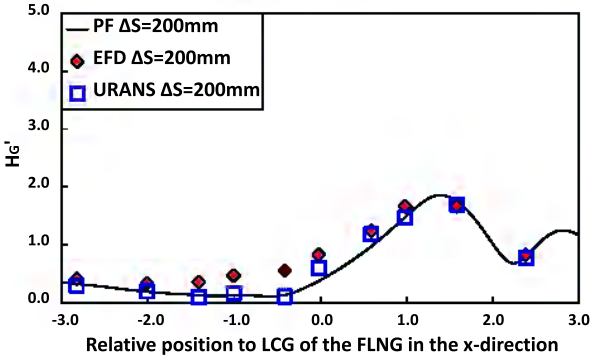

f=0.81 Hz

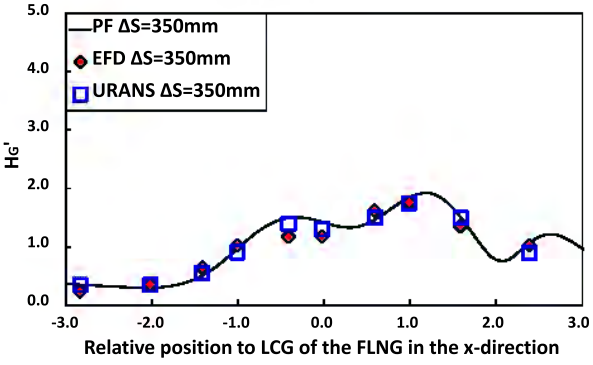

f=0.81 Hz

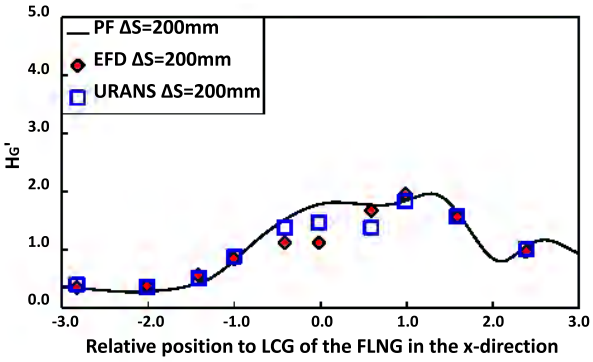

f=0.89 Hz

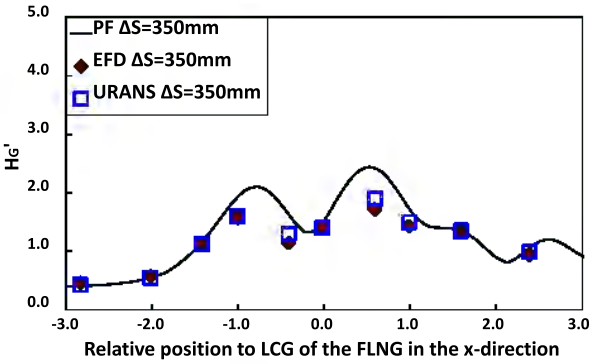

f=0.89 Hz

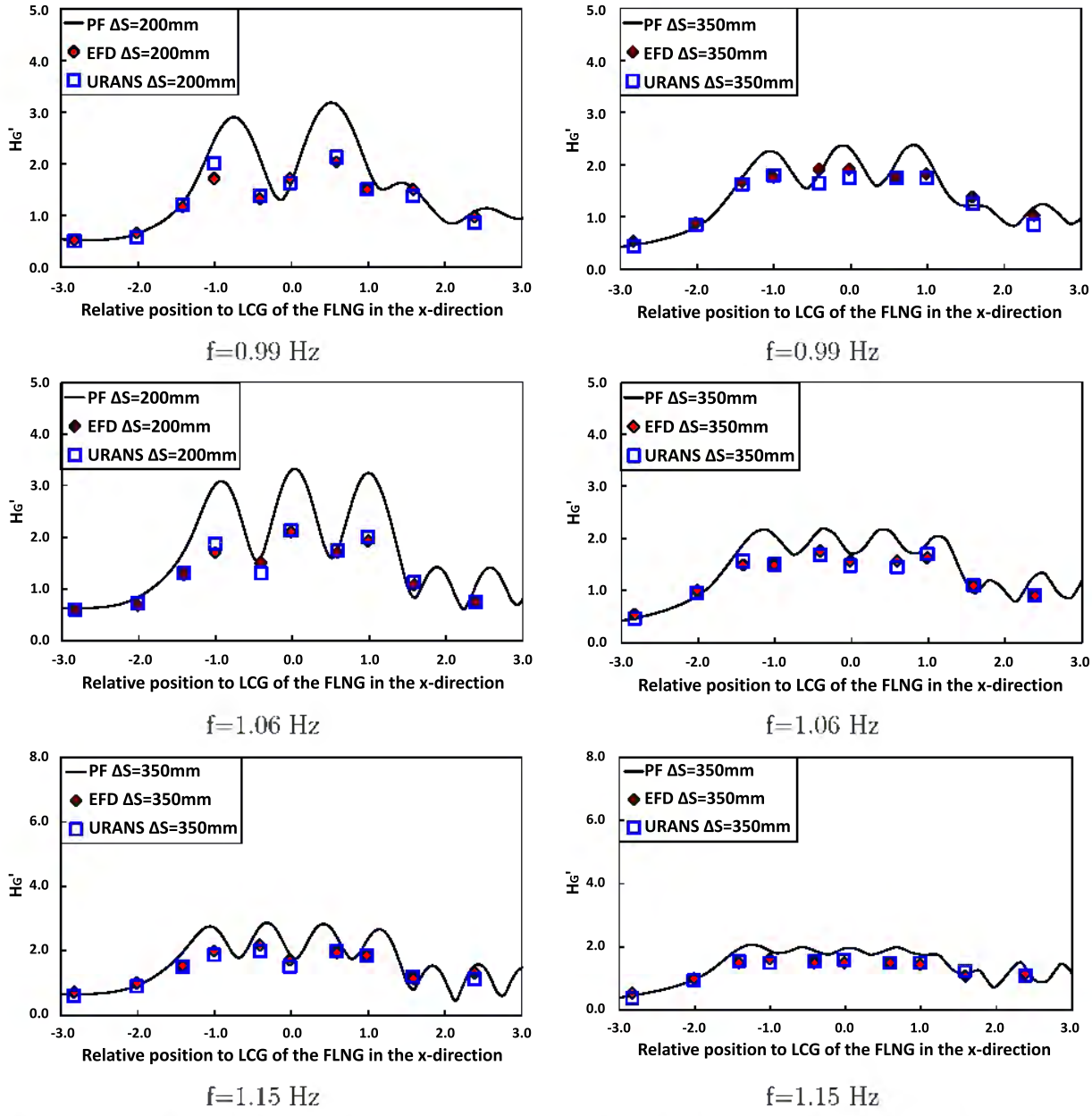

Figure 6.15 Non-dimensional gap wave height for the lateral separations of ΔS=200 mm and ΔS=350 mm

The variation of lateral separation also influences the wave loads on the FLNG and LNG hulls, which are associated with the gap wave responses. Figure 6.16 presents the wave induced forces and moments from URANS, EFD and PF predictions for the investigated lateral separations of ΔS=200 mm and 350 mm. Combining with the wave load results for ΔS=100 mm in Figure 6.8, some interesting aspects are highlighted here. For the surge force given in Figure 6.16 (a) and (b), fluctuations on the transfer function are observed at wave frequencies close to the natural frequency of the gap fluid. These fluctuations start at relatively higher wave frequencies for conditions with less lateral separations. For the sway and heave force transfer functions in Figure 6.16 (c) - (f), similar to that observed in the gap wave responses.

when reducing the lateral separation between the FLNG and LNG, occurrence of the peak transfer function shifts to higher frequencies. In addition, the lateral separation also influences the significance of the exaggerations on the transfer functions and it was found that a less lateral separation brings a peak transfer function of greater magnitude. The effects of changing lateral separation on the pitch and yaw moment transfer functions exhibit a similar trend as shown in Figure 6.16 (g) - (j).

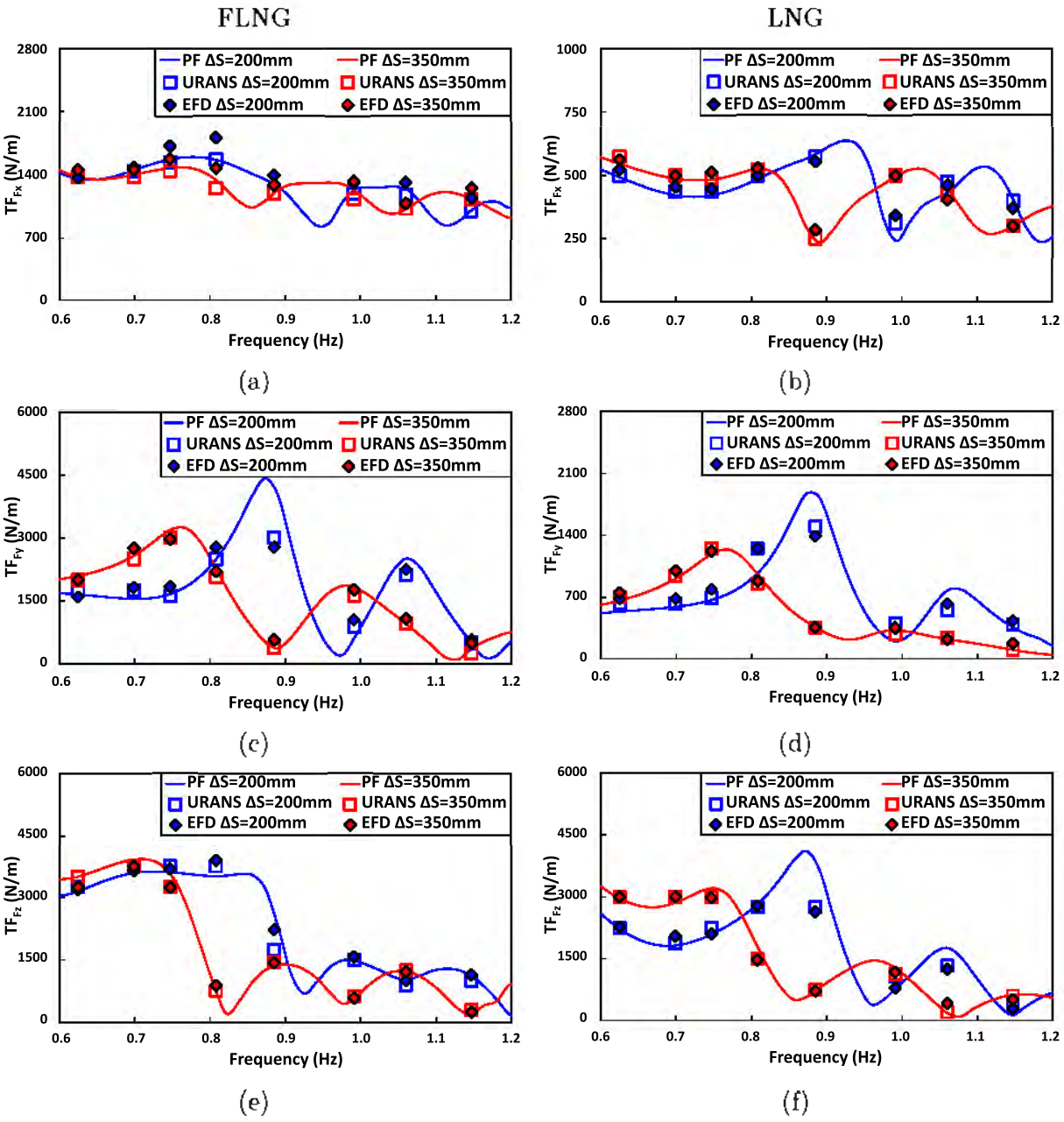

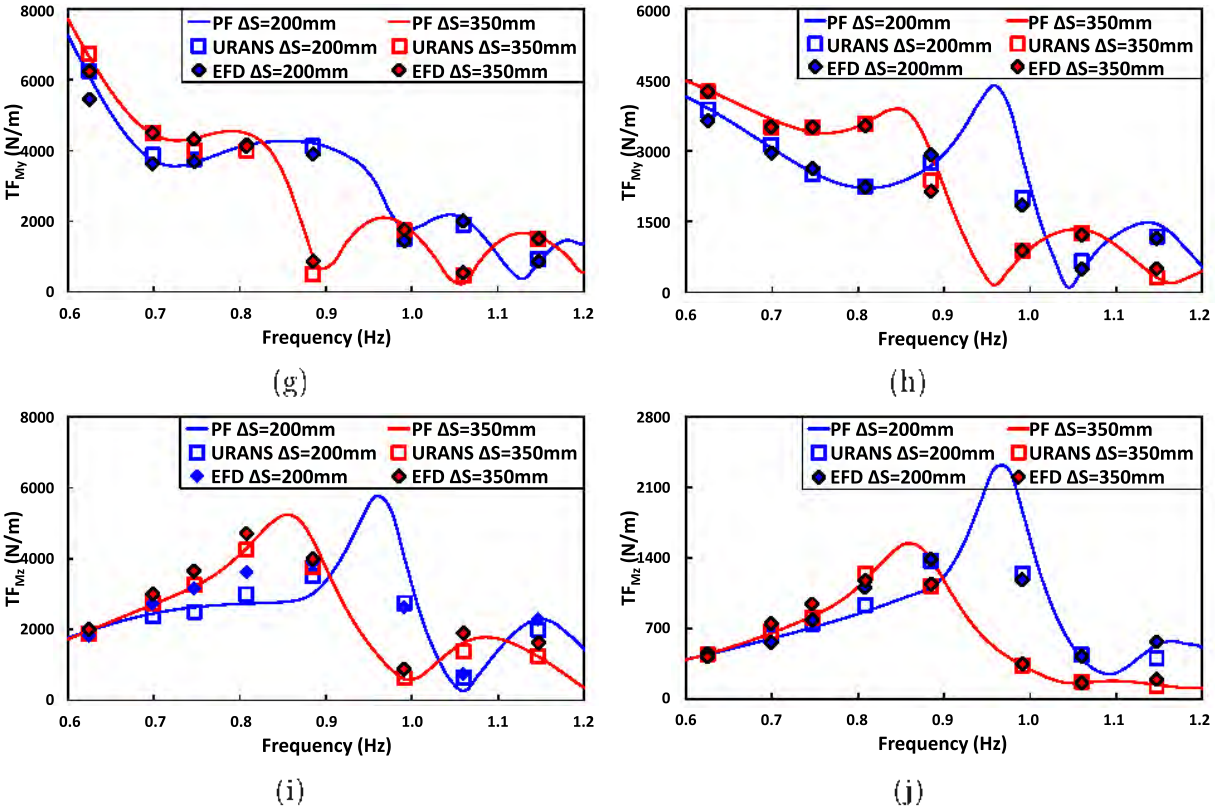

Figure 6.16 Transfer functions of wave loads on the FLNG and LNG for different lateral separations

With increasing lateral separation, the accuracy of PF predictions on the gap wave response increases. This trend is also found on the frequency domain wave loads given in Figure 6.16. The discrepancy between peak transfer functions from PF calculation and EFD measurement reduces as the lateral separation increases. For the condition of ΔS=350 mm, the URANS, EFD and PF give very close predictions for the wave forces and moments including the peak values. As above, in the absence of a tuned damping lid, PF method is still feasible to provide predictions on the wave loads with satisfactory level of accuracy for lateral separations greater than 200 mm.

6.5.4 Full scale predictions on FLNG-LNG interaction

To investigate scale effects in the FLNG-LNG interactions in waves, full scale URANS computations are carried out for the wave frequencies of 0.106 Hz and 0.115 Hz at the lateral separation of ΔS=10 m. The two cases correspond to the model scale conditions of wave frequencies of 1.06 Hz and 1.15 Hz at the lateral separation of ΔS=100 mm by Froude scaling. The full scale fluid domain and computational grid are scaled isotropically, therefore shares the same level of grid density when compared to model scale. Additional prism cells are added to

the full scale ships for achieving similar y+ distributions along the hull and resolving the boundary layer to the same extent as model scale conditions.

In this section, comparisons are made on the wave loads, gap wave elevations and diffracted wave patterns between the model and full scale computations. Figure 6.17 presents the time series of the model and full scale wave loads acting on the two ships for the wave frequency of 1.06 Hz (MS)/ 0.106 Hz (FS). It is observed that the two series of data correlates well, which reflects insignificant influence of scale effects in the prediction of wave loads for the case studied.

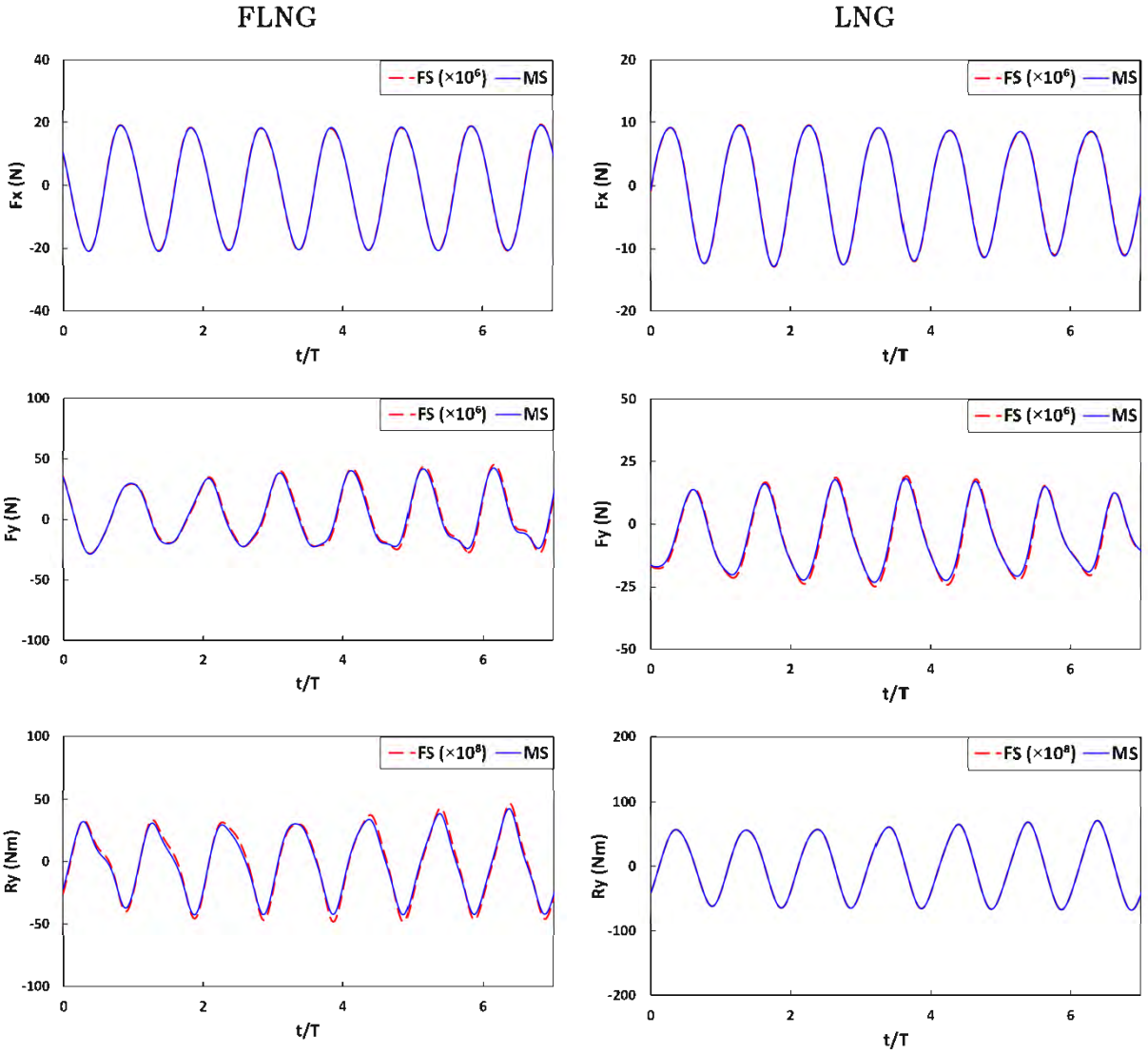

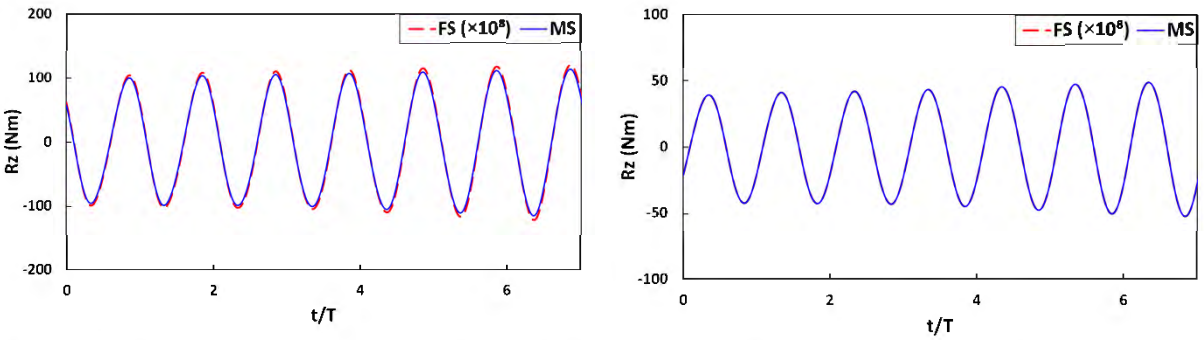

Figure 6.17 Comparison of model and full scale time history wave loads for the lateral separation of ΔS=100 mm (MS)/ ΔS=10 m (FS) at wave frequency of 1.06 Hz (MS)/ 0.106 Hz (FS)

To further investigate scale effects in the gap wave predictions, the model and full scale non-dimensional gap wave elevations η' are compared at different wave probe locations as given in Figure 6.18. Again, it is found that scale effects barely influence the gap wave responses. Model and full scale wave diffractions around the FLNG-LNG system are presented in Figure 6.19. The wave patterns exhibit great similarity, which demonstrates the minor influences of scale effects in the presented FLNG-LNG head sea interaction cases. As above, this part of the study has shown that model scale simulations are able to represent the full scale conditions for the presented FLNG-LNG interaction in head sea waves.

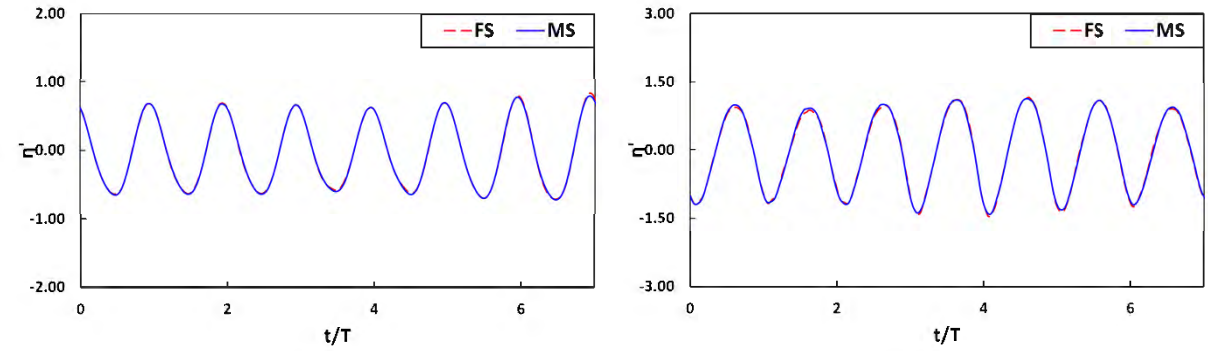

WP 1 WP 2

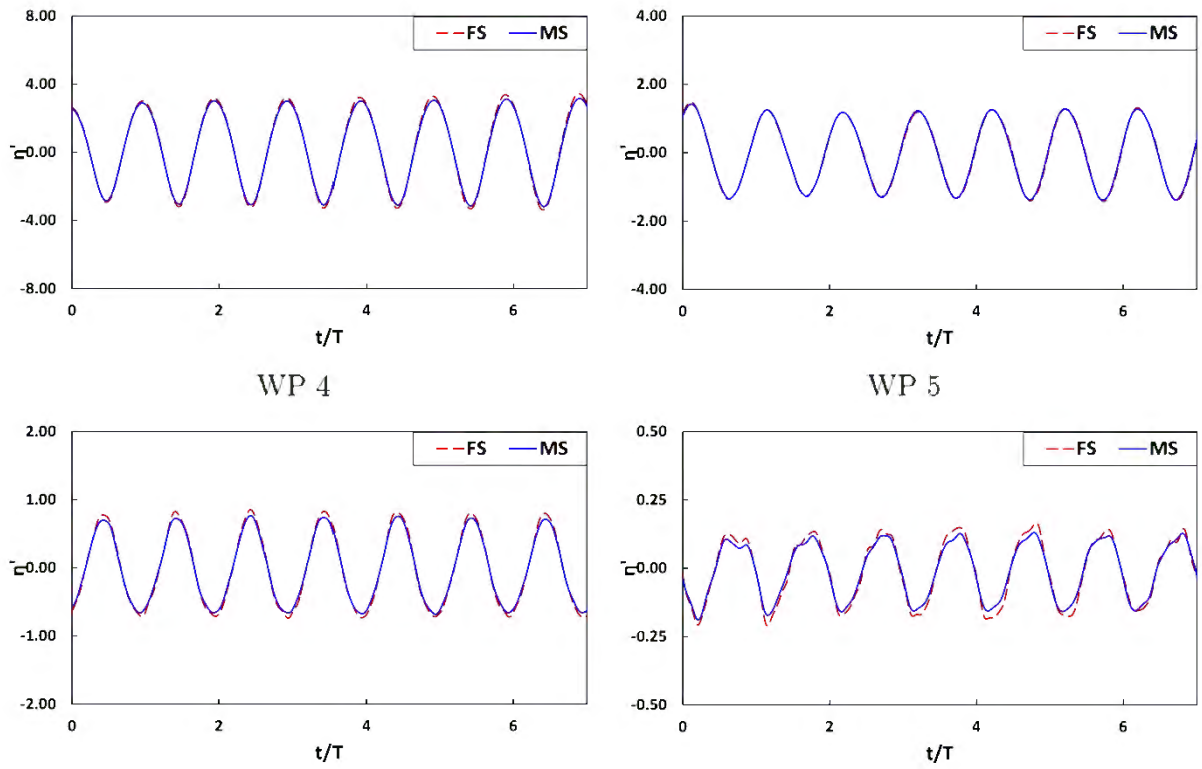

Figure 6.18 Comparison of model and full scale non-dimensional gap wave elevations for the lateral separation of ΔS=100 mm (MS)/ ΔS=10 m (FS) at wave frequency of 1.06 Hz (MS)/ 0.106 Hz (FS)

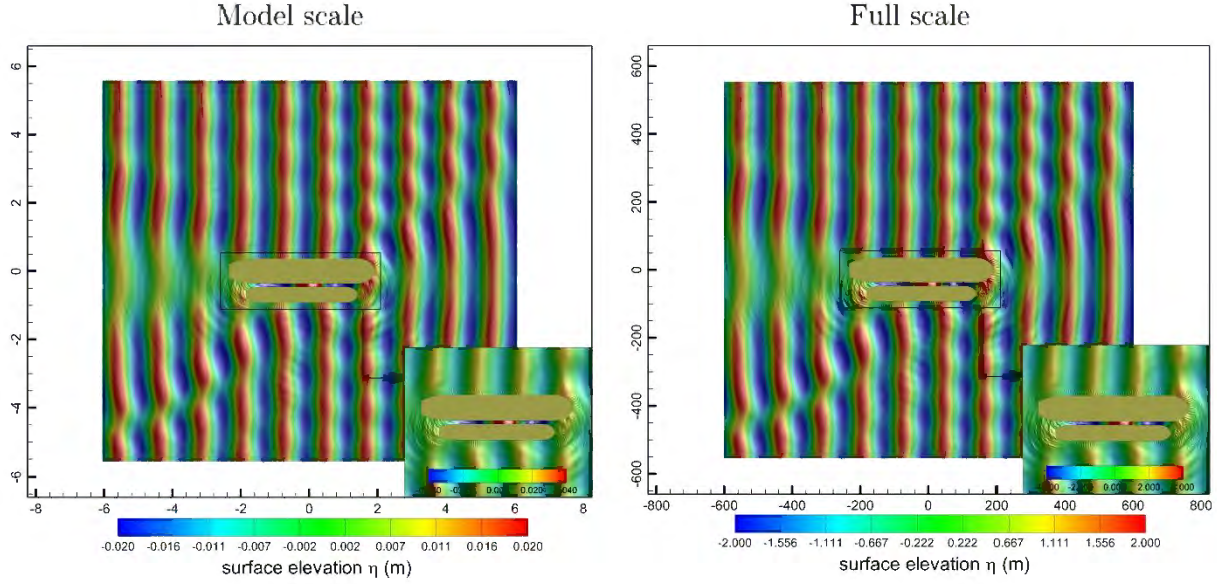

f=1.06 Hz f= 0.106 Hz

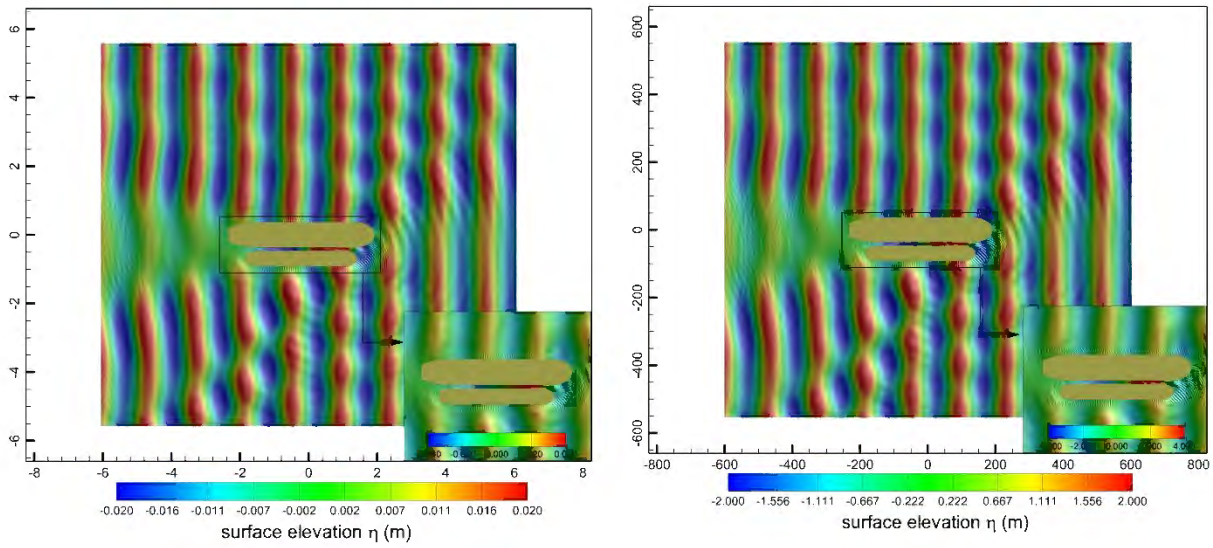

f=1.15 Hz f= 0.115 Hz

Figure 6.19 Comparison of model and full scale wave diffraction for the lateral separation of ΔS=100 mm (MS)/ ΔS=10 m (FS) after 15 encountered wave periods

6.6 Concluding remarks

The hydrodynamic interactions of a conceptual FLNG-LNG offloading system has been investigated using viscous URANS solver Star-CCM+. The computations are carried out with 6 DOF motions of the ship being fixed. Predictions on the wave loads as well as gap wave responses are carried out and compared with that from the physical model scale experiments and inviscid potential flow solver AQWA. A verification and validation study is performed based on a chosen wave case to demonstrate the credibility of the computational setup.

Based on the validated URANS model, a systematic investigation is conducted for analysing the influences of wave frequency and lateral separation between the FLNG and LNG on the hydrodynamic interactions. Furthermore, full scale computations are presented to demonstrate scale effects involved in the FLNG-LNG hydrodynamic interactions. From the computational results, the following conclusions can be drawn:

- There is a good correspondence between the experimental and URANS computed gap wave responses and wave loads for the investigated conditions, demonstrating the credibility of URANS approach for studying ship-ship interactions in waves.

- Viscous URANS computations provide more accurate predictions on the gap wave responses over the PF method at relatively high wave frequency conditions when the lateral separation between two ships is relatively small (ΔS=100 mm and 200 mm). With greater lateral separation (ΔS=300 mm), the PF calculations are proven to have similar level of accuracy.

- The PF method is still valid and recommended for predicting the wave loads when the incident wave frequency is relatively low and away from the natural frequency of the gap fluid considering its rapid computational time. The accuracy of the PF method improves as the lateral separation increases.

- Gap wave resonance is observed when the incident wave frequency approaches the natural frequency of the fluid in the gap between the FLNG and LNG vessels. This also leads to significant variation of wave loads in the directions of surge, sway, heave, pitch and yaw.

- Changing the lateral separation can strongly affect the ship-ship hydrodynamic interactions. Reduction in the lateral separation between the FLNG and LNG brings greater exaggeration of gap wave responses and shifts the occurrence of gap wave resonance to a higher frequency region.

- The variation of lateral separation poses similar effects on the wave loads in the directions of sway, heave, pitch and yaw. When reducing the lateral separation between the FLNG and LNG, occurrence of peak wave load transfer functions of greater significance shifts to a higher frequency region.

- The model and full scale URANS computations correlate well in aspects of wave loads, gap wave responses and wave diffractions around the FLNG-LNG system, which implies the minor influence of scale effects for the tested wave cases.

In summary, this chapter tests the feasibility of viscous URANS method for investigating ship-ship interactions in regular waves. Comparisons are made with EFD and inviscid PF calculations for the demonstration of numerical accuracy. Although the URANS method can be much more computational expensive shown in **Table** 6.9, it provides more accurate predictions on wave frequency loads at gap wave resonated conditions.

Table 6.9 Computational cost of URANS and PF computations

Method	Processor	Number of CPUs	Run time
URANS	Intel Xeon Phi KNL	130	Approx. 72 hrs (per wave frequency
PF	Intel Xeon E5-2620 v3	6	Approx. 4 hrs

Suggestions are also provided for the applicability of PF method when there are no experimental data available to tune a damping lid. However, the topic of ship-ship interactions requires further investigations since the current study has limitations subject to negligence of

the ship motion related wave radiation and the mechanical coupling with stationkeeping system.

Chapter 7 - Global Performance of an Integrated FLNG-LNG Offloading System

In this chapter, numerical analysis on the global performance of a FLNG-LNG offloading system is carried out using commercial potential flow solver AQWA, validations are presented for the computed second order wave drift forces. The results are compared against experimental data and those gathered from Pinkster (1979) and Molin et al. (2009). After demonstrating the credibility of the numerical model, time domain analysis coupled with hawsers, fenders and moorings is performed for a given environmental condition. Furthermore, the effects of varying hawser pretension and stiffness on the hydrodynamic performance of the FLNG-LNG system and the loads of the connection system are investigated. This chapter aims to provide an overview on the global hydrodynamic performance of an integrated FLNG-LNG offloading system. Though AQWA predictions on the first order wave loads can be inaccurate at certainty wave frequency conditions as shown in Chapter 6, its adverse influence on the global motion performance predictions are neglected here. A future study of using URANS computed wave frequency loads as an input into the PF time-domain analysis is proposed in Chapter 8.2.

7.1 Description of the FLNG-LNG system

7.1.1 Turret mooring system

The FLNG-LNG system is modelled to be located in a water depth of 300 m and moored by a turret mooring system consisting of 12 mooring lines. The centre of the turret is located at 90m aft from the bow and it allows the FLNG hull to weathervane freely under different environmental load conditions. The mooring lines had three segments arranged as chain-wire-chain and are spread with a horizontal span of 500 m. The pre-tension acting on top of each mooring line was 1064.7 kN; details of the mooring configuration are listed in Table 7.1.

Table 7.1 Configuration of the mooring lines in the FLNG system

Segment	Length	Diameter	Submerged mass	Axial stiffness	Min breaking load
	(m)	(mm)	(kg/m)	(kN/m)	(kN)
Chain	150	127	280.9	1629000	14971
Ploycster	100	233	7.9	59175	15696
Chain	400	127	280.9	1629000	14971

7.1.2 FLNG-LNG side-by-side arrangement

The conceptual FLNG-LNG offloading system is connected in a side-by-side arrangement by 8 spring hawsers and 4 fenders as presented in Figure 7.1. The axial stiffness of each hawser is set to be 83.7 kN/m with a safe working load (SWL) of 796.9 kN, 55 % of minimum breaking load (MBL) of 1449.0 kN. The hawsers are pre-tensioned by 250.0 kN in the base case. The axial stiffness of each fender is set to be 1785.9 kN/m. Reference of the mooring line and hawser properties can be made to OrcaFlex (2006) The positions of the hawsers and fenders with respect to the CoG of the FLNG are listed in Table 3.

Table 7.2 Relative positions of the hawser and fender connections in global coordinates

	Connection on the FLNG		Connection on the LNG	
	Longitudinal (m)	Lateral (m)	Longitudinal (m)	Lateral (m)
Hawser 1	125	36.4	110	46.4
Hawser 2	105	36.4	90	46.4
Hawser 3	85	36.4	70	46.4
Hawser 4	-10	36.4	25	46.4
Hawser 5	-30	36.4	-65	46.4
Hawser 6	-125	36.4	-110	46.4
Hawser 7	-145	36.4	-130	46.4
Hawser 8	-165	36.4	-150	46.4
Fender 1	100	36.4	100	46.4
Fender 2	25	36.4	25	46.4
Fender 3	-70	36.4	-70	46.4
Fender 4	-145	36.4	-145	46.4

7.1.3 Environmental conditions

In this study, the conceptual FLNG system is designed to be located in the coast of Western Australia. The random sea waves are described by the JONSWAP spectrum with a significant

wave height of 2.5 m. The peak period of the wave spectrum is 10.0 s and the enhancement factor is given to be 3.0. The current velocity near free surface is 1.0 m/s. The mean velocity of the wind at the reference height of 10 m is assumed to be 13.0 m/s (Zhao et al., 2014). During the numerical simulations, the heading of wind, wave and current approaching the FLNG system is set to be 180°.

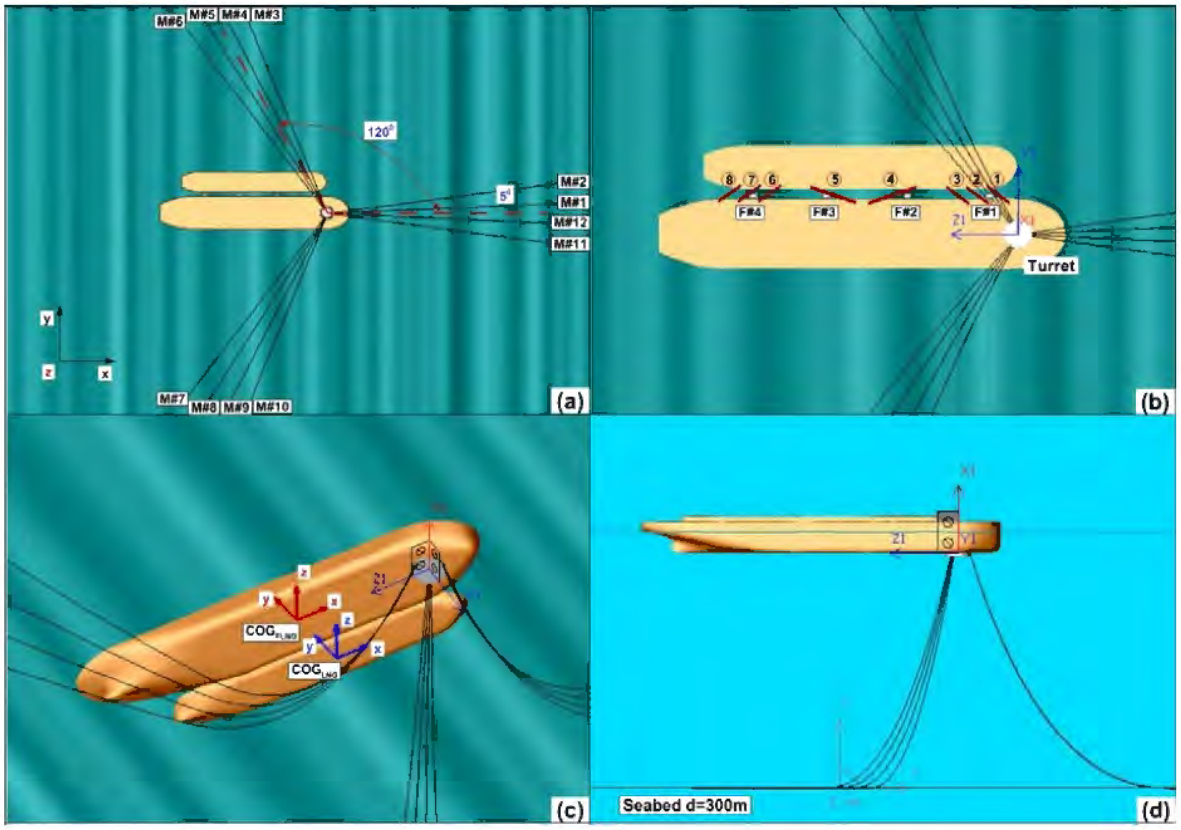

Figure 7.1 The side-by-side arrangement for the FLNG-LNG offloading system (a) plan view of the turret mooring (b) hawser and fender system (c) articulation modelling of internal turret (d) overview of operational depth

7.2 Frequency domain wave loads validation

7.2.1 Experimental study

Experimental validations of the first order wave loads on the FLNG-LNG offloading system are presented in this section. The models were constrained to enable the wave loads to be measured. The tested cases are listed in Table 7.3. Measurements of the FLNG-LNG motion responses coupled with mooring lines, hawsers and fender systems were not performed.

Table 7.3 Matrix of model test cases

	Degrees of freedom	Wave encountering angle μ	Wave frequency (Hz)
FLNG	Fixed in 6 DoF	180° (head sea)	0.63 0.70 0.75 0.81 0.89 0.99 1.06 1.15
LNG			

Wave probes were placed between the two vessels for measuring the gap wave elevations at different incoming wave conditions. The positions of probes relative to the LCG of the FLNG are given in Table 7.4. In order to obtain accurate wave elevation measurements, wave probes were calibrated on daily basis before testing. For the load cells, calibrations were performed at the beginning and at the end of the testing program.

Table 7.4 Positons of the wave probes relative to the LCG of the FLNG parallel to the x-axis

Wave probe	1	2	3	4	5	6	7	8	9	10
Position (m)	2.39	1.59	0.99	0.59	-0.02	-0.41	-1.01	-1.41	-2.01	-2.83

7.2.2 Wave frequency load transfer functions

The first order wave frequency load transfer functions are computed in full scale at water depth draft ratio d/T_{FLNG}=3.3. The experimental measurements are converted to full scale by Froude scaling. As shown in Figure 7.2, it can be seen that the simulation results correlate well with experimental data in the frequency range of 0.06 - 0.12 Hz. The general trend of the predicted wave force transfer functions is smooth when the wave frequency is below 0.90 Hz. As the frequency increases, fluctuations appear in the results. The FLNG and LNG experience upsurging of wave load in directions of sway, heave and yaw at high wave frequency conditions. A possible explanation of this phenomenon could be severe gap wave responses around these particular wave frequencies.

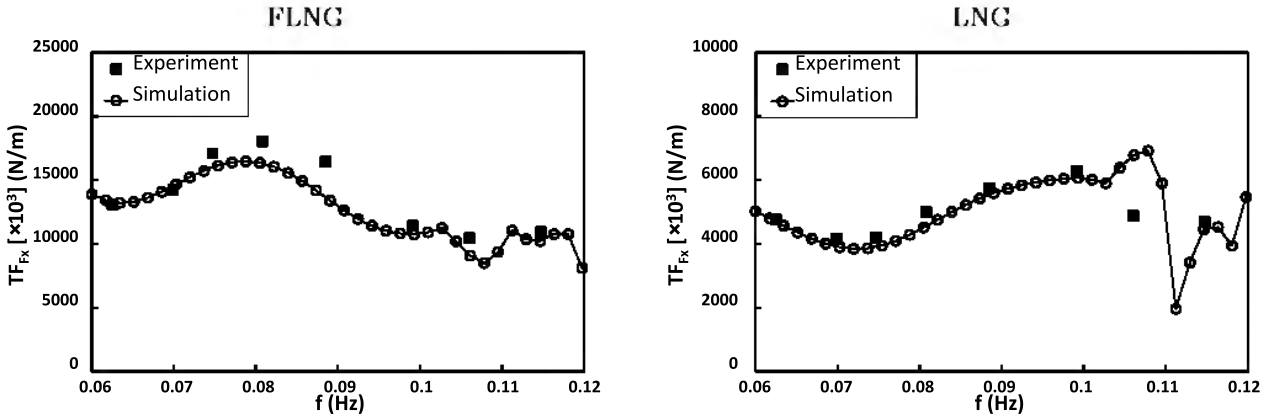

(a) (b)

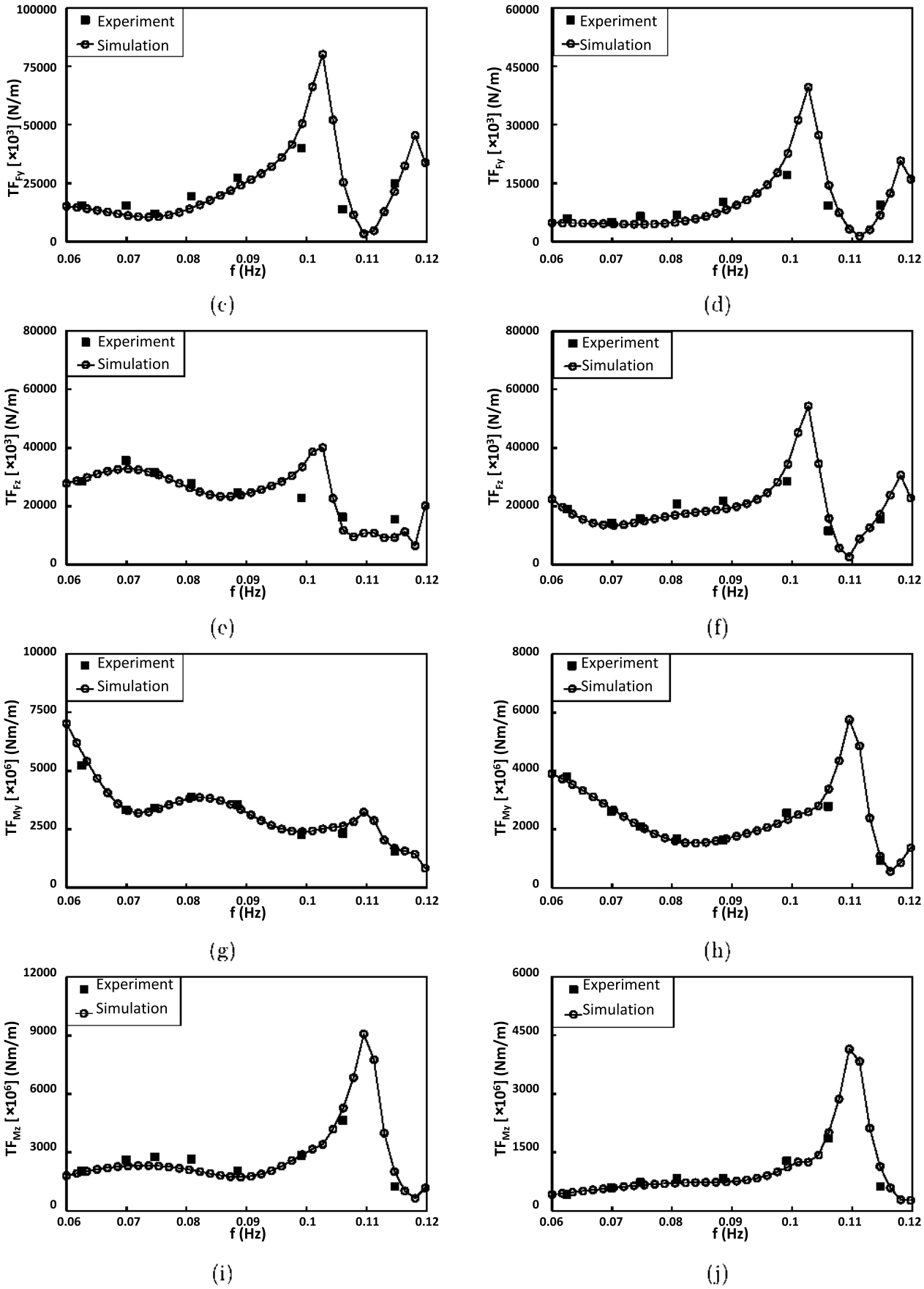

Figure 7.2 Wave force transfer functions on the FLNG and LNG hulls during offloading

7.2.3 Gap wave excitation

Comparisons are made between the experimental and simulation results on the non-dimensional gap wave height (H_G') for the investigated frequencies as shown in Figure 7.3. The non-dimensional gap wave height represents the ratio between the gap wave height (H_G) and incident wave height (H_O). The behaviour of gap waves exhibits great similarities for the conditions when the incident wave frequency is below 0.099 Hz, though there are discrepancies in the magnitude of H_G' at certain positions. For positions in the range of -300 - 0.0 m, the gap waves are suppressed to about half of the incident wave amplitude for the low frequency cases (0.063 - 0.089 Hz). Conversely, the tendency of H_G' varies significantly for high wave frequency conditions (0.106 Hz and 0.115 Hz). Meanwhile, it is found that the amplitude of the gap waves at these frequencies are enlarged to 2 - 3 times of the incident wave amplitude. This observation can be regarded as an explanation of the peaks existing in the wave force transfer functions as discussed previously. The amplified gap waves can induce highly asymmetric pressure distribution on the hulls of the FLNG and LNG vessel, therefore results in much larger net forces and motion responses. This can have a significant impact on the FLNG-LNG system during side-by-side offloading operations.

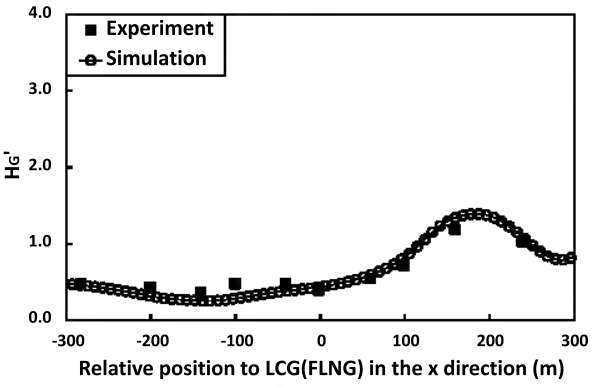

f = 0.063 Hz

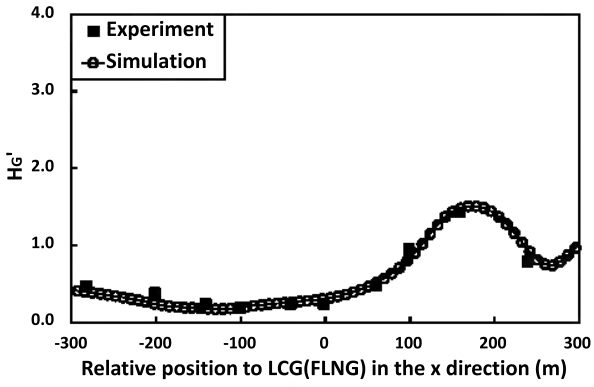

f = 0.070 Hz

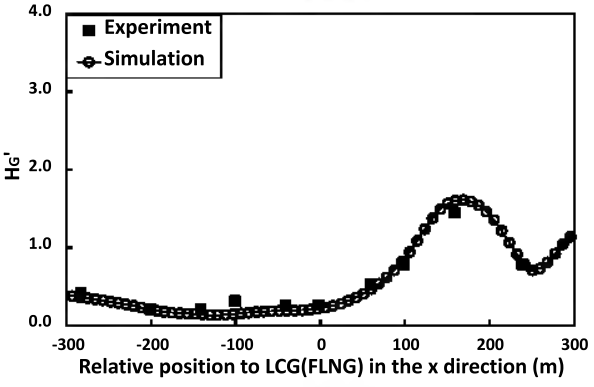

f = 0.075 Hz

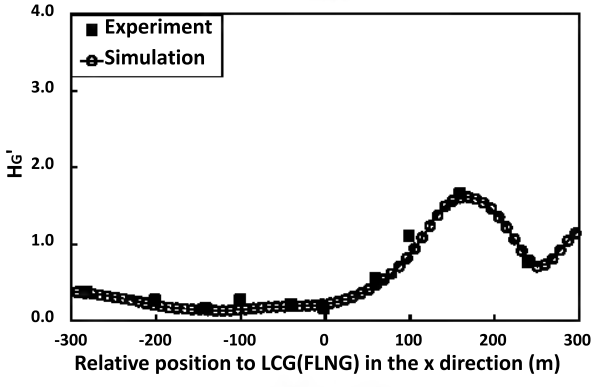

f = 0.081 Hz

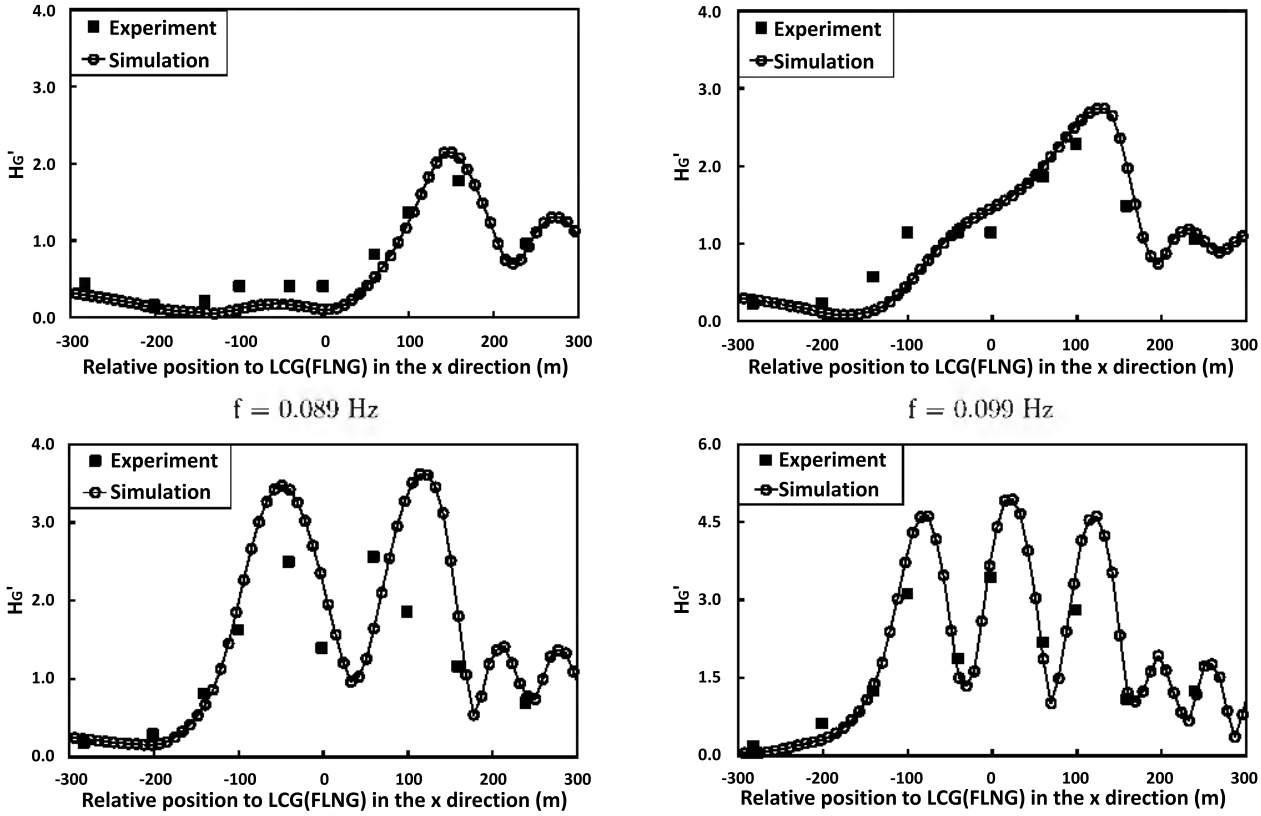

Figure 7.3 Comparison of experimental and numerical predictions on the non-dimensional gap wave elevation in full scale

7.2.4 Mean and low frequency wave drift load validation

In order to validate the calculation of second order wave excitation forces in AQWA, a few selected cases are replicated and the computed QTFs are compared with published experimental and numerical results. It is worth mentioning here that the mean wave drift forces correspond to the diagonal terms in a QTF matrix while the low frequency wave drift forces are related to the off-diagonal components of the difference QTF. The main physical particulars of the investigated structures and their corresponding test conditions are listed in Table 7.5.

Table 7.5 Validation cases for the second order wave excitation force computations in AQWA

Case	Barge (Pinkster, 1979)	Semi-Submersible (Pinkster, 1979)	Identical Barges Side-by-Side (Molin et al., 2009)
Scale	Full Scale	Full Scale	Model Scale
L_{pp} (m)	150	100	2.47
B (m)	50	76	0.60
T (m)	10	20	0.18
d (m)	50	40	3.00
μ(deg)	-180 (head sea)	-180 (head sea)	-180 (head sea)
Separation (m)	~	~	0.12

The mean wave drift force in the surge direction for the single barge and semi-submersible cases are presented in Figures 7.4(a) and (b). The results have been made non-dimensional using the incident wave height and the length of the structures. One can observe there is a good correspondence between AQWA predictions and the results gathered from literatures. For the case of side-by-side barges, the mean wave drift forces in the sway direction are shown in Figure 7.4(c). The results correlate very well with numerical predictions in (Molin et al., 2009). The force is repulsive on either hull, and attains quite large magnitude.

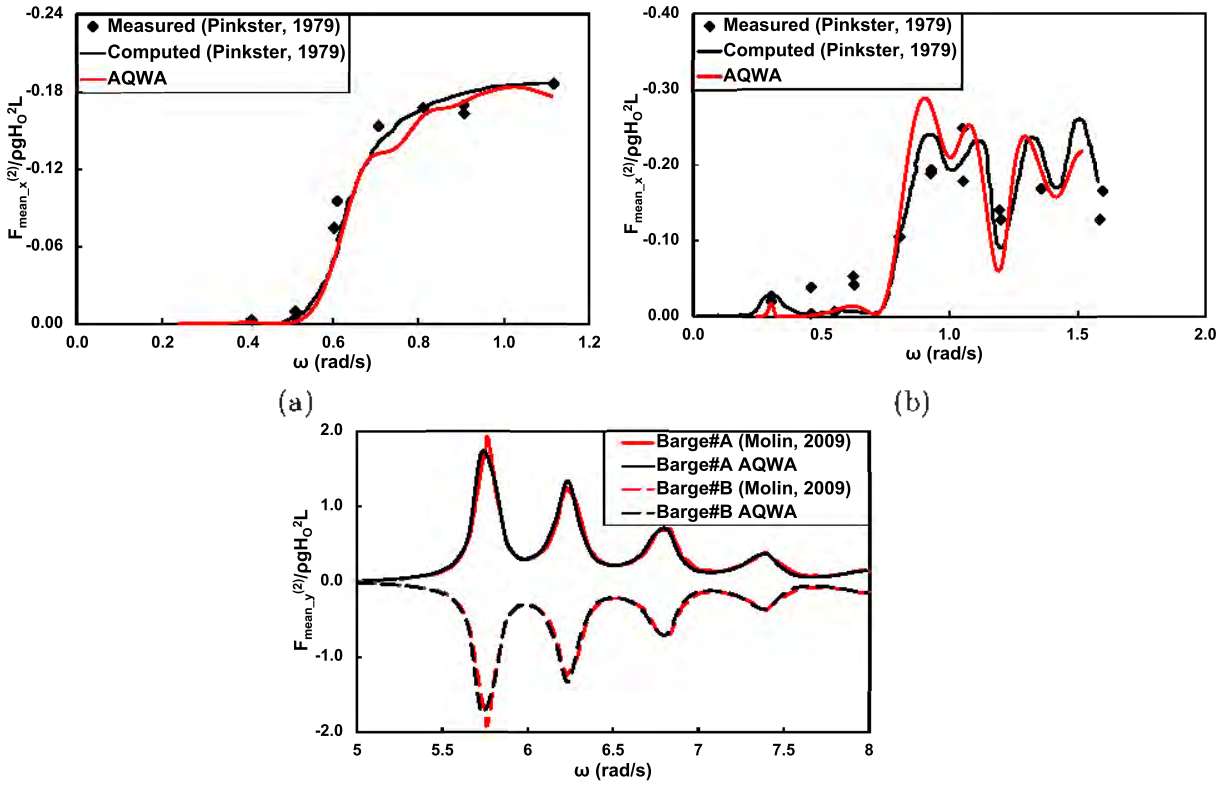

Figure 7.4 Comparisons of mean wave drift force from AQWA and literatures on (a) barge, (b) semi-submersible and (c) side-by-side barges

To exam the computation of low frequency wave drift force, comparison is made between the surge QTF matrix off-diagonal components of the semi-submersible from AQWA and (Pinkster, 1979) in Table 7.6. The results have been non-dimensionalised as Figure 7.4, where the averaged difference between the two series data is around 25%.

Table 7.6 Comparison of computed surge QTF matrix for the semi-submersible

(Pinkster, 1979)	ω1 (rad/s)	0.5	0.6	0.7	0.8	0.9	1.0	1.1
ω2 (rad/s)								
0.5		0.00	0.08	0.11	0.07	0.08	0.20	0.15
0.6			0.01	0.06	0.07	0.05	0.14	0.19
0.7				0.00	0.07	0.15	0.03	0.18
0.8					0.11	0.23	0.20	0.13
0.9						0.25	0.21	0.09
1.0							0.20	0.21
1.1								0.24
AQWA	**ω1 (rad/s)**	**0.5**	**0.6**	**0.7**	**0.8**	**0.9**	**1.0**	**1.1**
ω2 (rad/s)								
0.5		0.00	0.07	0.10	0.04	0.06	0.20	0.11
0.6			0.01	0.05	0.04	0.06	0.11	0.11
0.7				0.00	0.06	0.12	0.13	0.10
0.8					0.12	0.23	0.25	0.08
0.9						0.29	0.24	0.11
1.0							0.21	0.20
1.1								0.24

7.3 Global performance of the FLNG-LNG offloading system

In the previous section, the credibility of AQWA predictions on the first order wave frequency and second order wave drift loads has been demonstrated. Based on results from analogous numerical modelling, time domain analyses are performed for the FLNG-LNG facility at a water depth of 300 m (d/T_{FLNG}=12.5) coupled with turret mooring, hawser and fender systems in full scale.

7.3.1 Motions of side-by-side FLNG-LNG system

Time history predictions on the motion responses of the FLNG and LNG in a side-by-side configuration are presented in Figure 7.5. It can be observed that both the FLNG and LNG hulls experienced long periodic motions, especially in surge, sway and roll. This corresponds

well with the findings presented in Zhao et al. (2014), except the period of those low frequency motions. The primary reason of this is due to the difference in the length of mooring chains utilised in the designs, which resulted in different pretensions at the turret mooring top end connections. One can also observe that the heave, roll and pitch motions of the FLNG and LNG are frequency dominated and the LNG vessel experience severer heave, roll and pitch motion responses than the FLNG hull. This is partially due to the fact the displacement of the LNG vessel is much less than that of the FLNG hull.

The statics of the 6 DoF motion responses of the FLNG and LNG under the given environmental condition are presented in Table 7.7. It is observed that the peak to peak (P-P) surge motion of the FLNG is 6.50 m, which is significantly smaller than that of the LNG vessel (10.77 m). The P-P sway motions of the FLNG and LNG are observed to be 8.02 m and 11.79 m respectively. The yaw motions of the FLNG and LNG show similar long periodical behaviour as that of the surge and sway motions, and the P-P responses are 3.32 deg and 4.35 deg respectively. The P-P amplitudes of other motions including heave, roll and pitch are relatively small compared to that of the surge, sway and yaw motions.

The long periodical surge and sway motions of the FLNG offloading system are further studied in this section as they are the dominant motions. First, the trajectories of the FLNG and LNG in the horizontal plane are presented individually in Figure 7.6. To investigate the operability of LNG offloading, the relative surge and sway motions between the CoGs of the FLNG and LNG vessel are shown in Figure 7.7. It is found both of the relative surge and sway motions exhibit long periodical nature. Figure 7.8 gives the trace plot of these two relative motions in the horizontal plane. It is seen that the relative motion between the two CoGs varies between -3.25 - 1.83 m in the x direction and -4.17 - 1.98 m in the y direction. This gives a good indication of the operational limit for the cryogenic hose during offloading in respect of displacement.

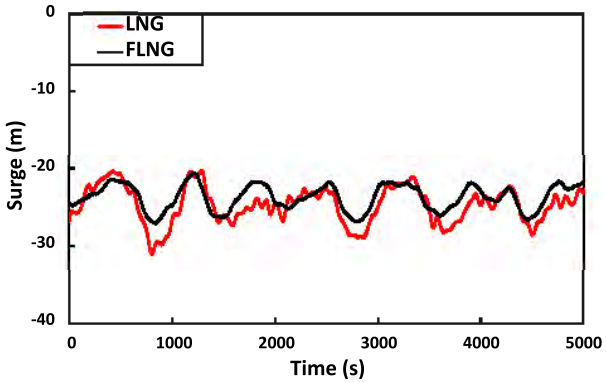

(a)

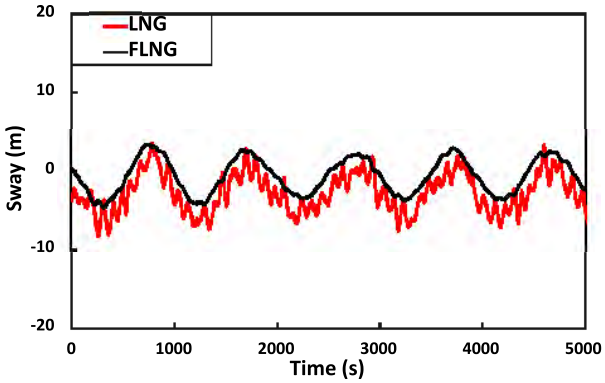

(b)

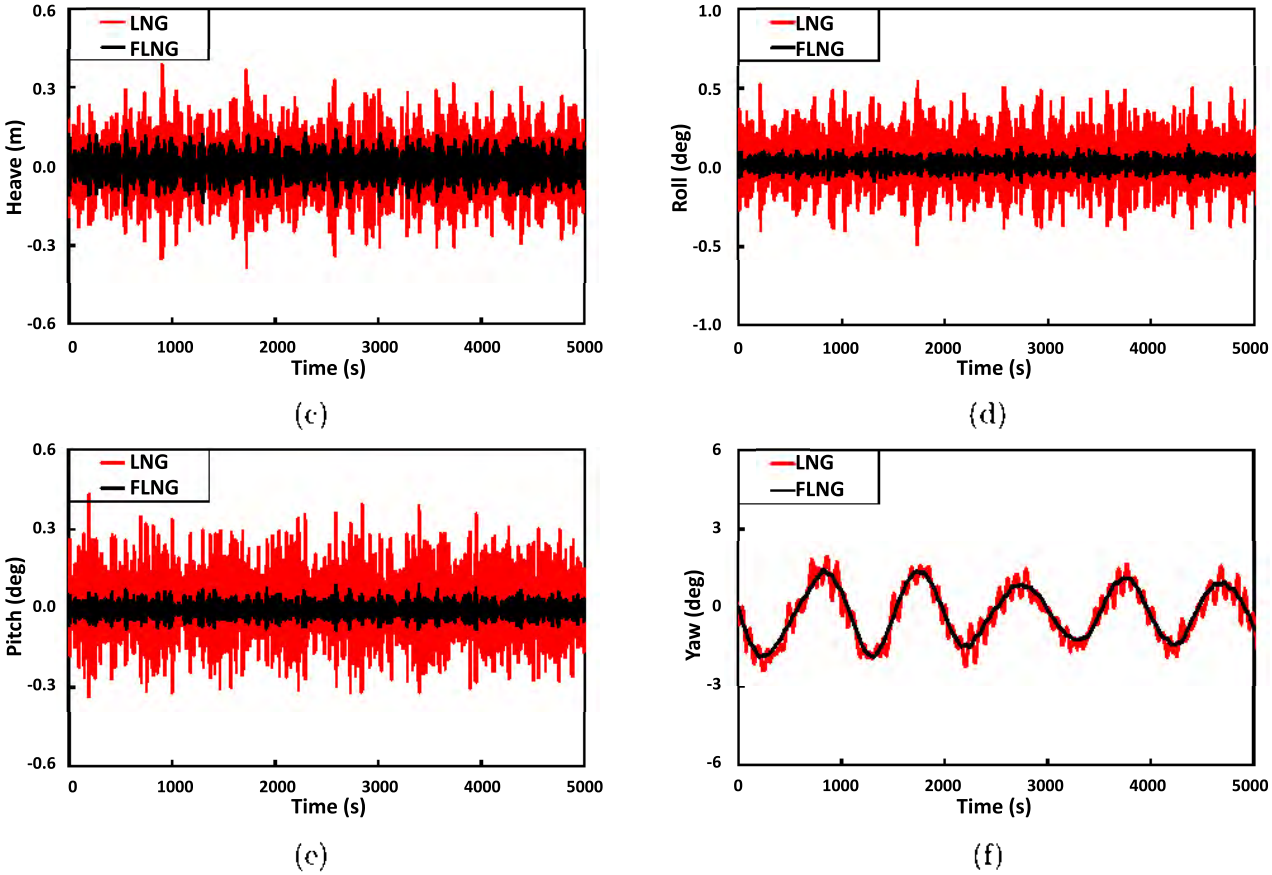

Figure 7.5 Time series of the FLNG and LNG 6 DoF motion responses

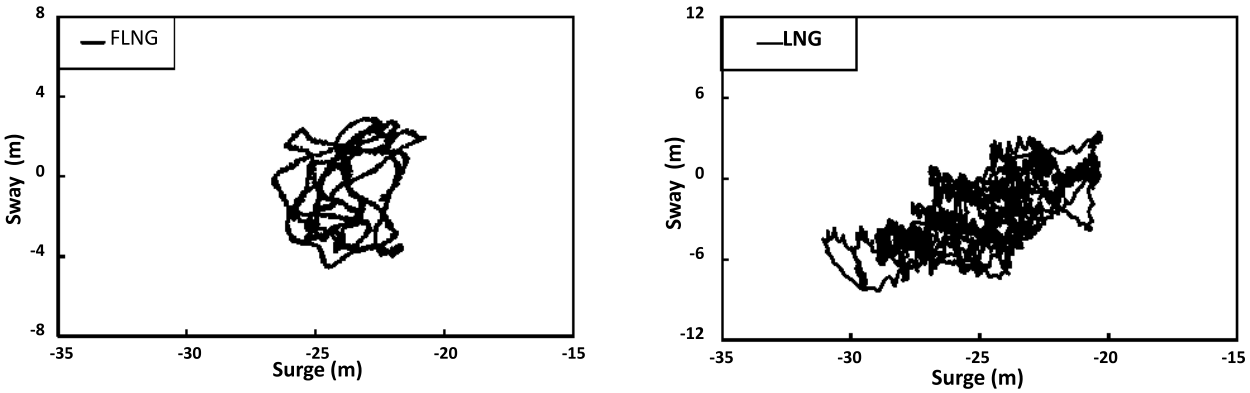

Figure 7.6 Trace plot of the FLNG and LNG in the horizontal plane

Table 7.7 Quantitative summary of FLNG and LNG motion responses

		Max	Min	P-P	Mean	STD
Surge (m)	FLNG	-20.59	-27.09	6.50	-23.73	1.62
	LNG	-20.30	-31.07	10.77	-24.73	2.34
Sway (m)	FLNG	3.30	-4.72	8.02	-0.67	2.21
	LNG	3.44	-8.35	11.79	-2.76	2.44
Heave (m)	FLNG	0.14	-0.15	0.29	0.00	0.05
	LNG	0.38	-0.38	0.77	0.00	0.10
Roll (deg)	FLNG	0.14	-0.09	0.23	0.02	0.03
	LNG	0.54	-0.48	1.02	0.05	0.15
Pitch (deg)	FLNG	0.09	-0.09	0.17	-0.01	0.03
	LNG	0.43	-0.34	0.77	0.01	0.11
Yaw (deg)	FLNG	1.45	-1.87	3.32	-0.17	0.94
	LNG	1.96	-2.39	4.35	-0.22	1.03

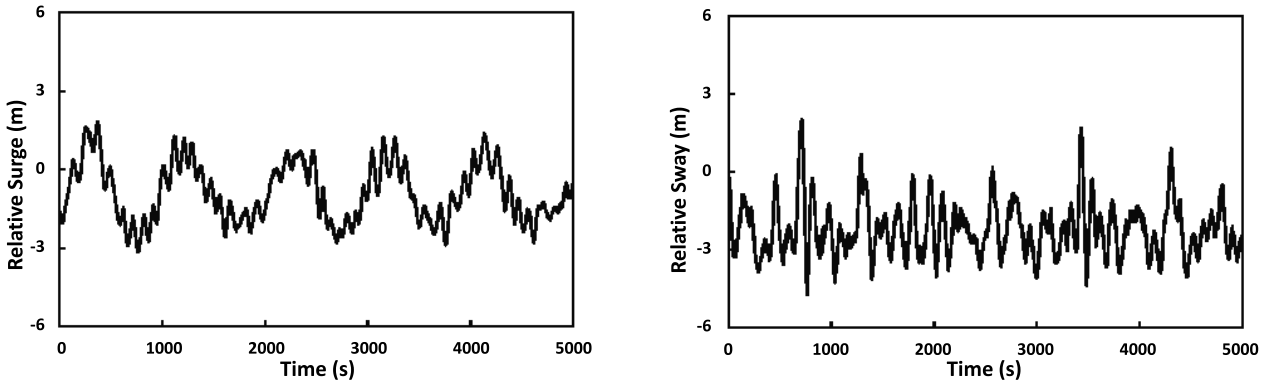

Figure 7.7 Time series of relative motions between the CoGs of the FLNG and LNG

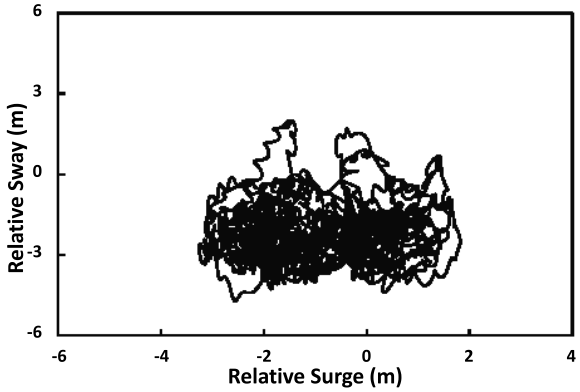

Figure 7.8 Trajectory of the relative motion between the CoGs of the FLNG and LNG in horizontal plane

7.3.2 Hawser, fender and mooring loads

Apart from motion responses of the FLNG offloading system, mechanical loads acting on the hawsers, fenders and mooring lines have also been analysed for the presented base case. Figure 7.9 shows the time history prediction of the force acting on a pre-tensioned hawser. It is observed that the variation of the predicted hawser load is closely related to the sway motion between the two vessels. As a result of excessive relative sway motion, collisions between the FLNG and LNG happen frequently through the fenders. Figure 7.10 depicts these collision forces in the form of impulsive loads on the time domain, from which it can also be found that the fenders in the bow of the vessels experienced more collisions than those located in the stern region.

The mooring loads acting on the top connection of the inner turret mooring system are presented in Figure 7.11. It is observed that the mooring lines were pre-tensioned by their self-weight and dominated by low frequency force component. One can also find that periods of the low frequency force on mooring lines 1 and 5 correspond well with the surge and sway motion (Figure 7.5) of the FLNG hull respectively. This is primarily due to the positional configuration of the investigated mooring system as given in Figure 7.1. Mooring line 1 was positioned at an angle of 2.5° off the global x-axis, therefore a large portion of the dynamic mooring load was induced by the environmental loads in the surge direction. Similarly, mooring line 5 was orientated to an angle close to the global y-axis, hence it was loaded mainly by the sway force resulting from the hydrodynamic interaction. Table 7.8 summarises the hawser, fender and mooring loads which are compared against their individual SWLs (OrcaFlex, 2006).

Table 7.8 Quantitative summary of hawser, fender and mooring loads

	Max (kN)	Min (kN)	Mean (kN)	STD (kN)	SWL (kN)
Hawser 5	406.98	121.36	273.04	43.54	797.0
Fender 1	2036.88	~	~	~	3000
Fender 4	1541.75	~	~	~	3000
Mooring 1	1351.71	1245.90	1296.79	20.20	8234
Mooring 5	1024.65	951.18	988.51	13.02	8234

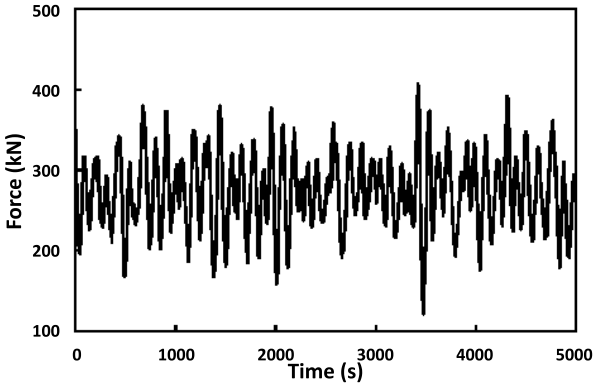

Figure 7.9 Time series of forces acting on hawser 5

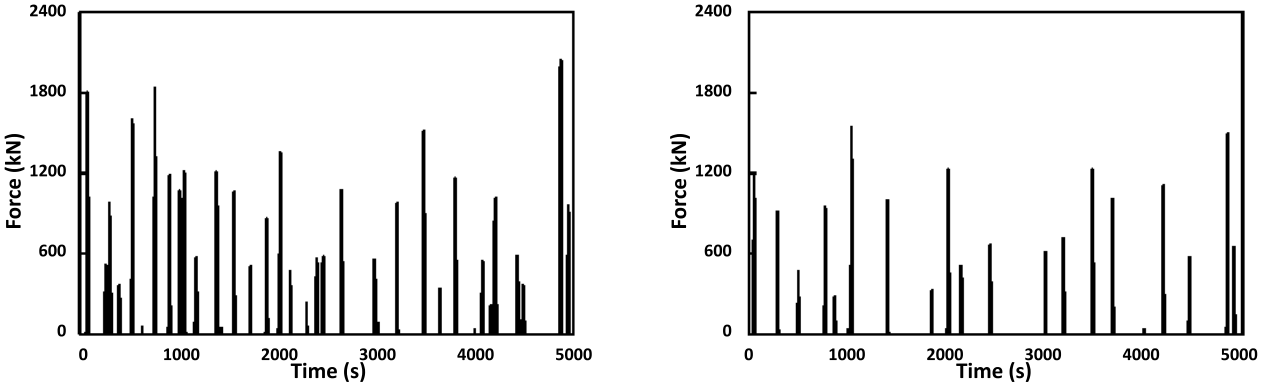

Figure 7.10 Time series of fender loads: (a) fender 1 and (b) fender 4

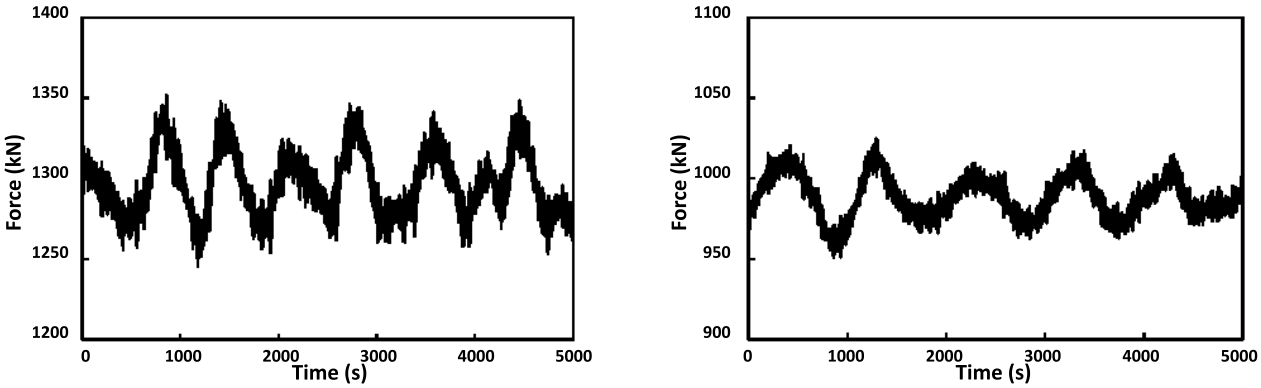

Figure 7.11 Time series of mooring loads at top connection of the inner turret mooring system (a) mooring line 1 and (b) mooring line 5

7.3.3 Effects of hawser pretension and stiffness

In this section, the influences of varying hawser pretension and stiffness are discussed through a series of parametric studies presented in Table 7.9. For each of these cases, the trajectory and relative motions of the FLNG and LNG as well as the hawser, fender and mooring line loads have been analysed.

Time history plots of the FLNG and LNG horizontal plane motion for different hawser pretension conditions are shown in Figure 7.12. One can observe that the LNG trajectory is more sensitive to the pretension forces compared to that of the FLNG. Again, this is partially due to the lower displacement of the LNG vessel.

A comparison of relative surge and sway motions between the FLNG and LNG vessels under different pretension conditions are shown in Figure 7.13. It can be seen that the relative motions decrease as the pretensions of the hawser increases. A quantitative summary of the relative motions is given in Table 7.10, the P-P relative surge motions are 6.65 m, 4.75 m and 3.85 m in Case 1, Case 2 and Case 3 respectively. The P-P relative sway motions are 7.57 m, 5.99 m and 4.37 m for the three studied cases. The standard deviations of the relative motions also decrease as pretension increases, which indicates that an increment of pretension would effectively inhibit the large fluctuations of the relative motions.

The trajectories of relative motions of the FLNG and LNG in the horizontal plane for varying pretensions are shown in Figure 7.14. Again, it demonstrates that the relative motions can be significantly reduced by pretensioning the hawser connections.

Table 7.9 Computational matrix of the parametric study

	Hawser Pretension (kN)	Hawser Stiffness (kN/m)
Case 1	0	83.57
Case 2	200	83.57
Case 3	400	83.57
Case 4	200	100.0
Case 5	200	75.0
Case 6	200	50.0
Base case	300	83.57

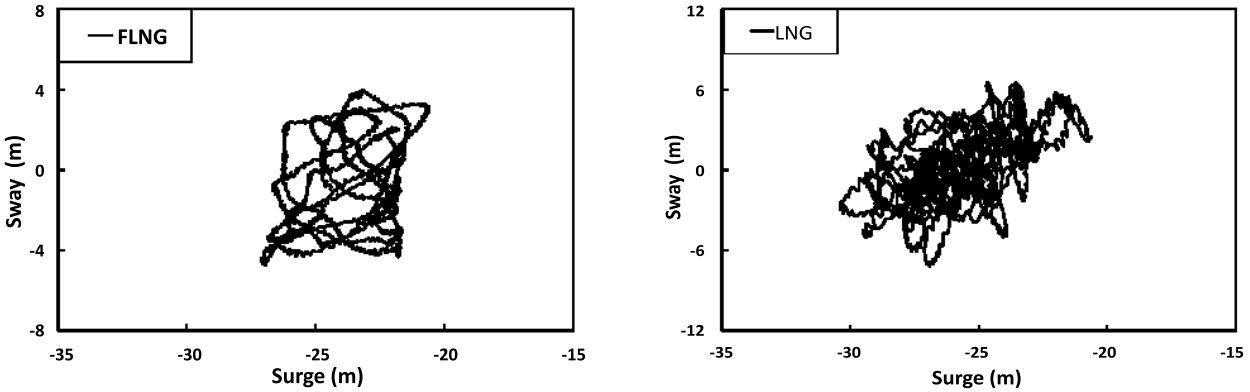

(a)

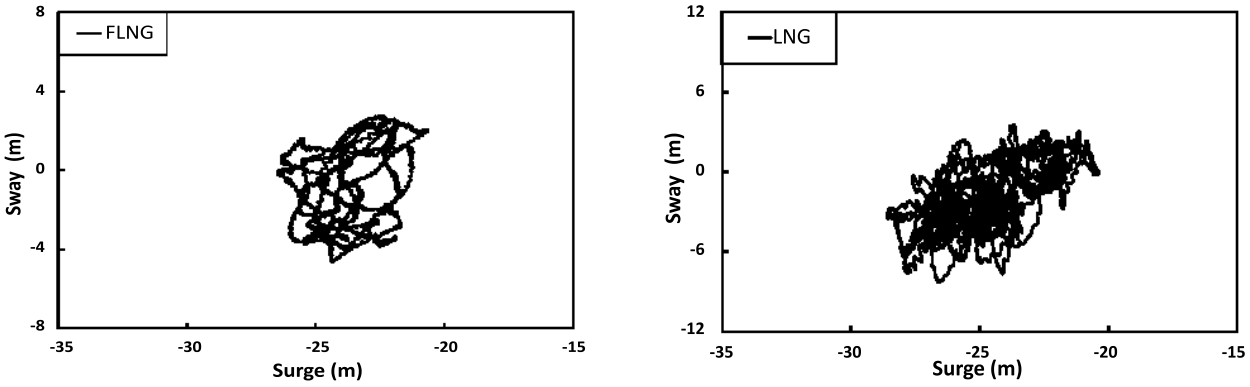

(b)

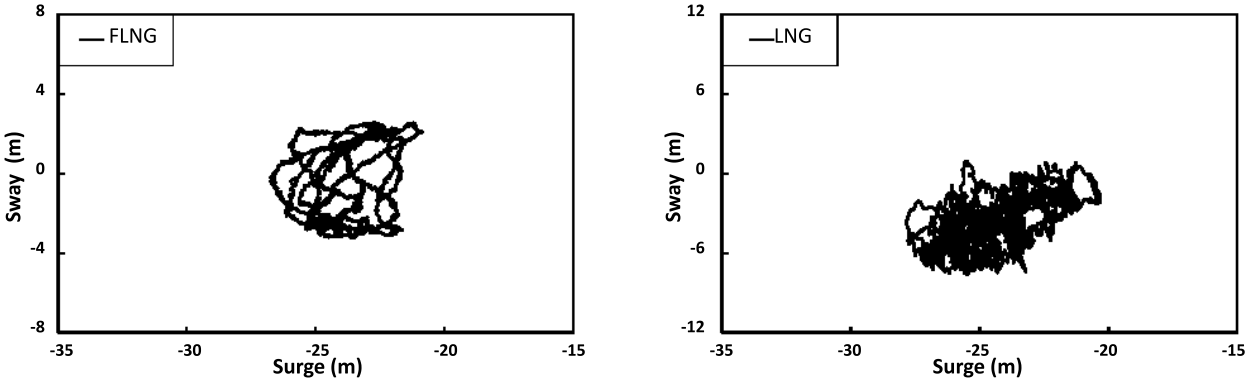

(c)

Figure 7.12 Horizontal plane motions of the FLNG and LNG at different hawser pretension conditions (a) case 1, (b) case 2 and (c) case 3

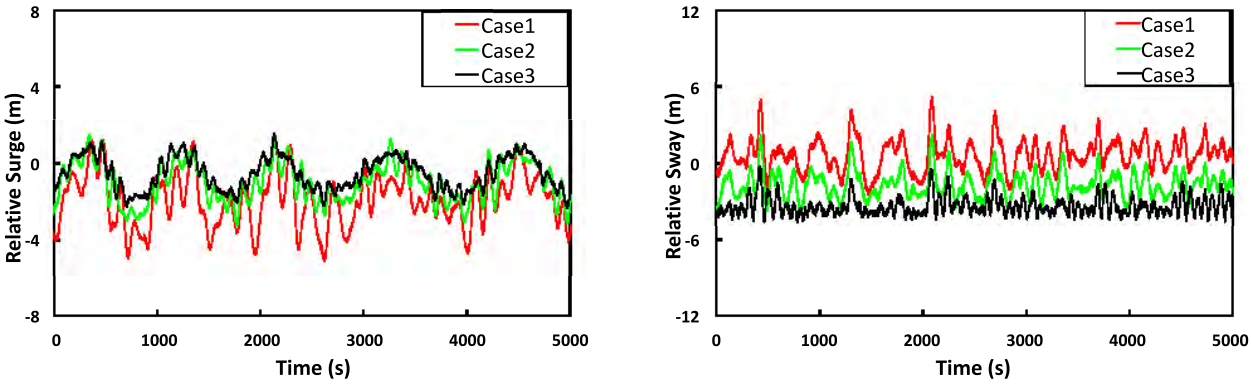

Figure 7.13 Relative motions between the FLNG and LNG at different hawser pretension conditions

Table 7.10 Quantitative summary of the relative motions at different pretention conditions

	Max	Min	P-P	Mean	STD
Relative surge (m)					
Case 1	1.57	-5.08	6.65	-1.91	1.40
Case 2	1.46	-3.28	4.75	-0.98	1.07
Case 3	1.54	-2.31	3.85	-0.53	0.87
Relative sway (m)					
Case 1	5.16	-2.41	7.57	0.69	1.25
Case 2	2.22	-3.77	5.99	-1.64	1.03
Case 3	-0.19	-4.56	4.37	-3.34	0.71

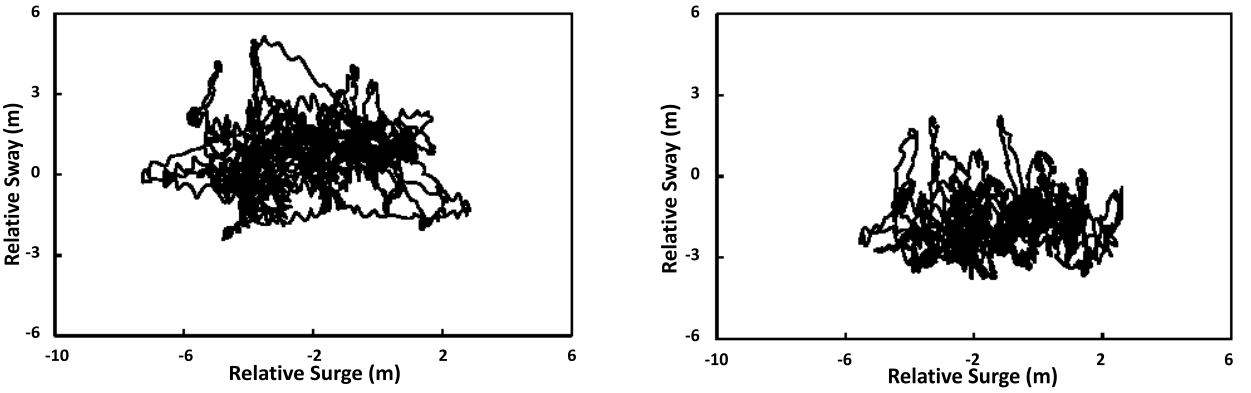

(a) (b)

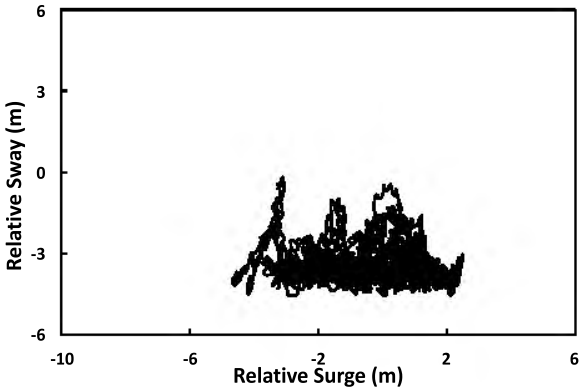

(c)

Figure 7.14 Trace plot of relative motions between FLNG and LNG in the horizontal plane at different hawser pretension conditions (a) case 1, (b) case 2 and (c) case 3

Time history predictions on hawser and fender loads for varying hawser pretensions are presented in Figure 7.15. It can be observed that fluctuations on the hawser loads have been reduced effectively by increasing hawser pretension. This correlates well with the decreasing trend of the standard deviation of the forces predicted on hawser 5 listed in Table 7.11. The maximum tensions on hawser 5 for the investigated varying pretension conditions exhibit insignificant difference in magnitude while the mean hawser tension decreases as the pretension is being reduced. As shown in Figure 7.15, the maximum forces acting on fender 4 increase when the hawser pretension has been increased, simultaneously the collision between the two vessels is more frequent.

The influence of hawser pretension on mooring forces seems to be minor as shown in Figure 7.16. The magnitude and period of the low frequency mooring forces for the investigated three pretension conditions and the base case are very close to each other and the mooring forces display as a combination of wave frequency and low frequency components as discussed in previous sections.

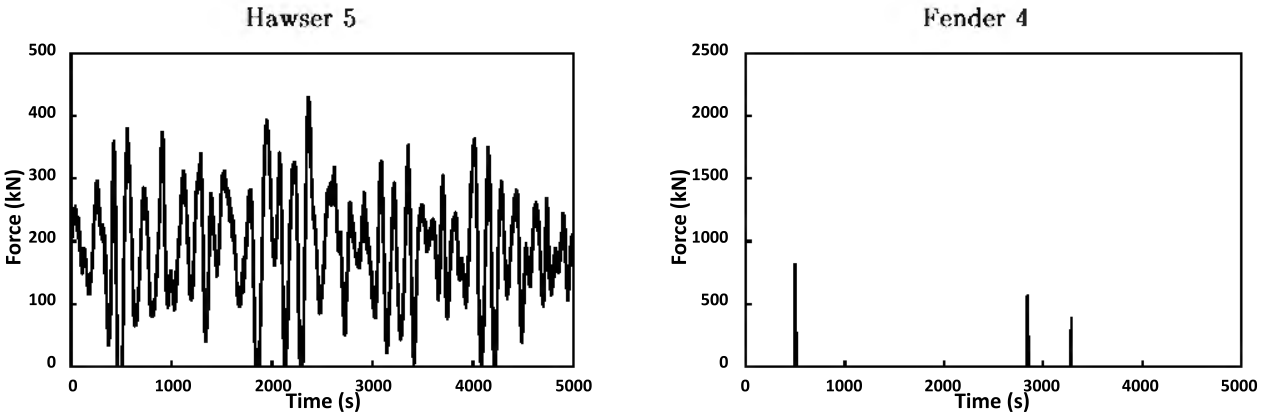

(a)

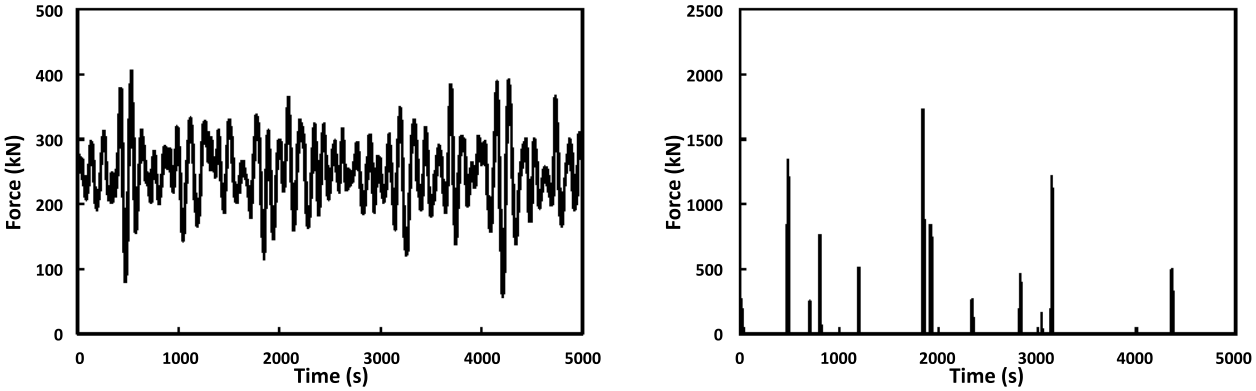

(b)

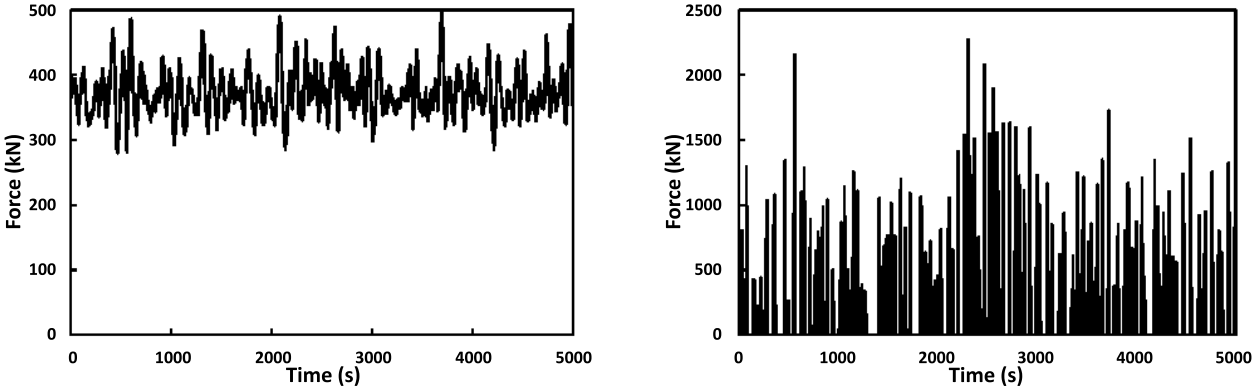

(c)

Figure 7.15 Time series of forces on hawser 3 and fender 4 at different hawser pretension conditions (a) case 1, (b) case 2 and (c) case 3

Table 7.11 Quantitative comparison of hawser and fender loads at different hawser pretension conditions

	Max	Min	Mean	STD
Hawser force (kN)				
Case 1	429.27	0.00	187.50	85.02
Case 2	404.83	57.24	248.44	50.47
Case 3	499.94	280.41	373.12	34.12
Fender force (kN)				
Case 1	812.78	~	~	~
Case 2	1725.84	~	~	~
Case 3	2270.91	~	~	~

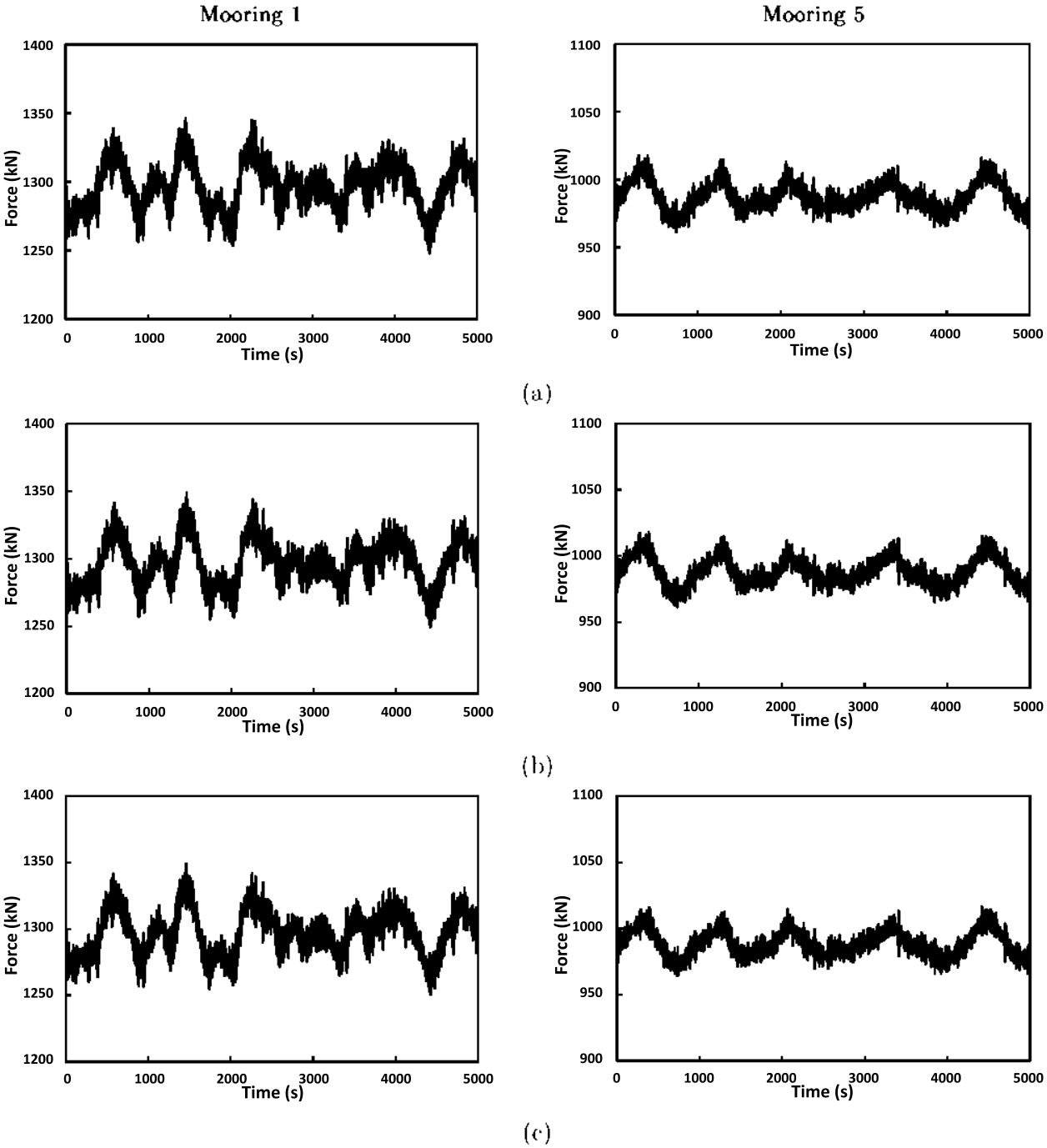

Figure 7.16 Time series of mooring forces at different hawser pretension conditions (a) case 1, (b) case 2 and (c) case 3

To investigate the influence of hawser stiffness, a comparison of relative surge and sway motions between the FLNG and LNG vessels are shown in Figure 7.17. It can be observed that the relative surge motion between the two vessels is less sensitive to the variation of hawser stiffness compared to the relative sway motion. Figure 7.18 presents the trajectories of the relative motions between the FLNG and LNG in the horizontal plane for the investigated three cases. One can observe that the variations are comparably less than that caused by altering

the hawser pretension as given previously in Figure 7.14. As summarised in Table 7.12, the P-P relative surge motions are found to be 4.63 m, 4.83 m and 5.20 m for Case 4, 5 and 6 respectively. The relative sway motion exhibits a more significant increment in its magnitude as the hawser stiffness is being reduced. The P-P relative sway motions are estimated to be 5.68 m, 6.16 m and 6.90 m for Case 4, 5 and 6 respectively. The standard deviation of the relative motions reveals the same trend. As the hawser stiffness being reduced, the fluctuations in the relative motions are enlarged.

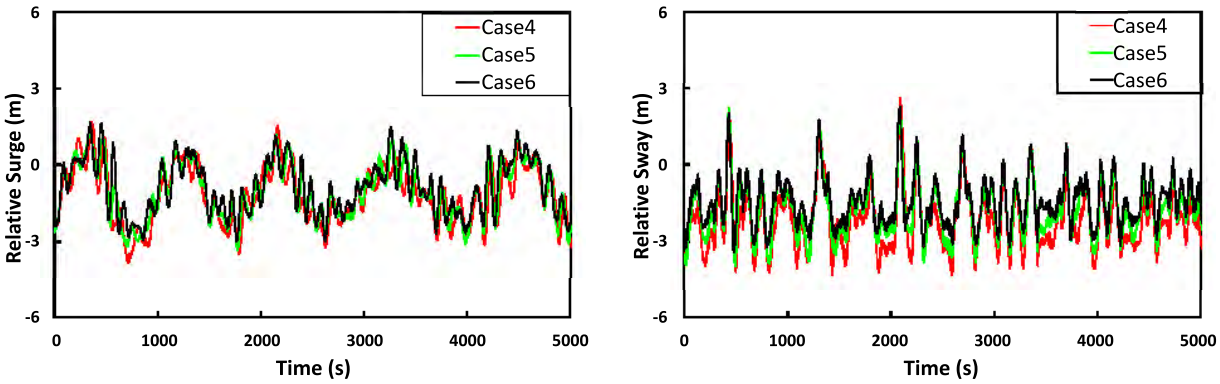

Figure 7.17 Relative motions between the FLNG and LNG at different hawser stiffness conditions

Table 7.12 Quantitative summary of the relative motions at different hawser stiffness conditions

	Max	Min	P-P	Mean	STD
Relative surge (m)					
Case 4	1.64	-2.99	4.63	-0.88	1.06
Case 5	1.29	-3.54	4.83	-1.03	1.08
Case 6	1.66	-3.32	5.20	-1.18	1.12
Relative sway (m)					
Case 4	2.26	-3.43	5.68	-1.44	0.94
Case 5	2.20	-3.96	6.16	-1.76	1.07
Case 6	2.58	-4.32	6.90	-2.19	1.14

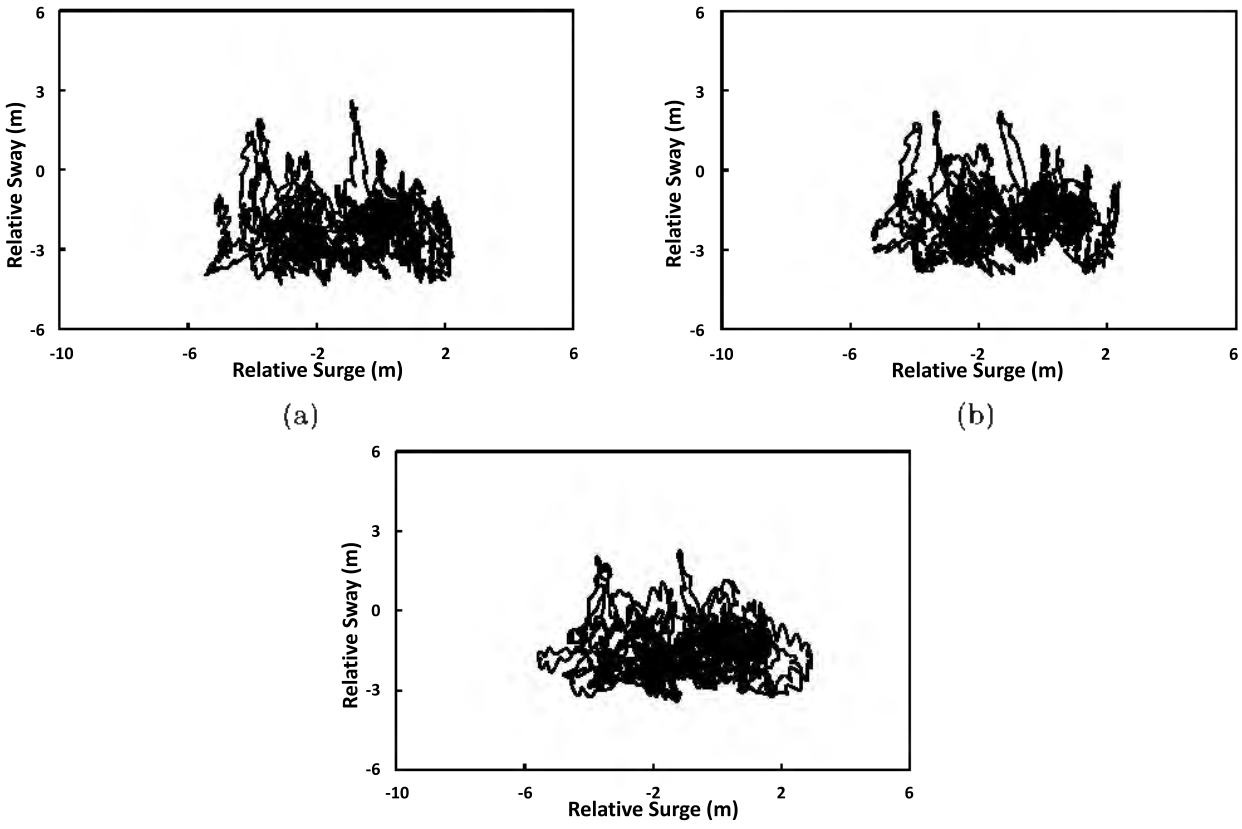

Figure 7.18 Trace plot of relative motions between FLNG and LNG in the horizontal plane at different hawser stiffness conditions (a) case 4, (b) case 5 and (c) case 6

Time history predictions on hawser and fender forces for varying hawser stiffness are presented in Figure 7.19. It is observed that the fluctuations in hawser tension can increase significantly as its stiffness is reduced. Conversely, increasing the hawser stiffness can result in more frequent collisions on the fenders. Statistical analysis has been carried out for the loads acting on hawser 5 and fender 4 as presented in Table 7.13. The maximum and mean tensions on the hawser increase as its stiffness is reduced. The same can be found for the maximum load on fender 4. Although not presented in this section, it is worth mentioning here that varying hawser stiffness has minor influences on the mooring line loads.

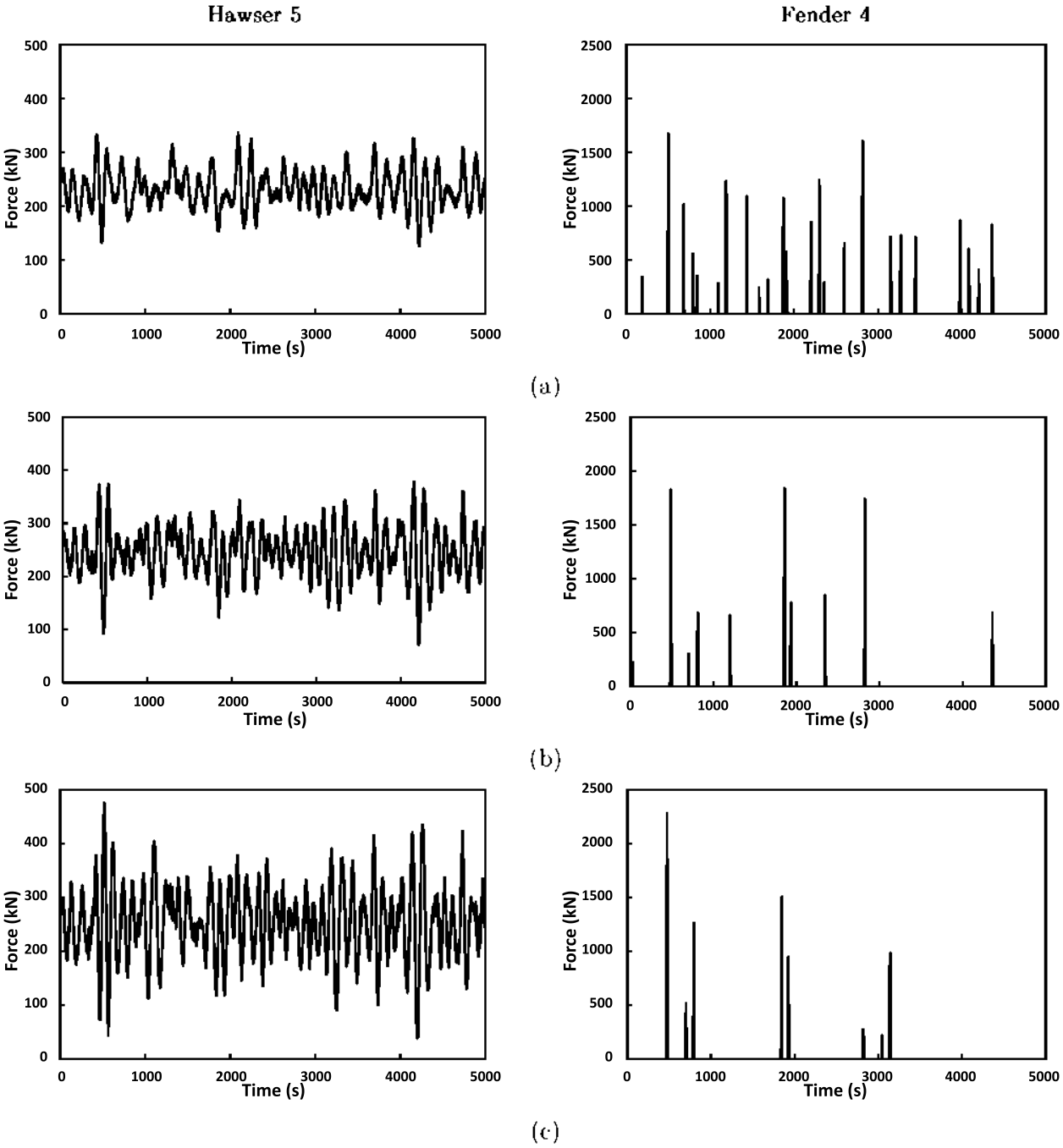

Figure 7.19 Time series of forces on hawser 5 and fender 4 at different hawser stiffness conditions (a) case 4, (b) case 5 and (c) case 6

Table 7.13 Quantitative comparison of hawser and fender loads at different hawser stiffness conditions

	Max	Min	Mean	STD
Hawser force (kN)				
Case 4	336.39	126.34	231.83	34.63
Case 5	378.80	71.42	245.81	46.45
Case 6	475.11	38.57	253.30	66.08
Fender force (kN)				
Case 4	1671.22	~	~	~
Case 5	1835.00	~	~	~
Case 6	2278.17	~	~	~

7.4 Concluding Remarks

A side-by-side FLNG-LNG offloading system coupled with inner turret mooring arrangement has been analysed numerically. Predictions of the hydrodynamic performance of the system under given environmental conditions are reported. First, the wave frequency forces and gap wave elevations are compared against experimental measurement for demonstrating the credibility of the performed simulation. The experimental and numerical results are found to correlate reasonably well despite some discrepancies in the high frequency region.

Based on the same numerical setup, the motion responses of the FLNG-LNG offloading system as well as hawser, fender and mooring forces have been investigated. A parametric study is also carried out for identifying the influences of varying hawser pretension and stiffness. From the obtained results, several interesting observations can be made:

- The surge, sway and yaw motions of the FLNG and LNG vessels exhibit long periodic nature while the heave, roll and pitch are dominated by wave frequency components.
- The LNG encounters much greater motion responses than the FLNG vessel due to its relatively smaller mass displacement.
- The mooring forces are dominated by the low frequency components and their periods are closely related to the orientation of the mooring line.
- The fender loads are found to be impulsive. Furthermore, it is observed that the fender in the bow of the vessels experiences more collisions than those in the stern for the studied base case.

- The hawser pretension and stiffness are found to be influential to the performance of the FLNG-LNG system including the trajectories of the vessels, the relative motions between the vessels and the hawser and fender loads.

- A decrease of hawser pretension and stiffness results in an increase in the relative horizontal plane motions between the two vessels as well as their fluctuations, but lead to a reduction in the number of collisions.

The presented study provides a basic understanding of the hydrodynamic characteristics of an FLNG-LNG offloading system in waves. This information will be useful in the design and development of such ship configuration. The numerical and experimental results are expected to be employed in the ship handling simulators to improve the reality of simulations.

Chapter 8 - Closure

8.1 Summary and Conclusions

This dissertation focuses on investigating the hydrodynamics around the side-by-side FLNG-LNG offloading system. Wave induced loads and motions on the structures and gap wave elevations have been studied through experimental and numerical approaches. The feasibility of viscous RANS/URANS methods on investigating the hydrodynamics of single FLNG/LNG and FLNG-LNG interactions has been assessed. The study also attempts to quantify the scale effects that exist in the predictions of wave loads and interaction forces and the issues associated with extrapolating model scale data to represent the full scale case. In this chapter, the major findings are presented and recommendations for future areas of research are identified and discussed.

The investigation begins with a preliminary study of the scale effects on the prediction of manoeuvring coefficients for a FLNG/LNG type of hull presented in the Appendix. The work demonstrates the capability of viscous RANS/URANS CFD solver on performing full scale simulations on ship hydrodynamics. Followed by that, numerical studies on estimating the FLNG-LNG interaction forces and moments in calm water steady current are carried out using a viscous steady state RANS approach. A detailed validation study of the numerical method with existing benchmark cases is presented. The numerical method is then applied for the systematic simulations to predict model scale and full scale hydrodynamic interactions. For modelling the FLNG-LNG interactions in waves, a two-phase flow volume of fluid method is adopted with the URANS computations for simulating the complex hydrodynamics involved. The application of such a numerical approach is proven to be accurate and reliable for estimating the single FLNG/LNG hydrodynamics in regular waves. The computed wave loads and motions on individual ship hull correlate well with experimental and potential flow predictions. Based on this, the URANS computations are extended to model the FLNG-LNG interactions in regular waves. Experimental studies are also performed for the validation of the numerical predictions for wave loads and gap wave responses. Once again, the scale effects on the interaction forces and moments have been investigated here. To investigate the global performance of the side-by-side FLNG-LNG system in a real world scenario, a case study based on time domain analysis is carried out with the system coupled with mooring lines, fenders and hawsers in an irregular sea environment. Predictions of the global performance

including the motion responses, fender and mooring loads of the system under realistic environmental conditions are reported.

8.2 Key Findings

8.2.1 FLNG-LNG interaction in calm water steady current

The key findings of the investigations into FLNG-LNG hydrodynamic interactions in calm water steady current are:

- The quasi-static viscous RANS method is successfully applied to predict the FLNG-LNG interactions in calm water steady current. The variation of interaction forces and moments for different positional offsets has been identified.
- The magnitude of non-dimensional model and full scale interaction force and moment predictions for the LNG and FLNG hulls correlate well.
- Model scale simulations demonstrate relatively thicker boundary layers and larger turbulent wake regions around the LNG and FLNG hulls, indicating a more significant viscous effect over the full scale conditions. As a result, large discrepancies exist between the predictions of model scale and full scale surge force magnitude, which illustrate that scale effects are evident.
- Scale effects are much less influential in sway force, roll moment and yaw moment predictions due to very good correspondence found between the patterns of model and full scale pressure distributions on the port side of the LNG and starboard side of FLNG hulls.

8.2.2 Single FLNG/LNG hydrodynamics in regular waves

Major observations from the investigation into single FLNG or LNG hydrodynamic performance in regular waves are:

- The URANS computations are feasible of making predictions of wave loads and motions on the FLNG/LNG individually in regular waves.
- For both head and oblique sea conditions, good correlations are observed between URANS, potential flow and experimental results.

- Scale effects are not evident in the predictions of wave loads and motions for single ship. The difference between model and full scale simulation results varies from 0.10% to 3.70% which are less than the estimated numerical uncertainties from the validation study.

8.2.3 FLNG-LNG interaction in regular waves

The following conclusions are drawn from the study of FLNG-LNG hydrodynamic interactions in regular waves:

- The URANS computations are feasible of making predictions of gap wave responses and wave loads for ship-ship interactions in waves.
- Viscous URANS computations provide more accurate predictions on the gap wave responses over PF method at relatively high wave frequency conditions when the lateral separation between two ships is relatively small (ΔS=100 mm and 200 mm). With greater lateral separation (ΔS=300 mm), the PF calculations are proven to have similar level of accuracy.
- PF method is still valid and recommended for predicting the wave loads when the incident wave frequency is relatively low and away from the natural frequency of the gap fluid considering its rapid computational time. The accuracy of PF method improves as the lateral separation increases.
- Gap wave resonance is observed when the incident wave frequency approaches the natural frequency of the fluid in the gap between the FLNG and LNG vessels. This also leads to significant variation of wave loads in the directions of surge, sway, heave, pitch and yaw.
- Changing the lateral separation can strongly affect the ship-ship hydrodynamic interactions. Reduction in the lateral separation between the FLNG and LNG brings greater exaggeration of gap wave responses and shifts the occurrence of gap wave resonance to a higher frequency region.
- The variation of lateral separation poses similar effects on the wave loads in the directions of sway, heave, pitch and yaw. When reducing the lateral separation between the FLNG and LNG, occurrence of peak wave load transfer functions of greater significance shifts to a higher frequency region.
- The model and full scale URANS computations correlate well in aspects of wave loads, gap wave responses and wave diffractions around the FLNG-LNG system, which implies the insignificant influence of scale effects for the tested wave cases.

8.2.4 Time domain analysis of an integrated FLNG-LNG system

The global performance of the integrated conceptual FLNG-LNG offloading system is summarised as followings:

- The surge, sway and yaw motions of the FLNG and LNG vessels exhibit long periodic nature while the heave, roll and pitch are dominated by wave frequency components. The LNG encountered much greater motion responses than the FLNG vessel due to its relatively smaller mass displacement.

- The mooring forces are dominated by the low frequency components and their periods are closely related to the orientation of the mooring line.

- The fender loads are found to be impulsive. Furthermore, it is observed that the fender at the bow of the vessels experiences more collisions than those near the stern for the studied base case.

- The hawser pretension and stiffness are found to be influential to the performance of the FLNG-LNG system including the trajectories of the vessels, the relative motions between the vessels and the hawser and fender loads.

- A decrease of hawser pretension and stiffness results in an increase in the relative horizontal plane motions between the two vessels as well as their fluctuations, but lead to a reduction in the number of collisions.

8.2 Suggestions for Future Work

Research into the FLNG-LNG hydrodynamic interactions using viscous RANS/URANS CFD approach can be implemented in several ways. The following recommendations for future work are proposed for developing a more sophisticated numerical model.

- Wave generation capabilities of URANS method are required to be investigated. The sensitivity studies for a wide range of sea-states, the effects of the irregularity, directionality and nonlinearity of ocean waves on the FLNG-LNG hydrodynamic interaction can be investigated.

- The influence of geometrical parameters such as body draft, breadth and bilge radius on the interaction forces and gap waves can be studied in the future.

- Real station-keeping mechanism including mooring lines, fender and hawsers can be incorporated in the viscous URANS computations for analysing the global performance of the FLNG-LNG system. Extensive studies should be carried out on the cost effectiveness and feasibility of such simulations.

- URANS predictions on the wave frequency loads can be adopted in the time domain PF analysis for more accurate modelling of gap wave resonance and its effect on the global motion performance of an integrated FLNG-LNG offloading system

References

ABKOWITZ, M. A., ASHE, G. M. & FORTSON, R. M. 1976. Interaction effects of ships operating proximity in deep and shallow water. 11th Symposium on Naval Hydrodynamics, 1976 University College of London, England.

ANSYS 2013. Aqwa Theory Manual. U.S.A.

BRIX, J. 1987. Manoeuvring technical manual. *Schiff und Hafen*, 36, 5 p.

BUCHNER, B., VAN DIJK, A. & DE WILDE, J. 2001. Numerical multiple-body simulations of side-by-side mooring to an FPSO. *International Society of Offshore and Polar Engineers (ISOPE)*.

CD-ADAPCO 2014. User guide STAR-CCM+ Version 9.0.6.

CHEN, G.-R. & FANG, M.-C. 2001. Hydrodynamic interactions between two ships advancing in waves. *Ocean Engineering*, 28, 1053-1078.

CHEN, X. B. 2005. Hydrodynamic analysis for offshore LNG terminals. *The Bulletin Technique of Bureau Veritas*.

DNV 2010. Environmental conditions and environmental loads. Det Norske Veritas.

DUFFY, J. T. 2008. *Modelling of ship-bank interaction and ship squat for ship-handling simulation*. 2008.

FANG, M.-C. & CHEN, G.-R. 2002. On Three-Dimensional Solutions of Drift Forces and Moments Between Two Ships in Waves. *Journal of Ship Research*, 46, 280-288.

FANG, M. C. & KIM, C. H. 1986. Hydrodynamically coupled motions of two ships advancing in oblique waves. *Journal of Ship Research*, 30.

FENTON, J. 1985. A Fifth - Order Stokes Theory for Steady Waves. *Journal of Waterway, Port, Coastal, and Ocean Engineering*, 111, 216-234.

HIMENO, Y. 1981. Prediction of Ship Roll Damping-A State of the Art. University of Michigan.

HOCHKIRCH, K. & MALLOL, B. On the importance of full-scale CFD simulations for ships. Proceedings of the 12th International Conference on Computer Applications and Information Technology in the Maritime Industries (COMPIT 2013). 2013 Cortona, Italy. pp.85-85.

HONG, S. Y., KIM, B. W., CHO, S. K., CHOI, Y. R. & KIM, Y. S. 2005. Numerical and experimental study on hydrodynamic interaction of side-by-side moored multiple vessels. *Ocean Engineering*, 32, 783-801.

IRVINE JR, M., LONGO, J. & STERN, F. 2008. Pitch and heave tests and uncertainty assessment for a surface combatant in regular head waves. *Journal of Ship Research*, 52, 146-153.

ITTC 2005. Testing and Extrapolation Methods, Loads and Responses, Seakeeping, Seakeeping Experiments. *ITTC Report, 7.5-02 07-02.1.*

ITTC 2011. Practical guidelines for ship CFD applications. 26th ITTC Specialist Committee on CFD in Marine Hydrodynamics.

JACOBSEN, N. G., FUHRMAN, D. R. & FREDSOE, J. 2012. A wave generation toolbox for the open - source CFD library: OpenFoam®. *International Journal for Numerical Methods in Fluids,* 70, 1073-1088.

JIN, Y., CHAI, S., DUFFY, J., CHIN, C., BOSE, N. & SUN, L. 2016. URANS prediction of ship hydrodynamics in head sea waves at zero forward speed with model testing validation. *International Conference on Ocean, Offshore and Arctic Engineering (OMAE2016).* Busan, South Korea: American Society of Mechanical Engineers.

JIN, Y., CHAI, S., DUFFY, J., CHIN, C., BOSE, N. & TEMPLETON, C. 2016a. RANS prediction of FLNG-LNG hydrodynamic interactions in steady current. *Applied Ocean Research,* 60, 141-154.

KASHIWAGI, M. Wave drift forces on two ships in close proximity. Ocean '04 - MTS/IEEE, 2004 Kobe, Japan. Marine Technology Society Inc., 578-584.

KIM, M. S., JEONG, H. S., KWAK, H. W., KIM, B. W. & EOM, J. K. Improvement method on offloading operability of side-by-side moored flng. 22nd International Offshore and Polar Engineering Conference, ISOPE-2012, June 17, 2012 - June 22, 2012, 2012 Rhodes, Greece. International Society of Offshore and Polar Engineers, 921-926.

KODAN, N. 1984. The motions of adjacent floating structures in oblique waves. *Journal of Energy Resource Technology,* 106, 199-205.

LATAIRE, E., VANTORRE, M. & DELEFORTRIE, G. Captive model testing for ship-to-ship operations. International Conference on Marine Simulation and Ship Maneuverability (MARSIM '09), 2009 Panama City, Panama. Panama Canal Authoritiy ; International Marine Simulator Forum.

LATAIRE, E., VANTORRE, M., DELEFORTRIE, G. & CANDRIES, M. 2012. Mathematical modelling of forces acting on ships during lightering operations. *Ocean Engineering,* 55, 101-115.

LONGO, J. & STERN, F. 2005. Uncertainty assessment for towing tank tests with example for surface combatant DTMB model 5415. *Journal of ship research,* 49, 55-68.

MENTER, F. R. 1994. Two-equation eddy-viscosity turbulence models for engineering applications. *AIAA journal,* 32, 1598-1605.

MOLIN, B., REMY, F., CAMHI, A. & LEDOUX, A. Experimental and numerical study of the gap resonances in-between two rectangular barges. 13th congress of international maritime association of mediterranean, 2009.

MORADI, N., ZHOU, T. & CHENG, L. 2015. Effect of inlet configuration on wave resonance in the narrow gap of two fixed bodies in close proximity. *Ocean Engineering,* 103, 88-102.

MOUSAVIRAAD, S. M., SADAT-HOSSEINI, S. H., CARRICA, P. M. & STERN, F. 2016b. Ship–Ship interactions in calm water and waves. Part 2: URANS validation in replenishment and overtaking conditions. *Ocean Engineering*, 111, 627-638.

MOUSAVIRAAD, S. M., SADAT-HOSSEINI, S. H. & STERN, F. 2016a. Ship–ship interactions in calm water and waves. Part 1: Analysis of the experimental data. *Ocean Engineering*, 111, 615-626.

NEWMAN, J. N. Progress in wave load computations on offshore structures. Invited Lecture, 23rd OMAE Conference, Vancouver, Canada, 2004.

NEWTON, R. N. 1960. Some notes on interaction effects betweem ships close aboard in deep water.

ORCAFLEX 2006. Orcina Ltd. *Daltongate, UK*.

ORIHARA, H. & MIYATA, H. 2003. Evaluation of added resistance in regular incident waves by computational fluid dynamics motion simulation using an overlapping grid system. *Journal of Marine Science and Technology*, 8, 47-60.

PINKSTER, J. A. 1979. Mean and low frequency wave drifting forces on floating structures. *Ocean Engineering*, 6, 593-615.

ROSEMAN, D. P. 1987. *The Marad systematic series of full-form ship models*, The Society of Naval Architects and Marine Engineers SNAME.

RUSCHE, H. 2003. *Computational fluid dynamics of dispersed two-phase flows at high phase fractions*. Imperial College London (University of London).

SADAT-HOSSEINI, H., WU, P.-C., CARRICA, P. M., KIM, H., TODA, Y. & STERN, F. 2013. CFD verification and validation of added resistance and motions of KVLCC2 with fixed and free surge in short and long head waves. *Ocean Engineering*, 59, 240-273.

SADAT-HOSSEINI, H., WU, P.-C., TODA, Y., CARRICA, P. & STERN, F. Urans studies of ship-ship interactions in shallow-water. 2nd International Conference on Ship Manoeuvering in Shallow and Confined Water: Ship to Ship Interactions 2011, May 18, 2011 - May 20, 2011, 2011a Trondheim, Norway. Royal Institution of Naval Architects, 299-308.

SADAT-HOSSEINI, H., WU, P., TODA, Y., CARRICA, P. & STERN, F. 2011b. Urans studies of ship-ship interactions in shallow-water.

SAITOH, T., MIAO, G. & ISHIDA, H. Theoretical analysis on appearance condition of fluid resonance in a narrow gap between two modules of very large floating structure. Proceedings of the 3rd Asia-Pacific Workshop on Marine Hydrodynamics, Beijing, China, 2006. 170-175.

SIMONSEN, C. D., OTZEN, J. F., JONCQUEZ, S. & STERN, F. 2013. EFD and CFD for KCS heaving and pitching in regular head waves. *Journal of Marine Science & Technology*, 18, 435.

SIMONSEN, C. D., OTZEN, J. F., NIELSEN, C. & STERN, F. 2015. CFD prediction of added resistance of the KCS in regular head and oblique waves. *30th Symposium on Naval Hydrodynamics*. Hobart, Australia.

STERN, F., WILSON, R. V., COLEMAN, H. W. & PATERSON, E. G. 2001. Comprehensive Approach to Verification and Validation of CFD Simulations—Part 1: Methodology and Procedures. *Journal of Fluids Engineering*, 123, 793-802.

TAYLOR, D. W. 1909. Some model experiments on suction of vessels. *Society of Naval Architects and Marine Engineers (SNAME)*.

TEZDOGAN, T., DEMIREL, Y. K., KELLETT, P., KHORASANCHI, M., INCECIK, A. & TURAN, O. 2015. Full scale unsteady RANS CFD simulations of ship behaviour and performance in head seas due to slow steaming. *Ocean Engineering*.

TUCK, E. O. & NEWMAN, J. N. 1974. Hydrodynamic interaction between ships. 10th Symposium on Naval Hydrodynamics, 1974 Cambridge, Massachusetts, USA.

VANTORRE, M., LAFORCE, E. & VERZHBITSKAYA, E. Model test based formulations of ship-ship interaction forces for simulation purposes. 2001 2001.

WEYMOUTH, G. D., WILSON, R. V. & STERN, F. 2005. RANS computational fluid dynamics predictions of pitch and heave ship motions in head seas. *Journal of Ship Research*, 49, 80-97.

WILCOX, D. C. 2008. Formulation of the k-w turbulence model revisited. *AIAA journal*, 46, 2823-2838.

WILSON, R. V., STERN, F., COLEMAN, H. W. & PATERSON, E. G. 2001. Comprehensive Approach to Verification and Validation of CFD Simulations—Part 2: Application for Rans Simulation of a Cargo/Container Ship. *Journal of Fluids Engineering*, 123, 803-810.

YASUKAWA, H. & YOSHIDA, S. Hydrodynamic interaction of two thin ships with rudder in close proximity. 2nd International Conference on Ship Manoeuvering in Shallow and Confined Water: Ship to Ship Interactions 2011, May 18, 2011 - May 20, 2011, 2011 Trondheim, Norway. Royal Institution of Naval Architects, 399-406.

ZHAO, W., WOLGAMOT, H., TAYLOR, P. & TAYLOR, R. E. 2017. Gap resonance and higher harmonics driven by focused transient wave groups. *Journal of Fluid Mechanics*, 812, 905-939.

ZHAO, W., YANG, J., HU, Z. & TAO, L. 2014. Prediction of hydrodynamic performance of an FLNG system in side-by-side offloading operation. *Journal of Fluids and Structures*, 46, 89-110.

ZHAO, W., YANG, J., HU, Z. & XIE, B. 2013. Hydrodynamics of an FLNG system in tandem offloading operation. *Ocean Engineering*, 57, 150-162.

ZHAO, W. H., YANG, J. M., HU, Z. Q. & WEI, Y. F. 2011. Review: Recent developments on the hydrodynamics of floating liquid natural gas (FLNG). *Ocean Engineering*, 38, 1555-1567.

ZOU, L. & LARSSON, L. 2013. Numerical predictions of ship-to-ship interaction in shallow water. *Ocean Engineering*, 72, 386–402.

ZOU, L., LARSSON, L., DELEFORTRIE, G. & LATAIRE, E. CFD prediction and validation of ship-bank interaction in a canal. 2nd International conference on ship manoeuvring in shallow and confined water, Trondheim, Norway, 2011.

Appendix - Publications

(Continued)